NEW EFFICIENT CONTACT DISCONTINUITY CAPTURING TECHNIQUES IN SUPERSONIC FLOW SIMULATIONS

By

Sergei V. Pevchin

A DISSERTATION SUBMITTED TO THE FACULTY OF

VIRGINIA POLYTECHNIC INSTITUTE AND STATE UNIVERSITY

IN PARTIAL FULFILLMENT OF THE REQUIREMENTS FOR THE DEGREE OF

DOCTOR OF PHILOSOPHY

IN

AEROSPACE ENGINEERING

Bernard Grossman, Chairman

John Steinhoff

Robert W. Walters

Joseph A. Schetz

Eugene M. Cliff

September 1996

Blacksburg, Virginia

Keywords: CFD, supersonic flow, discontinuities, confinement, capturing

Abstract

NEW EFFICIENT CONTACT DISCONTINUITY CAPTURING TECHNIQUES IN SUPERSONIC FLOW SIMULATIONS

by

Sergei V. Pevchin

Committee Chairman: Bernard Grossman
Aerospace Engineering

(ABSTRACT)

Accurate numerical algorithms for solving systems of nonlinear hyperbolic equations are considered. The issues of the capturing and the non-diffusive resolution of contact discontinuities were investigated using two different approaches: a kinetic fluctuation splitting scheme and a discontinuity confinement scheme based on an antidiffusion approach. In both approaches cell-vertex fluctuation-splitting methods are used in order to generate a multi-dimensional procedure.

The kinetic fluctuation-splitting scheme presented here is a Boltzmann type scheme based on an LDA-scheme discretization on a triangulated Cartesian mesh that uses diagonal adaptive strategy. The LDA scheme developed by Struijs, Deconinck and Roe has the property of being second-order accurate and linear for a scalar advection equation. It is implemented for the Boltzmann equation following the work of Eppard and Grossman and completes the series of multi-dimensional Euler solvers with upwinding applied at the kinetic level. The MKFS-LDA scheme is a cell-vertex scheme. It was

obtained by taking the moments of the fluctuation in the distribution function that are calculated according to the LDA fluctuation splitting procedure on a kinetic level. The diagonal-adaptive procedure designed by Eppard and Grossman for MKFS-NDA scheme was applied to eliminate the diagonal dependence. Results show improvement over lower-order N-scheme based solvers. Results for a simple oblique-shock reflection and a shear wave demonstrate that the adaptive procedure and the higher order low diffusion scheme provide sharper resolution than the dimensionally-split kinetic CIR scheme and the first order N-scheme. Moreover, no evidence of oscillations near discontinuities was observed but the order of accuracy is probably lower than the second-order theoretically predicted accuracy on regular meshes. Results for the inviscid reflection of an oblique shock wave and for an oblique shear wave indicate greatly improved resolution over first-order dimensionally-split approach. However, the complexity of the scheme and CPU usage increase were not justified by slight improvement over the first order N-scheme.

In the second part a new discontinuity confinement procedure is described. It uses ideas developed by Steinhoff to capture concentrated vorticity layers and short acoustic pulses. The discontinuity confinement method not only captures contact discontinuities over a few grid cells but also safeguards them from numerical dissipation as they evolve with time and over long spatial distances. A one dimensional discontinuity confinement method in terms of flux correction was developed and applied to the Euler solver. The results for the shock tube problem and contact discontinuity propagation were encouraging but the extension to two dimensional problems was not possible in the flux correction framework. A new scheme was developed using a closely related antidiffusion convection and fluctuation splitting ideas used in vortex confinement method by Steinhoff. The new formulation provides a simple and multi-dimensional procedure that can be used with any monotone basic solver.

A comparison of the dissipative property of the confinement scheme with a higher-order dimensionally split upwind scheme and several solutions on adaptive unstructured grids demonstrate that the new method has the ability to much more sharply resolve complex regions with contact discontinuities. Moreover, the quality of the

solution does not deteriorate over many time iterations or long spatial distances. Solutions for several two-dimensional steady problems are presented to demonstrate the high resolution property of the new scheme. It includes oblique shear layer problem, triple point problem and underexpanded nozzle flow. Underexpanded nozzle flow involves complex interaction of free surface, shock waves and slip lines. Traditional high-order schemes smear the contact surfaces preventing accurate definition of the flow structure inside the jet. However, using a Cartesian grid and the discontinuity confinement procedure the free surface of the jet and slip lines were resolved within 3 grid cells. In the case of an oblique shear layer the new scheme demonstrated no degradation of the initial profile for the discontinuity.

Robustness of the confinement scheme depends on the monotone basic solver and also multi-dimensional switch that excludes expansion regions from effect of the confinement. Research still needs to be done in order to develop a switch which can be used on a wide variety of applications.

Acknowledgements

The author is indebted to Dr. Bernard Grossman, whose guidance over the last four years has been invaluable. A huge thank you goes out to Dr. John Steinhoff, whose ideas have been a driving force during this research. I'm happy that I had a chance to learn from Dr. Walters that CFD could be fun but it is not an easy field to play. Also I'm grateful to Dr. Joseph Schetz and Dr. Pamela Kurstedt for their help in the beginning of my graduate study program at VPI & SU. I would like to mention Dr. Sidilkover for his valuable suggestions and corrections. A special thank you goes out to my family for the love and support they have provided over the years. And finally, to my friends at Virginia Tech whose help and friendship have made my work and life during last four years a great experience.

Contents

List of Figures

Chapter 1

Introduction

1.1 Overview

The present state of computational fluid dynamics (CFD) tools has been established by the rapid development of the methodology in the last three decades. During the last ten years dramatic changes in highly accurate and efficient numerical methods for the full range of Mach number regimes has been accompanied the explosive development in computer hardware. Together, numerical algorithms and computer equipment determine the capability of CFD to perform at the level necessary for real-life calculations. Three-dimensional calculations are possible for elementary aircraft configurations and are being performed on a daily basis.

At the same time, the variety of the methods and approaches is a sign of the growing stage when the preferences are not settled and universal approaches are still under scrutiny. There is a long way before the CFD community will get to some general methods that will be accepted by both academe and industry. The industry approval of CFD methods as design tools imposes requirements for the methods to be: a) simple to set up and use, b) inexpensive computationally and c) reliable for a wide range of the problems.

Two major players in today's CFD development are central difference and upwind difference solvers. The central difference approach, due to its relative simplicity, has made it easier to generate efficient solvers which utilize multigrid procedures

and implicit algorithms. At the same time the resolution of important features in supersonic and hypersonic flows, such as shock waves depends on user-controlled parameters that require extensive experience in numerical analysis. The use of an artificial dissipation has to be controlled by the user and there is no universal approach in this area. Problems arise in regions with steep gradients where central difference approximation breaks down. Another problem is that in smooth regions there is high-order dispersive error that causes slow convergence for steady state problems. Carefully added numerical dissipation is common way of dealing with these problems. But it requires a user who is expirienced in this field. Several methods introduced during the last decade will be described in Chapter 4.

Upwind methods are an alternative for central difference solvers and possess many attractive features. These include natural stability, very high precision at the shock waves, the minimum human input needed to control undesired oscillation, and an inherent mechanism for proper boundary conditions. Up to the late 1980s most upwind solvers were implemented using on one-dimensional techniques. The low quality of the multi-dimensional extensions demonstrated a serious need for a new theoretical base in order to develop genuinely two and three-dimensional solvers. In addition, the enhanced stability of implicit methods used with upwind differencing was tempered by expensive calculations needed for Jacobian matrices. The calculation of limiters throughout the flow field, even though they are only useful in limited regions with discontinuities, adds extra CPU load and reduces performance. Also, the logical switches that are the core of the limiters can slow convergence and impede the implementation of multigrid procedures to accelerate convergence.

1.2 Multidimensional Finite Volume Methods

Complex aerospace design problems that address turbulence, massively separated flows, and mixing flows demand development of genuine multi-dimensional algorithms to replace those based on one-dimensional physical modelling. Accurate representation of inviscid convective terms is one of the main requirements for a successful solver. Excessive artificial dissipation and cross-diffusion will not only affect the accuracy but

could overwhelm physical viscosity and cause non-physical solutions. Effective methods for the Euler equations not only improve high-Reynolds flow modelling but also build foundation for general problems described by Navier-Stokes equations.

At the present time, many reviewers point out that since multi-dimensional upwind methods are at a stage of early development, we still may see many changes before the massive introduction of the upwind solvers to industrial applications. Progress in the central difference schemes is somewhat less explosive and well established methods are used in practical applications. The introduction of the Runge-Kutta time-stepping procedure by Jameson *et al.* [1] in central difference solvers made them simple and efficient tools for numerical aerodynamic simulation. Currently, central-difference schemes with different forms of artificial dissipation are commonly used in the solution of the Navier–Stokes and Euler equations. Jameson *et al.* [1] introduced the most commonly used numerical dissipation. This is a blend of a second and fourth-order difference operators; the variation of the second order difference in the pressure actuates the second order dissipation. Stability, convergence to a steady state along with the elimination of the oscillatory mode are the main concerns of the design of different numerical dissipation models. In addition, complex three-dimensional computations require the most effective use of the available coarse meshes. That is, the amount of the added dissipation has to be minimized, especially in smooth regions, away from the major sources of instability (i.e., discontinuities). Jameson's method has proven to be efficient, but the resolution of the captured features is not monotone in general and contact discontinuities are poorly resolved. A matrix dissipation as a "smart" extension of the Jameson–type scalar dissipation was developed by Turkel, Swanson and Vatsa ([2], [3],[4]). Instead of a single constant it uses different scaling and limiters for different characteristic variables. The resulting series of improved central difference solvers demonstrated improved accuracy in both inviscid and viscous flows calculations. More elaborate applications of matrix dissipation schemes to combusting flows are presented by Gerlinger *et al.* [5].

The upwind methods for the modelling of the linear advection equations were originally introduced by Courant, Isaacson and Rees [6]. Their "CIR" scheme generated oscillation-free solutions in the presence of discontinuities where traditional

central difference schemes failed due to the invalidity of the Taylor series expansion in such regions. To apply these ideas to inviscid convection, the flux terms in the Euler solvers have to be split into positive and negative parts depending on the sign of the eigenvalues of the physical system. Characteristic decomposition is used to find the eigenvalues of the system of equations. This approach gave rise to popular upwind algorithms due to Van Leer [7] and Steger and Warming [8]. There are classified as flux-vector splitting methods.

A more physical alternative to the characteristic decomposition approach was introduced by Godunov [9], where the evolution of the flow was modelled in terms of a Riemann problem at each cell interface. This included the calculation of the shock tube subproblem for grid interfaces followed by the reconstruction stage when results of subproblems were projected to the piecewise constant distribution in the grid cells. However, most information generated by the Riemann solutions is lost and the scheme is only first order accurate. A more practical alternative was the approximate Riemann solver by Roe [10]. The family of Godunov-type schemes are referred as flux-difference splitting schemes.

The development of the upwind schemes was accompanied by the development of criteria to insure non-oscillatory behavior. The monotonicity conditions is the most severe, and it limits the accuracy of the scheme to first order. The total variation diminishing (TVD) condition developed by Harten [11] replaced monotonicity. It insured that monotone solutions will remain monotone at the next time step. Design of high resolution TVD schemes requires that one uses nonlinear methods. Accurate fluxes at the interfaces were calculated by higher-order extrapolation. The second order TVD scheme by Harten uses flux limiters to prevent a high order extrapolation from generating oscillations. Roe [12] and Chakravarthy and Osher [13] also used flux limiters to design high order upwind schemes based on approximate Riemann solvers. The extrapolation of the variables and calculation of the fluxes using extrapolated values is identical to the flux extrapolation procedure in the case of linear equations. For nonlinear fluxes, the two techniques have different properties. The system approach to the generation of the higher order upwind solver was introduced by Van Leer [14], [15] in his MUSCL procedure for higher-order schemes, which extrapolates

conserved variables and the calculated fluxes exactly. Instead of a piecewise constant distribution it uses a piecewise linear representation of the unknown in each grid cell. Reconstruction for each grid cell is based on information of the cell and its neighbours. Colella and Woodward [16] suggested PPM, whereas Harten *et al.* [17] established the family of ENO/UNO schemes. Different types of limiters and switches provided higher accuracy in smooth regions and stability in discontinuous regions.

All these upwind schemes lead to robust high quality solvers in one space dimension. Two and three dimensional calculations were based on dimensionally-split considerations and fluxes were split for each interface separately, using a one-dimensional characteristic decomposition or a one dimensional Riemann problem. Inherently based on one dimensional physics of the flow, this classic upwinding performs poorly and introduces unnecessary dissipation when convection or wave propagation are not normal to the grid interfaces. The TVD analysis in two dimensions also proved to be unreliable for unstructured grids [18] and limited schemes on Cartesian grid to first order accuracy, according to Goodman and LeVeque [19]. The notion of positivity as a replacement for the TVD condition for two dimensional structured grids was established by Spekreijse [20] and extended by Struijs *et al.* [21] to unstructured grids. It received new formulation as a local extremum diminishing (LED) condition introduced by Jameson [22] for unstructured grids and two and three dimensional solvers.

Multi-dimensional upwind schemes advanced in two distinct directions. In addition to the finite volume approach when the physics of the flow is simulated during interface flux calculations, the residual distribution schemes became a rapidly developed family of the upwind methods. The physics of the computational cell described by the unknowns on its vertices is considered. The variables are presented by piecewise linear distribution. Data representation is continuous which is a more physical situation. There are no privileged directions related to the geometry of the cell and gradients are modelled as a combination of linear waves. A cell-vertex method originated in the Lax-Wendroff scheme of Ni [23]. Morton and co-workers [24], [25] combined this approach with finite element methods and artificial dissipation methods to generate an effective technique in two and three dimensions [26]. The upwind application of

cell-vertex methods gave rise to the family of *fluctuation-splitting methods.* Here, the residual calculated for a grid cell is distributed to its vertices according to the upwinding strategy. There are many ways to calculate the residual and also a number of different distribution schemes. Roe pioneered this field [27] for one dimension where he used Roe-linearization to ensure the discrete conservation of the scheme. For two dimensions linearly distributed data were represented as a combination of planar waves and vorticity, see [28]. Later, he introduced a linear distribution scheme for the advection problem [29], using triangular meshes. Wave representation is used to calculate fluctuation, and the distribution stage completes the multi-dimensional upwind procedure. The scheme is compact since fluctuations are distributed only to the vertices of the triangles where they were calculated. Linear schemes satisfy either the positivity condition or a higher than first order approximation in the distribution of the variables. Nonlinear schemes that satisfy both criteria were introduced by Struijs *et al.* [21] and refined in collaborative research by CFD groups at the University of Michigan and the Von Karman Institute [30], [31], [32], [33], [34], [21]. A review of the different types of fluctuation splitting for the scalar conservation law in [35] covers both linear and nonlinear schemes. The recent results by Mesaros [36] demonstrate that despite excellent shock resolution properties, the application of the fluctuation-splitting methods in the subsonic and transonic range are not conclusive. Moreover, the extension to three dimensional problems is not clear because of additional complications in both the wave decomposition and the diagonalization procedures.

A more straightforward approach was proposed by Sidilkover [37]. It uses two and three dimensional extension of Roe linearization for the Euler equations [38] and fluctuation distribution is constructed on the Euler level, without resorting to characteristic wave decomposition or other types of wave modelling. Second order non-oscillating schemes with efficient multigrid capabilities [39] can be used for supersonic and subsonic calculations. Two-dimensional limiter proposed by Sidilkover provides an additional control over the positivity of the scheme. A simple three dimensional extension is also an appealing feature of the scheme.

Traditional finite volume methods pursued the goal of a high resolution multi-dimensional scheme in their own fashion. One of the popular approaches is the improvement of the flux modelling using multidimensional wave decomposition. Deconinck *et al.* [40] used characteristic decomposition to represent the flow in terms of two acoustic waves one shear wave and one entropy wave in the direction determined by pressure and velocity gradients . Wave representation is then used to calculate an upwind approximation at the interface and to construct the upwind procedure. Local decoupling of the Euler equation in two dimensions were also used by Hirsch *et al.* [41]. Two directions which allow the decoupling of the system of equations link the upwind procedure to the convection of the physical data. However, the new system is not conservative and requires a second conservative step; which results in a procedure that is upwind-central.

The original Roe solver was modified by Rumsey , Van Leer, and Roe [42] to obtain a grid-independent approximate Riemann solver in two dimensions. It uses five waves and leads to very sharply resolved oblique features. The same authors developed limiting procedure to suppress oscillations and overshoots near discontinuities [43]. First-order, two and three dimensional schemes were presented.

Another way to remove grid dependence is to consider the one dimensional problem in a direction relevant to the physical properties of the flow. Davis [44] suggested to use an upwind solver in the direction of the local pressure gradient. However, problems arise when the flow is near-uniform and the preferred direction becomes ill-defined. This leads to slow convergency and instability. A second order scheme based on this philosophy was developed by Levy *et al.* [45] and Dadone and Grossman [46]. Pressure or velocity magnitude were used as a sensitive parameter to determine tangent and normal fluxes. Levy used an interpolation process to calculate data at cell interfaces where fluxes are computed. Dadone and Grossman designed a procedure that chose the closest point as an approximation for data. Remarkable improvements were achieved compared to first order upwinding and classic dimensional-split second order schemes.

As central difference and upwind methodologies evolved with time, many reviewers noted that these two approaches are closely related. The latest developments

in artificial dissipation use an upwind approach to generate robust multidimensional schemes. Hirsch and Van Ransbeeck constructed the family of compact multidimensional schemes using a central difference approach, with artificial dissipation written as a classical first order upwind one dimensional dissipation plus multidimensional terms design to satisfy LED conditions. They applied the multi-dimensional limiter idea of Sidilkover [47] which results in second order accurate schemes for scalar convection. Euler applications are based on characteristic decomposition and the issue of the preferred direction is still unclear.

1.3 Multidimensional Kinetic Algorithms

Kinetic-based methods provide a natural generalization of the flux splitting procedure. The original study of the Boltzmann-type schemes was made by Harten *et al.* [48] where they approximated the hyperbolic system of conservation laws by a collisionless Boltzmann equation with different distribution functions, with limited support in the velocity space. The decomposition comes naturally from the decomposition of the distribution function that is a single scalar function. Original application were based on splitting at the Boltzmann level in a Courant-Isaacson-Rees (CIR) sense, resulting scheme is called Kinetic Flux-Vector Splitting (KFVS) [49]. Fluxes in scalar advection equation for the velocity distribution function are split according to velocity direction. The corresponding upwind discretization of the Euler equations is obtained as moments of the discretized Boltzmann scheme with a locally Maxwellian velocity distribution. Results for this scheme for multi-dimensional problems are similar to those by dimensionally-split traditional upwind schemes. Multi-dimensional kinetic schemes use multi-dimensional decompositions for the scalar hyperbolic equation and resulting moments of the fluctuation involve complex integration over the velocity space. This procedure eliminates the common problem with the multi-dimensional decomposition for the hyperbolic system when we do not have a straightforward procedure to define characteristic waves used in the flux splitting methods. This theoretical study was followed by the development of the first-order flux splitting by Deshpande [50] and Perthame [51], and the recent second order multidimensional

implementations by Perthame and Qiu [52]. They also used the distribution functions with a limited support and a simple shape function.

1.4 Discontinuity Confinement Technique

Traditional dimensional split upwind schemes or central difference schemes with artificial dissipation suffer from excessive cross diffusion and misinterpretation of the physics of the flow when the features are not aligned with the grid. In addition to these deficiencies, there is one type of problem that is rarely addressed in performance reviews of the methods. Short acoustic pulses and strong concentrated vorticity are examples of the flow features which have at least one small linear dimension and have to propagate over extensive distances. Numerical representation of these features will include high frequency components that are the first to be damped if the order of accuracy is not high enough. There are few computationally expensive options that resolve concentrated vorticity and prevent them from rapid dissipation. Fine grids require large memory storage. High order accuracy schemes increase the CPU load. Clustering and grid adaptation make multigrid methods and implicit time iteration hard to implement if possible at all.

The *vorticity confinement* method was developed by Steinhoff and coworkers for computing flows with concentrated vorticity and was originally applied to low-speed subsonic flows. Blade-vortex interaction problems were studied by Steinhoff *et al.* [53] using an Euler/Lagrangian method with additional velocity updating that preserves concentrated vorticity. Later they applied a velocity correction to the momentum conservation equations and solved incompressible Navier-Stokes equations for two and three dimensional vortex-dominated flows [54], [55]. The correction term is limited to the vorticity regions and does not affect smooth regions. Similar to shock capturing methods, it treats vortical layers without a detailed resolution of their internal structure. A confinement procedure is constructed in such a way that it preserves certain conservation laws outside and integrated over the vortical regions. The method is flexible and easily incorporated into standard Euler/Navier-Stokes methods on a

fixed grid [56]. Applied to various problems involving concentrated vorticity, the vorticity confinement approach has been proved to be capable of treating thin vortical structures in complicated flows even on relatively coarse grids. This new technique has been tested in conjunction with a compressible Euler/Navier Stokes solver for low speed compressible flows. It proved to be an effective tool for flows where vortical regions interact with the aerodynamic surfaces and where boundary layers undergo massive separation processes [57], [58]. Following the same antidiffusive convection idea as in vorticity confinement, Steinhoff *et al.* [59] have developed a new confinement procedure for short acoustic pulses. A "pressure confinement" convects the pressure wave back towards the center of a propagating pulse and balances numerical diffusion of a basic traditional solver.

1.5 Present Research

The objective of this research was to investigate new methods for the improvement in the resolution of discontinuities in multidimensional flow calculations, particularly for supersonic and hypersonic flow problems. Special effort was made to design a multi-dimensional solver capable of accurately resolving contact discontinuities.

There are two distinct parts in the presented work. The first approach was to use a Boltzmann-type scheme with the new multidimensional fluctuation splitting upwind scheme for the scalar advection equations. The Maxwellian velocity distribution function was used to calculate moments of the Boltzmann equation. Starting from the brief review of the previous efforts by Eppard and Grossman [60] to generate a first-order kinetic-based upwind scheme, we introduce a low diffusion scheme which has higher order accuracy. The method includes the LDA fluctuation splitting with adaptive cell decomposition [61]. Unfortunately, the improvement in the resolution was not strong enough to continue with this scheme. The development of the higher order nonlinear schemes that would provide better results is restricted by the impossibility of the analytical integration over the velocity space in the derivation of the scheme. The analysis and development of the scheme follows in Chapter 2. Some results are in Chapter 3.

The second stage of this work was the design of a discontinuity confinement technique for a supersonic and hypersonic flows. The origin of the method is in vortex and pulse confinement techniques developed by Steinhoff and coworkers [54],[59]; originally tested on vortex dominated flows the confinement technique was developed to treat more general discontinuities. A one dimensional discontinuity confinement method in terms of flux correction was developed and applied to the Euler solver. The results for the shock tube problem and contact discontinuity propagation were encouraging but the extension to two dimensional problems was not possible in the flux correction framework. A new scheme was developed using a closely related antidiffusion convection and fluctuation splitting ideas used in vortex confinement method. An additional stage for the conservation procedure was introduced into the solver. Preliminary two dimensional results for the steady state calculations demonstrate the potential of the method to be useful as a supplement to multi-dimensional solvers. There still are several issues that must be addressed in order to fully explore these ideas. The technique is developed in Chapter 4 and results are given in Section 5. An evaluation of the two approaches is given in Chapter 6.

Chapter 2

Kinetic Fluctuation Splitting Scheme

2.1 Essentials of Kinetic Theory

Kinetic theory is intended to describe the motion of the individual particles in a system using a statistical approach. In contrast to the macroscopic model that regards the gas as a continuous medium, kinetic theory uses a molecular model that describes the gas through the information about molecules that form it. It uses position, velocity and state of each molecule to describe the system. The core element of the statistical model is a distribution function that determines the probability of the particle to be present in a particular element of the phase space described by its location $(x_1, x_2, x_3, c_1, c_2, c_3, t)$ and the volume $(dx_1, dx_2, dx_3, dc_1, dc_2, dc_3)$, where x_i represent the spatial coordinates and c_i represent the particle velocity components.

The dynamics of the system of the N particles is determined by the evolution of the distribution function $F^N(x_i^l, c_i^l, t)$ for all N particles:

$$\frac{\partial}{\partial t}(F^N) + \sum_{l=1}^{N} \boldsymbol{c}^l \cdot \frac{\partial F^N}{\partial \boldsymbol{x}^l} + \frac{1}{m} \sum_{l=1}^{N} \frac{\partial}{\partial \boldsymbol{c}^l} \cdot \left(\boldsymbol{Y}_i F^N \right) = 0, \tag{2.1}$$

which is a well known Liouville equation. It uses $6N + 1$ dimensional phase space to described the system. The vector $\boldsymbol{Y}_i$ represents external force and m is the mass of the particle.

This general presentation of the system is complex and impractical to implement. We do not need such a detailed description of the flow. Kinetic theory uses a more limited model that leads to the Boltzmann equation for the *velocity distribution function* $f(\boldsymbol{c}, \boldsymbol{x}, t)$. For a simple dilute gas it gives

$$\frac{\partial}{\partial t}(nf) + \boldsymbol{c}\frac{\partial}{\partial \boldsymbol{x}}(nf) + \boldsymbol{X} \cdot \frac{\partial}{\partial \boldsymbol{c}}(nf) = \int_{-\infty}^{\infty} \int_{0}^{4\pi} n^2 (f^* f_1^* - f f_1) c_r \sigma d\Omega d\boldsymbol{c}_1, \qquad (2.2)$$

where n is the number density and $\boldsymbol{X}$ is the external force per unit mass acting on a particles. The Boltzmann equation describes the change in the number of molecules within the phase space element $d\boldsymbol{c}d\boldsymbol{x}$. The collision term on the right-hand side represents the total rate of increase of the number of molecules of class $\boldsymbol{c}$ in the element due to collisions with the rest of the molecules. It has to be integrated for all possible directions and magnitudes of the velocities ($\boldsymbol{c}_1$) of the second particle that participates in binary collisions. Distribution functions after collision, traditionally denoted as f^* and f_1^* are determined based on chosen modell for collision. This is the main source of mathematical difficulties associated with the Boltzmann equation and its modelling is the subject for numerous investigations.

The simplification of the Liouville equation (2.1) to the Boltzmann equation (2.2) comes at the expense of certain limitations on the usage of the model. The intermolecular forces are disregarded during intercollisional travel of the particles which means that the resulting equation is valid only for thermally perfect gases or may be extended to their mixture. The collisions are modelled by the use of the *collision cross-section* $\boldsymbol{\sigma}$ that eliminates the integration over all possible interactions among all of molecules. The intermolecular forces will not explicitly be used in the following discussion. The definition of the dilute gas limited the space that actually contains a molecule to the small portion of the overall gas volume. This way, the probability of two molecules to be in a particular state will be fully described by the product of the probability of each single molecule to be in its particular state alone. There will be no correlation between distribution functions of two colliding molecules according to the principle of *molecular chaos* [62]. Also, the assumption of the large intermolecular spacing let us assume that only binary collision have to be considered. An additional assumption is that the distribution function is uniform over the distances of the order

of the collisional cross section and does not change noticeably over the collision time. The mathematical transformation used to develop the Boltzmann equation also requires that the distribution function be differentiable along the phase trajectory [63]. Detailed discussion of the Boltzmann theory and its limitations can be found, for example, in Bird [63], Kogan [62], Grad [64] and Harris [65].

The macroscopic properties are defined as average values of the appropriate microscopic quantities over the molecular velocities. We use the single particle distribution function to describe the molecules in an element of the physical space over which the average is taken. The microscopic quantity itself can be either constant or the function of the molecular velocity. The statistical average for the molecular quantity $Q(\boldsymbol{c})$ at a given time and spatial location is given as the following moment of the velocity distribution function

$$\overline{Q}(\boldsymbol{x},t) = \int_{-\infty}^{\infty}\int_{-\infty}^{\infty}\int_{-\infty}^{\infty} Q(\boldsymbol{c}) f(\boldsymbol{c},\boldsymbol{x},t) dc_1 dc_2 dc_3. \tag{2.3}$$

These averages are referred to as moments of the distribution function. The macroscopic density is the simplest one due to the constant molecular mass (m in our notations). It is defined as the mass per unit volume of gas and calculated directly as the product

$$\rho = nm, \tag{2.4}$$

where n is a numerical concentration of the molecules in a gas. The stream velocity in the i-direction will be defined as the mean molecular velocity, i.e.

$$u_i = \overline{c_i}. \tag{2.5}$$

Thermal or random velocity as the velocity of the molecule relative to the stream velocity will be denoted by c' and given as

$$c'_i = c_i - u_i. \tag{2.6}$$

The mean thermal velocity is zero in a simple gas, i.e.

$$\overline{c'_i} = \overline{c_i} - u_i = 0. \tag{2.7}$$

The momentum transport by the peculiar or thermal motion is described by the pressure tensor

$$\boldsymbol{p} = \rho\overline{\boldsymbol{c}'\boldsymbol{c}'} \tag{2.8}$$

and for thermally perfect gases we define the scalar characteristic — "kinetic" pressure as the average of the three normal components of the pressure tensor:

$$p = \frac{1}{3}\rho\left(\overline{c_1^2} + \overline{c_2^2} + \overline{c_3^2}\right) = \frac{1}{3}\rho\overline{c'^2}. \tag{2.9}$$

The specific kinetic energy due to thermal transportation is given as a statistical average of the kinetic energy for a molecule per unit mass, i.e.

$$e_{tr} = \frac{\overline{\frac{1}{2}mc'_i c'_i}}{m} = \frac{1}{2}\overline{c'^2}. \tag{2.10}$$

The relation between the molecular and macroscopic quantities described above can be used to transform the Boltzmann equation. The conservation equations for the continuum gas dynamics are obtained by taking the moments of the Boltzmann equation multiplied by the set of particular functions $\psi = \psi(\boldsymbol{c})$. We will use the *moment function vector* $\boldsymbol{\Psi}$ which represents the molecular mass, momentum and the total energy

$$\boldsymbol{\Psi} = \begin{pmatrix} m \\ mc_k \\ m\epsilon_0 \end{pmatrix}, \tag{2.11}$$

with

$$\epsilon_0 = \frac{c_k c_k}{2} + \epsilon', \tag{2.12}$$

and ϵ' represents the internal energy per unit mass. The modelling of the internal energy depends on the problem under consideration. A general model introduced by Liu and Vinokur [66] is given as

$$\epsilon = \tilde{\epsilon}(T) + \epsilon_n(T_n) + \epsilon_e(T_e), \tag{2.13}$$

and it covers many problems with thermodynamic non-equilibrium. The kinetic energy $(c_k c_k)/2$ of thermal translation and the contribution of the internal modes that are assumed to be in equilibrium at the translational temperature, T, are included

in the first term $\tilde{\epsilon}(T)$. The non-equilibrium term $\epsilon_n(T_n)$ includes the internal modes that are assumed to satisfy a Boltzmann distribution at the non-equilibrium temperature T_n. The electronic contribution with the electron temperature T_e is supposed to describe the contribution of the bound electrons within a particle and free electrons in the system.

The suggested integration over all velocity space yields

$$\int_{-\infty}^{\infty} \boldsymbol{\Psi}(\boldsymbol{c})\Big[\frac{\partial}{\partial t}(nf) + \boldsymbol{c}\frac{\partial}{\partial \boldsymbol{x}}(nf) + \boldsymbol{X}\cdot\frac{\partial}{\partial \boldsymbol{c}}(nf) \\ -\int_{-\infty}^{\infty}\int_{0}^{4\pi} n^2(f^*f_1^* - ff_1)c_r\sigma d\Omega d\boldsymbol{c}_1\Big]d\boldsymbol{c} = 0. \tag{2.14}$$

We can use now the independence of the variables $\boldsymbol{c}$, $\boldsymbol{x}$ and t to switch the order of integration and differentiation in the first and second terms. Since each component of the moment function vector is either a constant or a function of $\boldsymbol{c}$ only, we can simplify the equation by taking $\boldsymbol{\Psi}$ inside the derivative in the first and second term, $\boldsymbol{c}$ inside the derivative in the second term and, at last, integrate the third term by parts:

$$\begin{aligned}
\int_{-\infty}^{\infty} \boldsymbol{\Psi}(\boldsymbol{c})\frac{\partial}{\partial t}(nf)d\boldsymbol{c} &= \frac{\partial}{\partial t}\left(n\int_{-\infty}^{\infty}\boldsymbol{\Psi}f d\boldsymbol{c}\right) = \frac{\partial}{\partial t}\left(n\overline{\boldsymbol{\Psi}}\right) \\
\int_{-\infty}^{\infty} \boldsymbol{\Psi}(\boldsymbol{c})\frac{\partial}{\partial \boldsymbol{x}}(nf)d\boldsymbol{c} &= \int_{-\infty}^{\infty}\nabla\cdot(n\boldsymbol{c}\boldsymbol{\Psi}f)\,d\boldsymbol{c} = \nabla\cdot(n\overline{\boldsymbol{c}\boldsymbol{\Psi}}) \\
\int_{-\infty}^{\infty} \boldsymbol{\Psi}(\boldsymbol{c})\boldsymbol{X}\cdot\frac{\partial}{\partial \boldsymbol{c}}(nf)d\boldsymbol{c} &= \int_{-\infty}^{\infty}\boldsymbol{X}\cdot\frac{\partial}{\partial \boldsymbol{c}}(n\boldsymbol{\Psi}f)d\boldsymbol{c} - \int_{-\infty}^{\infty}\boldsymbol{X}\frac{\partial\boldsymbol{\Psi}}{\partial \boldsymbol{c}}nf d\boldsymbol{c} = -n\boldsymbol{X}\cdot\overline{\frac{\partial\boldsymbol{\Psi}}{\partial \boldsymbol{c}}}.
\end{aligned}$$

In the transformation for the external force term it assumed that $\boldsymbol{X}$ is independent of $\boldsymbol{c}$ and the distribution function f has limited support or $f \to 0$ as $c \to \infty$ and the first integral vanishes. The resulting equation of transfer is given as

$$\frac{\partial}{\partial t}(n\overline{\boldsymbol{\Psi}}) + \nabla\cdot\left(n\overline{\boldsymbol{c}\boldsymbol{\Psi}}\right) - n\boldsymbol{X}\cdot\overline{\frac{\partial\boldsymbol{\Psi}}{\partial \boldsymbol{c}}} = \int_{-\infty}^{\infty}\int_{-\infty}^{\infty}\int_{0}^{4\pi} n^2\boldsymbol{\Psi}(f^*f_1^* - ff_1)c_r\sigma d\Omega d\boldsymbol{c}_1 d\boldsymbol{c}. \tag{2.15}$$

The integral of the term on the right-hand side is called the *collisional integral* J.

The analysis of the collisional invariant and Boltzmann's H-theorem supply us with important requirement for the distribution function. In particular, for the case of local translational equilibrium, it is necessary that the distribution function be the local Maxwellian velocity distribution function. By "equilibrium state" we mean the

situation when the distribution of the molecule in the velocity space remains constant with time. We denote this function f_0 and we call it local since in general it depends on t and $\boldsymbol{x}$, given by

$$f_0(\boldsymbol{c},\boldsymbol{x},t) = \left(\frac{1}{2\pi RT}\right)^{3/2} exp\left\{-2RT[(c_1-u_1)^2+(c_2-u_2)^2+(c_3-u_3)^2]\right\}, \quad (2.16)$$

where R is a universal gas constant. The collision integral J is zero since for the Maxwellian distribution function $f^* f_1^* = f f_1$.

For gases in a local translational equilibrium state and subject to zero body forces the Boltzmann equation reduces to the homogeneous scalar advection equation

$$\frac{\partial}{\partial t}(nf_0) + \boldsymbol{c}\frac{\partial}{\partial \boldsymbol{x}}(nf_0) = 0. \quad (2.17)$$

With this simple form of the governing equation on the kinetic level we can complete our discussion for the macroscopic system. In the following integrations we will use a local Maxwellian distribution function for the statistically averaged variables and for the moments of the Boltzmann equation. The kinetic pressure, Equation(2.9), and the average kinetic energy, Equation(2.10), become

$$p = \frac{1}{3}\rho\overline{c_i' c_i'}|_{f_0} = \frac{1}{3}\rho\int_{-\infty}^{\infty}\int_{-\infty}^{\infty}\int_{-\infty}^{\infty} c_i' c_i' f_0 dc_1 dc_2 dc_3 = \frac{1}{3}\rho 3RT, \quad (2.18)$$

and

$$e_{tr} = \frac{1}{2}\overline{c_i' c_i'}|_{f_0} = \frac{3}{2}RT, \quad (2.19)$$

respectively. Hence, we reproduced the result from classical equilibrium thermodynamics for the thermally perfect gas

$$p = \rho RT. \quad (2.20)$$

The *transfer equation* (2.15) in case of the Maxwellian distribution function will reduce to the following

$$\frac{\partial}{\partial t}(n\overline{\Psi}) + \nabla\cdot\left(n\overline{\boldsymbol{c}\Psi}\right) - n\boldsymbol{X}\cdot\overline{\frac{\partial\Psi}{\partial\boldsymbol{c}}} = 0, \quad (2.21)$$

and the conservative equations of gas dynamics with zero body forces will take the form

$$\frac{\partial \boldsymbol{Q}}{\partial t} + \frac{\partial \boldsymbol{F}}{\partial x_1} + \frac{\partial \boldsymbol{G}}{\partial x_2} + \frac{\partial \boldsymbol{H}}{\partial x_3} = 0, \quad (2.22)$$

where the conserved-variable vector is defined as

$$\boldsymbol{Q} \equiv \int_{-\infty}^{\infty}\int_{-\infty}^{\infty}\int_{-\infty}^{\infty} \boldsymbol{\Psi} n f_0 dc_1 dc_2 dc_3 = \overline{n\boldsymbol{\Psi}}, \tag{2.23}$$

and the flux vectors are defined as

$$\begin{aligned} \boldsymbol{F} &\equiv \int_{-\infty}^{\infty}\int_{-\infty}^{\infty}\int_{-\infty}^{\infty} \boldsymbol{\Psi} c_1 n f_0 dc_1 dc_2 dc_3 = \overline{n\boldsymbol{\Psi} c_1} \\ \boldsymbol{G} &\equiv \overline{n\boldsymbol{\Psi} c_2} \qquad \boldsymbol{H} \equiv \overline{n\boldsymbol{\Psi} c_3}. \end{aligned} \tag{2.24}$$

The equation (2.22) is the Euler equation and the vectors (2.23),(2.25) after proper integration are given as

$$\boldsymbol{Q} = \begin{pmatrix} \rho \\ \rho u \\ \rho v \\ \rho w \\ \rho e_0 \end{pmatrix}, \tag{2.25}$$

and

$$\boldsymbol{F} = \begin{pmatrix} \rho u \\ \rho u^2 + p \\ \rho uv \\ \rho uw \\ \rho u h_0 \end{pmatrix} \qquad \boldsymbol{G} = \begin{pmatrix} \rho v \\ \rho vu \\ \rho v^2 + p \\ \rho vw \\ \rho v h_0 \end{pmatrix} \qquad \boldsymbol{H} = \begin{pmatrix} \rho w \\ \rho wu \\ \rho wv \\ \rho w^2 + p \\ \rho w h_0 \end{pmatrix}, \tag{2.26}$$

where u, v, w are the velocity components, e_0 is a total energy and h_0 is a total enthalpy. These are inviscid fluxes for the Euler equation, in addition we need the closure relations to complete the description of the system. For a perfect gas assumption the vibrational contribution to the internal energy vanish and the translational and rotational modes are in equilibrium at the translational temperature. Combining these assumptions and the results for the Maxwellian distribution function, Equations (2.18),(2.19), one has

$$\begin{aligned} p &= \rho RT \\ e_0 &= \rho e + \frac{1}{2} u_k u_k \end{aligned} \tag{2.27}$$

$$
\begin{aligned}
e &= \frac{3}{2}RT + c_{vrot}T \\
h_0 &= e_0 + \frac{p}{\rho}.
\end{aligned}
$$

$$
c_{vrot} = \begin{cases} R & \text{for diatomic and linear polyatomic molecules} \\ \frac{3}{2}R & \text{for non-linear polyatomic molecules.} \end{cases} \tag{2.28}
$$

where linearity implies alignment of atoms in molecule.

Demonstrated connection between the Boltzmann equation on the kinetic level and the Euler equations on the macroscopic level will be used to construct multi-dimensional upwind scheme as moments of discretized Boltzmann scheme with a local Maxwellian distribution function. In our further discussion, however, we will use a more appropriate integral form of the Boltzmann equation that includes integration over the spacial coordinates in addition to the velocity space moments. For the moment function vector $\boldsymbol{\Psi}(\boldsymbol{c}, \boldsymbol{x}, t)$ the intgration will be written as the following:

$$
\begin{aligned}
&\frac{\partial}{\partial t}\int_{\delta V}\int_{-\infty}^{\infty} \boldsymbol{\Psi} n f d\boldsymbol{c} dV + \oint_{\delta S}\int_{-\infty}^{\infty} \boldsymbol{\Psi}(\bar{\boldsymbol{c}}\cdot\hat{\boldsymbol{n}}_o) n f d\boldsymbol{c} dS + \\
&\int_{\delta V}\int_{-\infty}^{\infty} \boldsymbol{\Psi}\frac{\partial}{\partial \boldsymbol{c}}\left\{(\boldsymbol{X})\, nf\right\} d\boldsymbol{c} dV = \int_{\delta V}\int_{-\infty}^{\infty}\int_{0}^{4\pi} n^2(f^* f_1^* - f f_1)\boldsymbol{\Psi} c_r \sigma d\Omega d\boldsymbol{c}_1\Big] d\boldsymbol{c},
\end{aligned} \tag{2.29}
$$

where δV is an arbitrary volume bound by the surface δS and $\hat{\boldsymbol{n}}_o$ is an outward pointing normal vector. If we follow the same transformation procedure as for Equation (2.15) in addition assuming zero external forces and equilibrium flow, the final form of the integral governing equation for the control volume becomes

$$
\frac{\partial}{\partial t}\int_{\delta V} n\overline{\boldsymbol{\Psi}} dV + \oint_{\delta S} n\overline{\boldsymbol{\Psi}\boldsymbol{c}}\cdot\hat{\boldsymbol{n}}_o dS = 0, \tag{2.30}
$$

or using conservative variables vector from Equation(2.25) and conservative generalized flux-vector $\boldsymbol{S}$ it could be rewritten as

$$
\frac{\partial}{\partial t}\int_{\delta V} \boldsymbol{Q} dV + \oint_{\delta S} n\boldsymbol{S}\cdot\hat{\boldsymbol{n}}_o dS = 0, \tag{2.31}
$$

where $\boldsymbol{S}$ is defined as

$$
\boldsymbol{S} = \boldsymbol{F}\boldsymbol{i}_1 + \boldsymbol{G}\boldsymbol{i}_2 + \boldsymbol{H}\boldsymbol{i}_3. \tag{2.32}
$$

In our study we also use the other order of integration of Equation (2.30). We first perform time integration and integration over the control volume; only after we

compute these values we use the velocity space moments to calculate an update for the Euler system of equations:

$$\int_{-\infty}^{\infty} \Psi \left[\int_{\delta V} \frac{\partial}{\partial t}(nf)dV + \oint_{\delta S}(nf)\mathbf{c}\cdot\hat{\mathbf{n}}_o dS \right] d\mathbf{c} = 0. \tag{2.33}$$

2.2 Kinetic Flux-Vector Splitting Scheme

2.2.1 Upwind Flux Splitting

In the previous discussion we showed that the Euler system of equations is closely related to the reduced form of Boltzmann equation (2.17). At the same time, in last couple decades, an extensive set of numerical approaches to solve scalar hyperbolic equations have been developed. The definite leaders in this field are the upwind methods. This approach introduces the physical propagation of perturbations along characteristics in the design of the numerical models for hyperbolic equations. If we step back and recall the widely used central difference then the main problem with them is that when we require high order accuracy than we run into problems with oscillations in the vicinity of the discontinuities. Later in this work (Chapter 4) we will introduce one of the most common ways of dealing with this problem — an artificial dissipation; in particular Jameson type dissipation that is well known and used in many present calculations. The discretizations based solely on Taylor expansion can be used up to any order of accuracy as long as there is no discontinuity in the domain, when we have only the smooth function. A construction of reliable and systematic schemes that will need as little as possible adjustment for a particular problem requires introduction of the essential physical information in the solvers. The upwind methods use characteristic to guide the propagation of the information through the domain.

Godunov-type methods use an exact local solution of the Euler equation at each cell interface. They solve the Riemann problem exactly or approximately and the order of the scheme will be determined at the reconstruction step when right and left states for the next iteration of the Riemann solver are calculated. The physics of the problem is implemented on the local level in the Riemann sub-solver.

The flux vector splitting methods use a different approach. The discretization of the governing equations depends on the local characteristics, particularly on their direction. For the system of coupled nonlinear equations, the characteristic decomposition is not straightforward and nonunique for the multi-dimensional problems. Moreover, in a situation when the eigenvalues of the system have different signs the flux decomposition becomes even more complicated and inconsistent even for the homogeneous equations. The eigenvalues of the original flux vector and of the negative and positive portions after splitting are different in general.

The upwind methods proved to be efficient as the shock capturing tools and their development for the Euler equation is continued with variable success. The particular problem is the design of the genuine multi-dimensional solvers.

2.2.2 Boltzmann Type Schemes

The original ideas of the upwind methods for the hyperbolic equation was developed by Courant, Issacson and Reeves [6] and for the one dimensional linear advection equation $u_t + cu_x = 0$ it could be written as

$$u_i^{n+1} - u_i^n = -\frac{\Delta t}{\Delta x}[c^+(u_i^n - u_{i-1}^n) + c^-(u_{i+1}^n - u_i^n)] \tag{2.34}$$

where the positive and negative projection of the eigenvalues

$$\begin{aligned} c^+ &= max(c, 0) = \frac{c + |c|}{2} \\ c^- &= min(c, 0) = \frac{c - |c|}{2} \end{aligned} \tag{2.35}$$

If we apply this directly to the Boltzmann equation that is reduced to the scalar advection equation for the Maxwellian velocity distribution function, the upwind discretization in space gives

$$\frac{\partial}{\partial t}(nf_0)_i + \frac{c_1 + |c_1|}{2} \cdot \frac{(nf_0)_i - (nf_0)_{i-1}}{\partial x_1} + \frac{c_1 - |c_1|}{2} \cdot \frac{(nf_0)_{i+1} - (nf_0)_i}{\partial x_1} = 0. \tag{2.36}$$

The corresponding upwind discretization of the Euler equation is obtained by multiplying this equation with the moment function vector Ψ and integrating the resulting

expression similarly to Equation (2.15). The integration will be split into two parts, one is over the positive half of the c_1 velocity space and the other one is over the negative counterpart. We denote the corresponding flux vectors as $\boldsymbol{F}^+$ and $\boldsymbol{F}^-$. The vector expression for the resulting scheme

$$\left(\frac{\partial \boldsymbol{Q}}{\partial t}\right)_i + \frac{\boldsymbol{F}^+{}_i - \boldsymbol{F}^+{}_{i-1}}{\Delta x_1} + \frac{\boldsymbol{F}^-{}_{i+1} - \boldsymbol{F}^-{}_i}{\Delta x_1} = 0; \tag{2.37}$$

this is the first order accurate in space one-dimensional upwind scheme that we will call the KFVS-CIR scheme. The one-dimensional vector of conservative variables is written as following

$$\boldsymbol{Q} = \begin{pmatrix} \rho \\ \rho u_1 \\ \rho e_0 \end{pmatrix} \tag{2.38}$$

and the flux vector is calculated

$$\boldsymbol{F}^{\pm} = \rho < \frac{c_1 \pm |c_1|}{2} \begin{pmatrix} 1 \\ c_1 \\ \epsilon_0 \end{pmatrix} > \Big|_{f_0} = \tag{2.39}$$

$$\begin{pmatrix} \frac{1}{2}\rho u_1 \left[1 \pm erf(\sqrt{\beta} u_1)\right] \pm \frac{\rho}{2\sqrt{\beta\pi}} e^{-\beta {u_1}^2} \\ \frac{1}{2}(\rho u_1^2 + p) \left[1 \pm erf(\sqrt{\beta} u_1)\right] \pm \frac{\rho u_1}{2\sqrt{\beta\pi}} e^{-\beta {u_1}^2} \\ \frac{1}{2}(\rho u_1 h_0) \left[1 \pm erf(\sqrt{\beta} u_1)\right] \pm \rho h_0 - \frac{1}{2} p \frac{1}{2\sqrt{\beta\pi}} e^{-\beta {u_1}^2} \end{pmatrix}$$

using the error function

$$erf(x) = \frac{2}{\sqrt{\pi}} \int_0^x e^{t^2} dt. \tag{2.40}$$

Some details of this integration procedure and integration in the rest of this chapter are shown in Appendix A.

If we would replace the Maxwellian distribution function by the delta function then the result of this integration is the Steger and Warming [67] flux splitting for the equation of gas dynamics. Detailed study of the entropy conditions and the stability analysis are performed by Harten *et.al.* in [48].

2.3 Multi–Dimensional Kinetic Fluctuation Splitting Schemes

The design of an upwind high resolution multi-dimensional solver can not rely on combination of the one-dimensional solvers. The finite volume approach, so typical for the computation of convection dominated flows with strong discontinuities uses discontinuous data representation across the cell interfaces. The discontinuities in solution are matched with the set of the jumps aligned with the cell faces. For a one dimensional case this will be a proper presentation and there are many ways to get efficient and accurate numerical simulation of the problem. For multidimensional problems this type of representation is questionable for the shock or contact surfaces which are oblique to the mesh. The most popular example of such misrepresentation is an oblique shear wave that if resolved by an interface -oriented Rieman solver will be numerically modelled as a combination of a shear wave along the cell face and two acoustic waves normal to the cell face [68]. In search for the approach that will incorporate a continuous data representation and upwind ideas, the group which is involved in developing of the fluctuation splitting methods [30] constructed efficient techniques for the scalar conservation laws and for the two-dimensional Euler equations [21].

2.3.1 Scalar Fluctuation Splitting Schemes

The fluctuation splitting approach uses continuous data representation in terms of linear shape functions ω_i that changes from unity at the (x_i, y_i) location to zero at the rest of the vertices of the triangles meeting at the i node. These triangles define the *support* of this function and the function is zero outside of this support, see Figure 2.1. The approximation has the following form

$$u(x, y, t) = \sum_i u_i(t)\omega_i(x, y) \tag{2.41}$$

where $u_i(t)$ is the value of the approximated function at the node i. In the following discussion we will use the arbitrary triangle T as a control volume, see Figure 2.2.

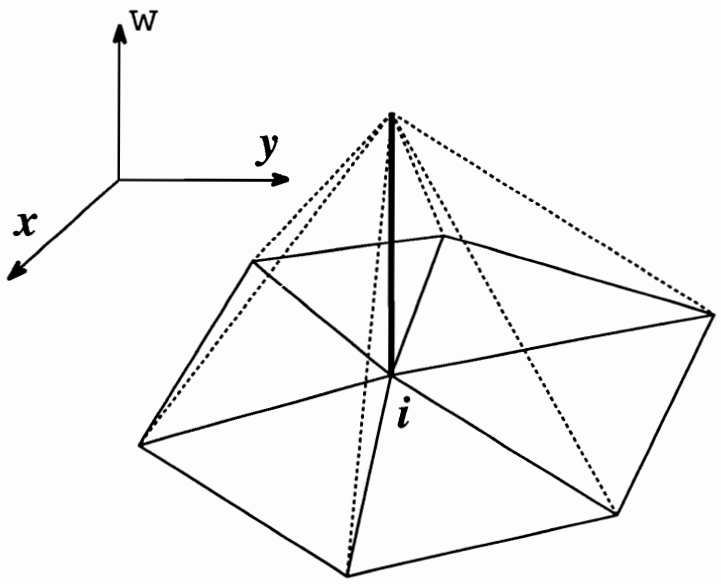

Figure 2.1: The 2D linear shape function.

The normal vectors $\bar{n}_l$ have been scaled with the corresponding edge length

$$\bar{n}_1 = \hat{n}_1 E_1 = (y_2 - y_3)\vec{1}_x - (x_2 - x_3)\vec{1}_y, \tag{2.42}$$

and the other two normals are calculated using circular permutation of $(1, 2, 3)$ indices. For the scaled normals we can formulate the following relation

$$\bar{n}_1 + \bar{n}_2 + \bar{n}_3 = \bar{0}. \tag{2.43}$$

For the vector field $\bar{c}$ we will define the inflow parameter, scalar

$$k_l = \frac{1}{2}\bar{c} \cdot \bar{n}_l \tag{2.44}$$

that will determine the *inflow* and *outflow* edges, and corresponding to them *downstream* and *upstream* nodes

$$\begin{aligned} \text{inflow face:} \quad & k_l \geq 0 \quad l \text{ is a downstream node;} \\ \text{outflow face:} \quad & k_l < 0 \quad l \text{ is an upstream node.} \end{aligned} \tag{2.45}$$

The above definition and the relation (2.43) imply that there are two situations determined by the geometry of the triangle and the local flow direction $\bar{c}$. If one of the

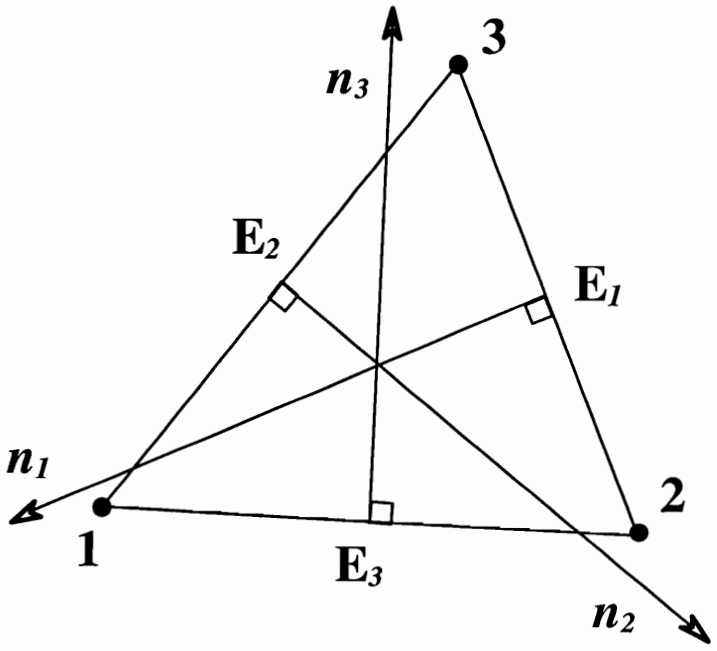

Figure 2.2: A triangular control volume T.

k_l is positive and the other two are negative then we have the triangle with one inflow side and one downstream node, see Figure 2.3. In the situation when one of the k_l is negative and the other two positive we have two inflow sides and two downstream nodes as shown in Figure 2.4.

For the first case we define the outflow point

$$\vec{r}_{out} = \frac{\sum_l max(0, k_l)\vec{r}_l}{\sum_l max(0, k_l)}, \tag{2.46}$$

where $\vec{r}_l$ is the position vector for the node l. The outflow point P_{out} corresponds to the streamline passing through the inflow node, see Figure 2.4. The linear approximation for the function (nf_0) at the outflow point is

$$(nf_0)_{out} = \frac{\sum_l max(0, k_l)(nf_0)_l}{\sum_l max(0, k_l)}. \tag{2.47}$$

The time evolution of the solution that is governed by the scalar advection equation (2.17) is determined by the residual in each triangle. The residual or fluctuation in the triangle T is represented by the integration

$$\phi_T = -\int\int_{V_T} \frac{\partial}{\partial t}(nf_0)dV = \oint_{\delta V_T} (nf_0)(\bar{\mathbf{c}} \cdot \hat{\mathbf{n}}_o)dS =$$

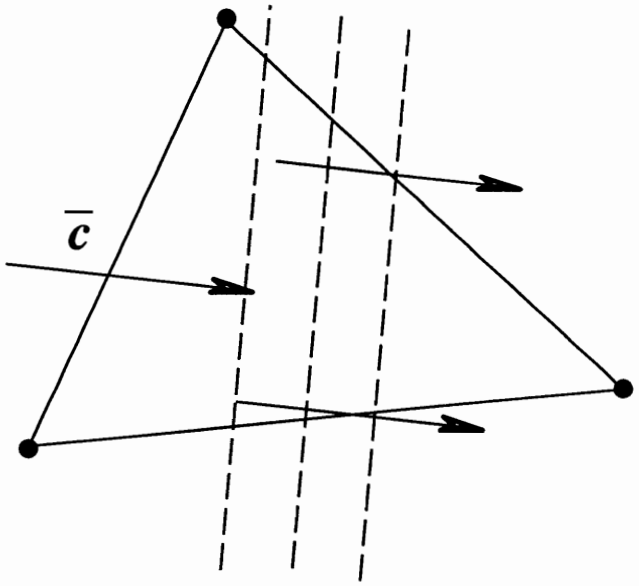

Figure 2.3: One inflow side triangle.

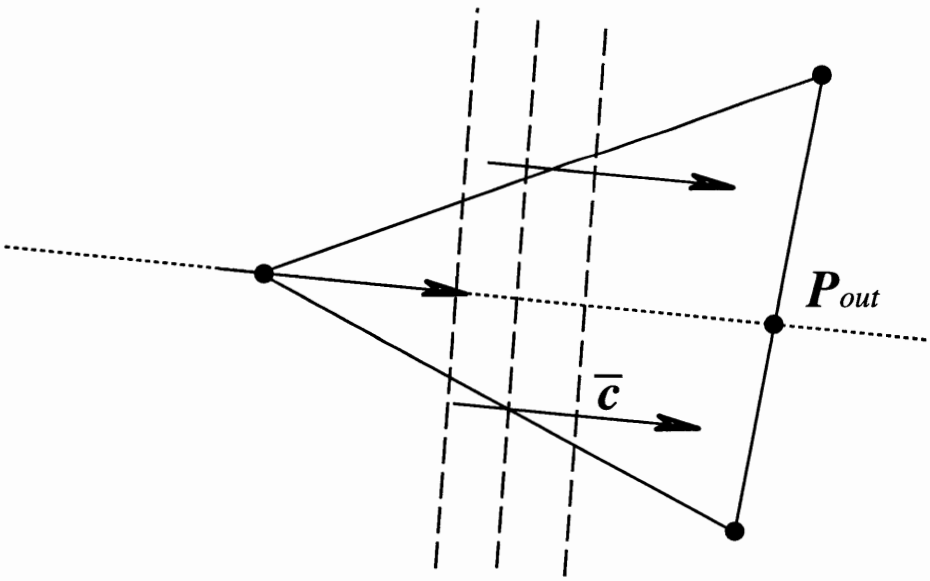

Figure 2.4: Two inflow side triangle.

$$\frac{1}{2}[(nf_0)_1 + (nf_0)_2]\bar{\boldsymbol{c}} \cdot \bar{\boldsymbol{n}}_3 + \frac{1}{2}[(nf_0)_2 + (nf_0)_3]\bar{\boldsymbol{c}} \cdot \bar{\boldsymbol{n}}_1 + \frac{1}{2}[(nf_0)_3 + (nf_0)_1]\bar{\boldsymbol{c}} \cdot \bar{\boldsymbol{n}}_2 \quad (2.48)$$

where we used the piecewise linear representation for the distribution function (nf_0), i.e. Equation (2.41) with $u = (nf_0)$. In addition we will use several equivalent formulations for the flux residual ϕ_T, in particular

$$\phi_T = -\frac{1}{2}\sum_{l=1}^{3}(nf_0)_l(\bar{\boldsymbol{c}} \cdot \hat{\boldsymbol{n}}_l), \quad (2.49)$$

and

$$\begin{aligned} \phi_T &= -\frac{(\bar{\boldsymbol{c}} \cdot \hat{\boldsymbol{n}}_1)}{2}[((nf_0)_1 - (nf_0)_3] - \frac{(\bar{\boldsymbol{c}} \cdot \hat{\boldsymbol{n}}_2)}{2}[((nf_0)_2 - (nf_0)_3], \quad (2.50)\\ &= -\frac{(\bar{\boldsymbol{c}} \cdot \hat{\boldsymbol{n}}_2)}{2}[((nf_0)_2 - (nf_0)_1] - \frac{(\bar{\boldsymbol{c}} \cdot \hat{\boldsymbol{n}}_3)}{2}[((nf_0)_3 - (nf_0)_1],\\ &= -\frac{(\bar{\boldsymbol{c}} \cdot \hat{\boldsymbol{n}}_3)}{2}[((nf_0)_3 - (nf_0)_2] - \frac{(\bar{\boldsymbol{c}} \cdot \hat{\boldsymbol{n}}_1)}{2}[((nf_0)_1 - (nf_0)_2]. \end{aligned}$$

Introducing the value $(nf_0)_{out}$ the fluctuation transforms to the following expression

$$\phi_T = \sum_l max(0, k_l)((nf_0)_{out} - (nf_0)_{in}). \quad (2.51)$$

The fluctuation vanishes and the grid cell is in equilibrium if the function (nf_0) is *streamwise invariant* and the difference $((nf_0)_{out} - (nf_0)_{in})$ is zero.

The core of the fluctuation splitting method is the distribution process that sends fractions of the calculated fluctuation to the surrounding nodes in a conservative manner. The explicit global update scheme includes contributions from all triangles that have a particular node as a vertex

$$\begin{aligned} (nf_0)_i^{n+1} &= (nf_0)_i^n - \frac{\Delta t}{S_i}\sum_T \beta_{l_i}^T \phi^T \quad (2.52)\\ &= (nf_0)_i^n - \frac{\Delta t}{S_i}\sum_T \beta_{l_i}^T \left(\sum_{l=1}^{3} k_l u_l^n\right), \end{aligned}$$

where Δt is the time step, S_i is the area of the median dual cell around node i, Figure 2.5, and $\beta_{l_i}^T$ is the weight-factor of this node i corresponding to the distribution in the T-triangle. This distribution scheme for an arbitrary triangle cell T is written as

$$(nf_0)_l^{n+1} = (nf_0)_l^n - \frac{\Delta t}{S_l}\beta_l^T \phi^T, \quad l = 1, 2, 3. \quad (2.53)$$

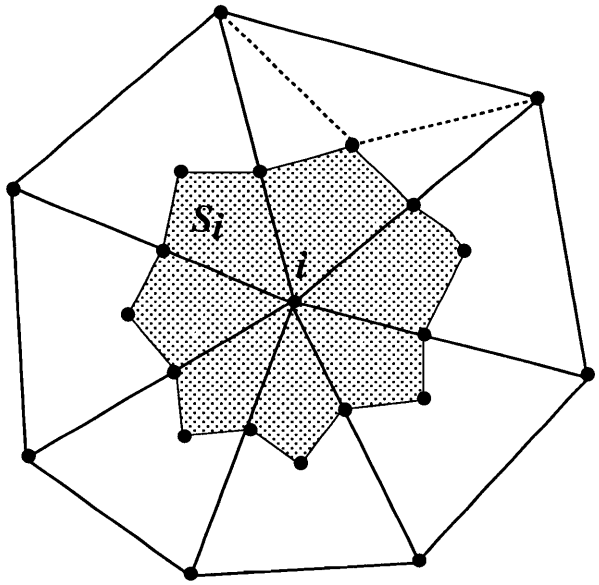

Figure 2.5: Median dual cell.

The conservation principle can be defined in terms of weight-factors for each triangle

$$\beta_1^T + \beta_2^T + \beta_3^T = 1. \tag{2.54}$$

In the construction of this distribution authors [29], [30], [21] imposed compactness conditions: the distribution is limited to the nodes of the triangle itself. The stencil of such an update, Figure 2.6, is less then the support of the linear shape function ω_i. For the velocity directed as shown on Figure 2.6 only grey triangles will contribute to the upgrade at the i node.

The method is conservative by design. The sum of all fluctuations over the computational domain is the sum of the fluxes on all interfaces most of which will cancel out reducing this sum to the boundaries of the domain

$$\sum_T \frac{((nf_0)_i^{n+1} - (nf_0)_i^n)}{\Delta t} S_i = -\sum_T \sum_{T_i} \beta_{l_i}^T \phi^T =$$

$$-\sum_T \phi^T(\beta_1^T + \beta_2^T + \beta_3^T) = -\sum_T \phi^T = \tag{2.55}$$

$$-\sum_T \oint_{\delta V_T} \vec{F} \cdot \hat{n} dS = -\oint_{\delta V_{domain}} \vec{F} \cdot \hat{n} dS.$$

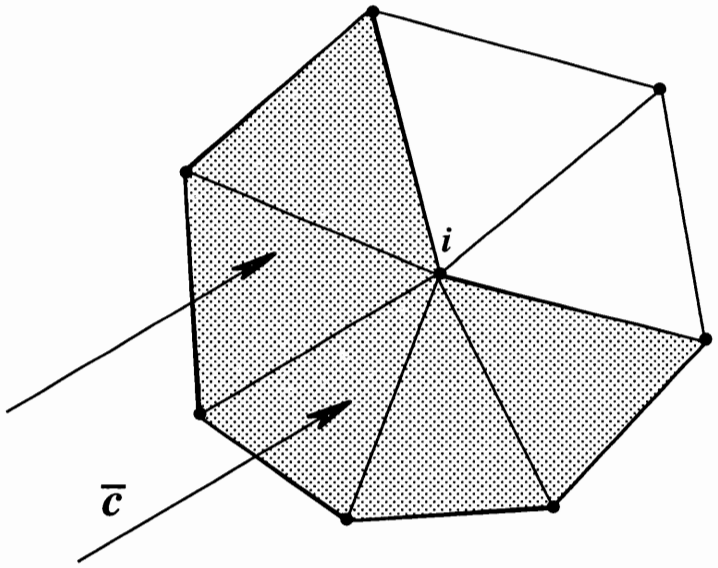

Figure 2.6: Upwind stencil for the fluctuation distribution scheme.

The time marching scheme (2.53) could be written in a more general formulation

$$(nf_0)_i^{n+1} = \sum_k c_k (nf_0)_k^n, \tag{2.56}$$

and the consistency condition will require that $\sum_k c_k = 1$. The c_k coefficients could be the function of (nf_0) and the scheme will be regarded as *non-linear*; the *linear* schemes have coefficients that are independent of (nf_0).

In addition to the consistency condition, there are two main design criteria applied to the fluctuation splitting schemes. The positivity of the scheme requires that $(nf_0)_i^{n+1}$ to be a convex combination of the values at the previous time step $(nf_0)_i^n$; or, in other words $c_k \geq 0$ for every k that included into the sum (2.56). The second criterion is called linearity preservation and according to Sidilkover [37] enforces that for zero fluctuation on the triangle T, none of the vertices of the triangle receive update. This means that the scheme will preserve an exact steady-state solution of Equation (2.17) when that solution is a linear function of spatial coordinates.

The positivity is the multi-dimensional replacement for monotonicity conditions. It was used in numerous investigations as a tool in design of the non-oscillating

schemes on unstructured meshes [30], [69], [34]. The concept was developed for two-dimensional scheme on structured grid by Spekreijse [20] and the more general approach of Local Extremum Diminishing (LED) by Jameson [22] became a useful tool for the design of non-oscillatory second order schemes applicable to structured and unstructured meshes. Together with consistency condition the positivity prevents the generation of new extrema. The local analysis, i.e. limited to each cell contribution, provides simple limits on β_i^T and time step ΔT but it is more restrictive then original requirements.

The linearity preserving property is often linked to the accuracy of the scheme. Indeed, based on Taylor expansions for the two dimensional convection operators developed by Hirsch [70], the linear preservation is equivalent to the second order accuracy for structured meshes. Paillere [35] gives a conservative local truncation error analysis for the fluctuation splitting on the arbitrary grid triangulation. According to him, we still can expect second order accuracy from linear preserving schemes on unstructured grids and for a nonuniform choice of diagonals on structured grids.

The combination of the positivity and linearity preservation is the desirable situation in the design of the methods. Unfortunately, for the linear schemes these two properties are incompatible. According to Struijs [71] the two dimensional extension of the Godunov's theorem for convection on unstructured meshes will exclude the possibility of the linear scheme to be positive and linearity preserving at the same time. If we consider the schemes with c_k coefficients as functions of (nf_0) then we can obtain that combination of properties for the expanse of the additional complications with nonlinearities.

2.3.2 N Scheme

One of the first linear schemes developed for fluctuation splitting on triangles was the N-scheme. Its narrow stencil and largest time-step among linear positive scheme are combined with the least truncation error in its class [47]. Sometimes it is called the optimal linear scheme. Moreover, for the situation when the advection is aligned with one a the cell edges, it gives an exact solution. At the same time, it does not

satisfy the linearity preserving for the two inflow edges triangles.

Using the classification of one and two-inflow sided triangles the N-scheme includes two strategies. For the triangle with one inflow side and one downstream node as in Figure 2.3, the entire fluctuation is passed to that node and the β coefficient for this node is 1, leaving zeros to the other two. For the inflow through the E_3 side, i.e. when $\bar{\boldsymbol{c}} \cdot \hat{\boldsymbol{n}}_3 > 0$ and $\bar{\boldsymbol{c}} \cdot \hat{\boldsymbol{n}}_{(1),(2)} < 0$, the local updates will be

$$
\begin{aligned}
(nf_0)_1^{n+1} &= (nf_0)_1^n, \\
(nf_0)_2^{n+1} &= (nf_0)_2^n, \\
(nf_0)_3^{n+1} &= (nf_0)_3^n - \frac{\Delta t}{S_3}\left\{\frac{(\bar{\boldsymbol{c}} \cdot \hat{\boldsymbol{n}}_1)}{2}[((nf_0)_1 - (nf_0)_3] - \frac{(\bar{\boldsymbol{c}} \cdot \hat{\boldsymbol{n}}_2)}{2}[((nf_0)_2 - (nf_0)_3]\right\}.
\end{aligned}
\tag{2.57}
$$

To determine the condition for the local positivity we will write the updates for the vertices of the triangle as the following:

$$
(nf_0)_l^{n+1} = \sum_{k=1}^{3} \alpha_k^l (nf_0)_k^n, \qquad l = 1, 2, 3. \tag{2.58}
$$

The positivity conditions $\alpha_k^l \geq 0$ will be satisfied if the time step is limited by

$$
\Delta t \leq \frac{2S_3}{\bar{\boldsymbol{c}} \cdot \hat{\boldsymbol{n}}_3}. \tag{2.59}
$$

The update vanishes for an exact linear solution and no update is sent to any of the nodes. That is the linearity preserving property is satisfied and the accuracy of the second order in space could be attained for the regular triangulation. If the situation is reverse and the side E_3 is the only inflow side, i.e. when $\bar{\boldsymbol{c}} \cdot \hat{\boldsymbol{n}}_3 < 0$ and $\bar{\boldsymbol{c}} \cdot \hat{\boldsymbol{n}}_{(1),(2)} > 0$, the fluctuation will be distributed among two downstream nodes 1 and 2. According to the upwind idea, no fluctuation will be sent to the upstream node 3. The optimal distribution for the other two nodes is based on velocity components along the appropriate edges and defined by Struijs *et.el.* [32] as

$$
\begin{aligned}
(nf_0)_1^{n+1} &= (nf_0)_1^n - \frac{\Delta t}{S_1}\left\{\frac{(\bar{\boldsymbol{c}} \cdot \hat{\boldsymbol{n}}_1)}{2}[((nf_0)_1 - (nf_0)_3]\right\}, \\
(nf_0)_2^{n+1} &= (nf_0)_2^n, -\frac{\Delta t}{S_2}\left\{\frac{(\bar{\boldsymbol{c}} \cdot \hat{\boldsymbol{n}}_2)}{2}[((nf_0)_2 - (nf_0)_3]\right\}, \\
(nf_0)_3^{n+1} &= (nf_0)_3^n.
\end{aligned}
\tag{2.60}
$$

The positivity condition will transform to the following

$$\Delta t \leq min\left[\frac{2S_1}{\bar{\boldsymbol{c}}\cdot\hat{\boldsymbol{n}}_1}, \frac{2S_2}{\bar{\boldsymbol{c}}\cdot\hat{\boldsymbol{n}}_2}\right]. \tag{2.61}$$

For the exact linear solution the updates in equations (2.61) will be equal in absolute value but with opposite sign. The cell fluctuation is zero but the nodes will receive updates from this and the rest of the node adjacent triangles. Two-inflow side cells will reduce the accuracy of the scheme to the first order in space. No mesh can be constructed of only one inflow side triangles. As a result, N schemes preserves monotone profiles through discontinuities but they lack the desired high resolution of the flow features due to excessive diffusion.

2.3.3 Low Diffusion scheme

The Low Diffusion (LDA) scheme is a higher-order linear scheme that satisfies the linearity preserving (LP) property. The LDA-scheme lacks the positivity (P) property and may produce oscillations around discontinuities, but will otherwise be second-order accurate for smooth solutions and grids [72].

The LDA-scheme may be developed by again considering triangles with one and two inflow sides. For a one inflow-side triangle shown in Figure 2.3, the LDA-Scheme satisfies both properties P and LP, sending the entire fluctuation to the downstream node. This update is identical to that for the N-Scheme given by Equation (2.58), and is locally positive under conditions expressed by Equation (2.59).

For the triangle with two inflow sides, shown in Figure 2.4, the general distribution scheme, Equation (2.53) will be linearity preserving when the coefficients β_l^T are bounded. The LDA-scheme for this case is developed by considering the intersection of the triangle with the streamline passing through the upstream vertex and crossing the outflow side at the point P_{out} as illustrated in Figure 2.7. According to the LDA-scheme the downstream nodes 1 and 2 will receive the fluctuations Φ_1 and Φ_2 corresponding to the adjacent subtriangles 314 and 324 respectively, as shown in Figure 2.7. The interpolated value at the outflow point 4 in terms of the values on the vertices is presented by Equation (2.47). Taking into account the fact that the

line connecting nodes 3 and 4 coincides with the streamline, it may be shown that

$$\Phi_1 = -\frac{\bar{\boldsymbol{c}} \cdot \bar{\boldsymbol{n}}_1}{2}[(nf_0)_4 - (nf_0)_3]\,, \tag{2.62}$$
$$\Phi_2 = -\frac{\bar{\boldsymbol{c}} \cdot \bar{\boldsymbol{n}}_2}{2}[(nf_0)_4 - (nf_0)_3]\,.$$

Substituting Eq. (2.47) into Eqs. (2.63), we obtain

$$\Phi_i = -\frac{\bar{\boldsymbol{c}} \cdot \bar{\boldsymbol{n}}_i}{\bar{\boldsymbol{c}} \cdot \bar{\boldsymbol{n}}_1 + \bar{\boldsymbol{c}} \cdot \bar{\boldsymbol{n}}_2}\{\bar{\boldsymbol{c}} \cdot \bar{\boldsymbol{n}}_2[(nf_0)_2 - (nf_0)_3] + \bar{\boldsymbol{c}} \cdot \bar{\boldsymbol{n}}_1[(nf_0)_1 - (nf_0)_3]\}\,, \qquad i = 1, 2\,, \tag{2.63}$$

and the LDA-scheme for the two inflow-side case may given by

$$\begin{aligned} (nf_0)_1^{\,n+1} &= (nf_0)_1^{\,n} + \frac{\Delta t}{S_1} \cdot \Phi_1\,, \\ (nf_0)_2^{\,n+1} &= (nf_0)_2^{\,n} + \frac{\Delta t}{S_2} \cdot \Phi_2\,, \\ (nf_0)_3^{n+1} &= (nf_0)_3^{n}. \end{aligned} \tag{2.64}$$

This case may lead to updates which are not positive and may give rise to non-monotone profiles through discontinuities. In our calculation we used the time step limit imposed by the one inflow side case, that is the same for the N - scheme and LDA - scheme, see Equation (2.59). Less restrictive constraint for the steady-state calculations was suggested by Mesaros [36]. It uses the global update formulation Equation (2.53) resulting in the following time step for the vertex i and adjacent triangle cells

$$\Delta t_i \leq \frac{S_i}{\sum_T max(0, \bar{\boldsymbol{c}} \cdot \hat{\boldsymbol{n}})}. \tag{2.65}$$

2.4 Multi-Dimensional Euler Solvers

Multi-dimensional Euler schemes presented in this chapter are Boltzmann type scheme on Cartesian grids with the Maxwellian velocity distribution function. The brief description of the N-scheme integration and detailed integration of the LDA - scheme will be presented. The original and detailed discussion of the procedure for N - scheme was

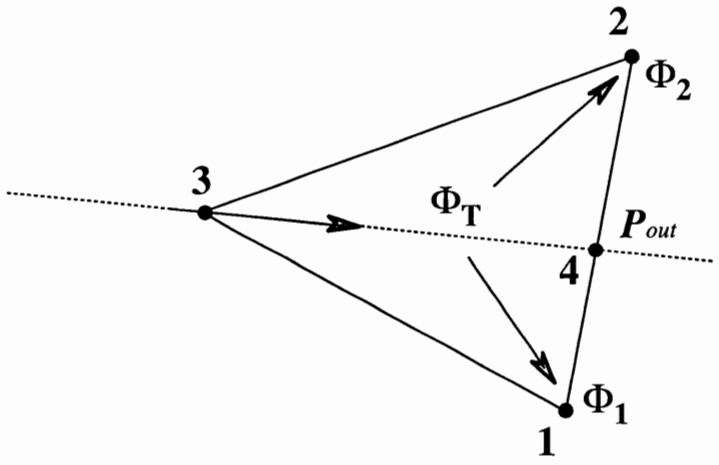

Figure 2.7: Upwind stencil for the fluctuation distribution scheme.

given by Eppard [73]. We will follow here the same notations and the Multi - dimensional Kinetic Fluctuation Splitting (MKFS) based on the N-scheme with adaptive diagonalization will be referenced as MKFS-NDA scheme to distinguish it from the scheme based on unidirected triangulation. The LDA scheme was constructed using the adaptive strategy and to avoid redundancy we call it MKFS-LDA scheme.

The update of the conserved-variable vector, $\boldsymbol{Q}$, is calculated by collecting the portions of fluctuations $\Delta(nf_0)_i^T$ from the triangles that meet at the node i and taking the moments in the Maxwellian velocity distribution function. The efficiency of the code required that the integration was performed analytically rather then using numerical approximations. By definition, Equation (2.23), the general formulation for the global update could be rewritten as

$$\Delta \boldsymbol{Q}_i = \int_{-\infty}^{\infty}\int_{-\infty}^{\infty}\int_{-\infty}^{\infty} \boldsymbol{\Psi} \sum_T \Delta(nf_0)_i^T dc_1 dc_2 dc_3, \tag{2.66}$$

and the integration procedure will depend on the decomposition of the velocity space since different direction of the space vector will determine which combination of the one-inflow and two-inflow sided triangles we will have to consider. So, the velocity space will be only divided on sectors, each extends from the center of coordinates to infinity. It has to be mentioned that for the nonlinear schemes, when the distribution procedure will be determined not only by geometry of the cell and a direction of the

velocity vector but by the absolute value of the vector also, the resulting decomposition of the velocity space will be much more complex. The subdomains of integration will be described by the algebraic equations and the analytical integration will be unreasonably complex.

Equation (2.66) has a deficiency in a sense that we have to loop over every node to calculate the updates and for each node we have to consider all triangles in the support of the ω_i. The supports for nodes have a great deal of overlapping and we can reduce computational efforts by looping over cells and calculating their contribution to the different nodes, later summarizing those to form the global update. For the structured rectangular grids we can take advantage of looping over the rectangular cells, split by diagonals and use our results for triangles. We calculate contributions of the cells to their four vertices and the compactness of the numerical procedure give us freedom to use multi-processing and vectorizing, which are crucial for complex computations of real flows.

2.4.1 Kinetic NDA Scheme

Three different multidimensional schemes for the Cartesian meshes has been designed by Eppard and Grossman [60]. All three constructed for the uniform orthogonal meshes where each rectangular cell is split into two triangles and the direction of the diagonal determine the scheme. The first two schemes, MKFS-NDD and MKFS-NDU, used the diagonal going downward and upward respectively. All cells in the domain had the same direction. The third version called diagonal-adaptive scheme is more complicated and includes the idea of adjusting the diagonal to be either up or down depending on the quarter of the velocity space.

The global and local numbering systems for the rectangular cell and its triangular subcells are shown in Figure 2.8 for the triangulation with the diagonal pointed down to the right and in Figure 2.9 for the diagonal going up. The dashed lines indicate the orientation of the diagonals for the rectangular cell with the sides Δx_1 and Δx_2 in the x_1 and x_2 directions. For each case we marked in the parenthesis the nodes that receive the portion of the fluctuation.

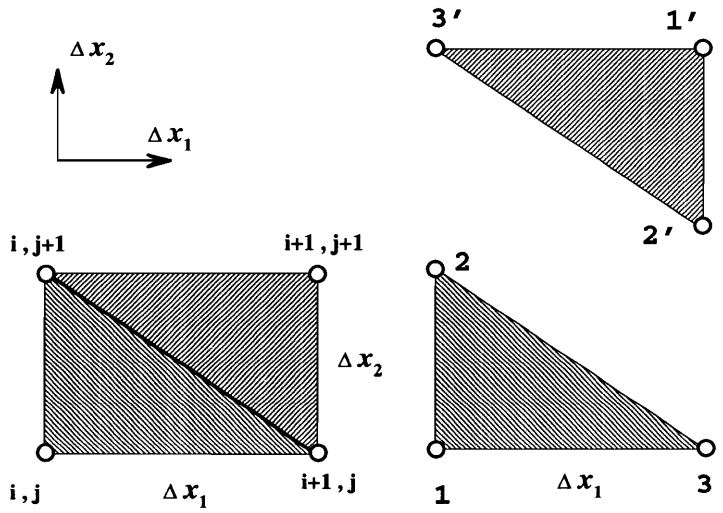

Figure 2.8: Grid cell splitting for the down diagonal scheme.

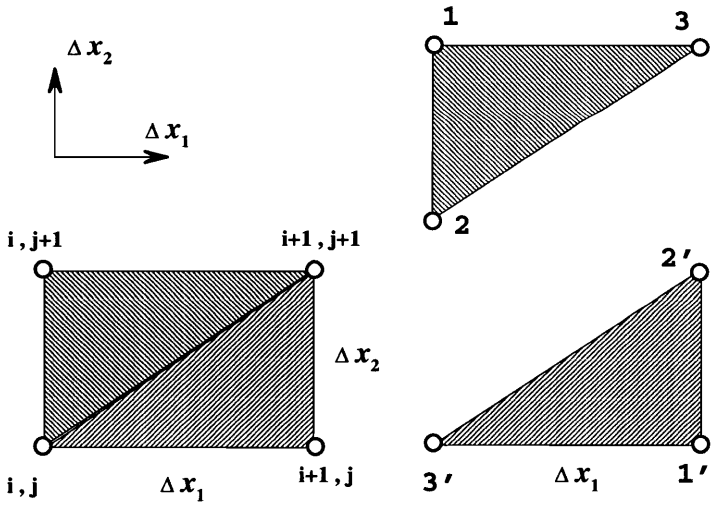

Figure 2.9: Grid cell splitting for the upward diagonal scheme.

Each node inside the domain will have to collect the updates from the four rectangular cells surrounding it or six triangles that have this node as a vertex. If we consider a single rectangular cell and the two triangles in it, then we will have to recognize six combinations, based on the velocity direction. Each triangle can have one of its three vertices either as upstream or downstream that makes six cases. The velocity space decomposition for the MKFS-NDD and MKFS-NDU scheme will be determined by these six cases and the integration in Equation (2.66) could be done analytically within each of the velocity subdomains, as shown in Figures 2.10 and 2.11. For example, the integration for the MKFS-NDD will be given as

$$\begin{aligned}\Delta \boldsymbol{Q} \;=\; \int_{-\infty}^{\infty} \Big\{ & \int_{-\infty}^{0}\int_{-\infty}^{0} \boldsymbol{\Psi}\Delta(nf_0)^{(1)} dc_2 dc_1 \\ & + \int_{-\infty}^{0}\int_{-c_1\alpha}^{\infty} \boldsymbol{\Psi}\Delta(nf_0)^{(2)} dc_2 dc_1 \\ & + \int_{0}^{\infty}\int_{-c_1\alpha}^{0} \boldsymbol{\Psi}\Delta(nf_0)^{(3)} dc_2 dc_1 \\ & + \int_{-\infty}^{0}\int_{0}^{-c_1\alpha} \boldsymbol{\Psi}\Delta(nf_0)^{(4)} dc_2 dc_1 \\ & + \int_{0}^{\infty}\int_{-\infty}^{-c_1\alpha} \boldsymbol{\Psi}\Delta(nf_0)^{(5)} dc_2 dc_1 \\ & + \int_{0}^{\infty}\int_{0}^{\infty} \boldsymbol{\Psi}\Delta(nf_0)^{(6)} dc_2 dc_1 \Big\} dc_3,\end{aligned} \tag{2.67}$$

where the α is the cell aspect ration defined by

$$\alpha = \frac{\Delta x_2}{\Delta x_1}. \tag{2.68}$$

This expression could be simplified even more if we recognize the fact that due to the upwind strategy used for triangles no more then four velocity subspaces will contribute to the integration for each node. If we combine the Figures 2.8 and 2.10 with simple one/two inflow side classification, then regardless of the distribution scheme, as long as it is upwind the following velocity subspaces will contribute to the local updates for the MKFS-NDD scheme:

$$\Delta \boldsymbol{Q}_{i,j} = \Delta \boldsymbol{Q}^{(1)}_{i,j} + \Delta \boldsymbol{Q}^{(4)}_{i,j} + \Delta \boldsymbol{Q}^{(5)}_{i,j}, \tag{2.69}$$

$$\Delta \boldsymbol{Q}_{i+1,j} = \Delta \boldsymbol{Q}^{(1)}_{i+1,j} + \Delta \boldsymbol{Q}^{(3)}_{i+1,j} + \Delta \boldsymbol{Q}^{(5)}_{i+1,j} + \Delta \boldsymbol{Q}^{(6)}_{i+1,j}, \tag{2.70}$$

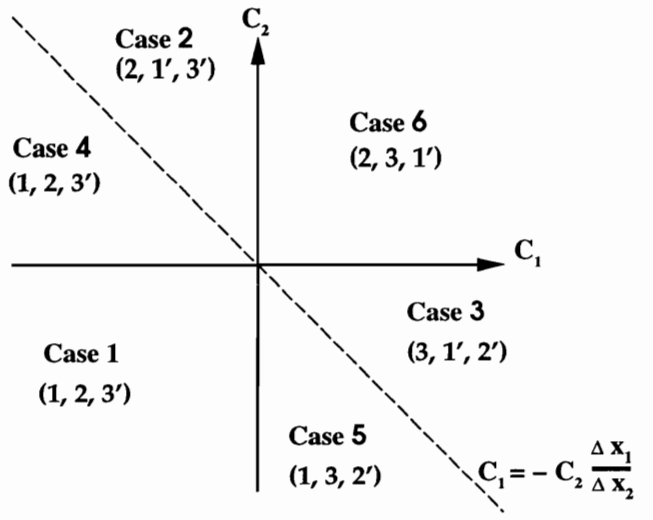

Figure 2.10: Velocity space decomposition for the down diagonal triangulation.

$$\Delta \boldsymbol{Q}_{i,j+1} = \Delta \boldsymbol{Q}^{(1)}_{i,j+1} + \Delta \boldsymbol{Q}^{(2)}_{i,j+1} + \Delta \boldsymbol{Q}^{(4)}_{i,j+1} + \Delta \boldsymbol{Q}^{(6)}_{i,j+1}, \tag{2.71}$$

$$\Delta \boldsymbol{Q}_{i+1,j+1} = \Delta \boldsymbol{Q}^{(2)}_{i+1,j+1} + \Delta \boldsymbol{Q}^{(3)}_{i+1,j+1} + \Delta \boldsymbol{Q}^{(6)}_{i+1,j+1}. \tag{2.72}$$

The updates for the MKFS-NDU scheme after proper velocity space decomposition become

$$\Delta \boldsymbol{Q}_{i,j} = \Delta \boldsymbol{Q}^{(1')}_{i,j} + \Delta \boldsymbol{Q}^{(4')}_{i,j} + \Delta \boldsymbol{Q}^{(2')}_{i,j} + \Delta \boldsymbol{Q}^{(6')}_{i+1,j}, \tag{2.73}$$

$$\Delta \boldsymbol{Q}_{i+1,j} = \Delta \boldsymbol{Q}^{(2')}_{i+1,j} + \Delta \boldsymbol{Q}^{(3')}_{i+1,j} + \Delta \boldsymbol{Q}^{(6')}_{i+1,j}, \tag{2.74}$$

$$\Delta \boldsymbol{Q}_{i,j+1} = \Delta \boldsymbol{Q}^{(1')}_{i,j+1} + \Delta \boldsymbol{Q}^{(4')}_{i,j+1} + \Delta \boldsymbol{Q}^{(5')}_{i,j+1}, \tag{2.75}$$

$$\Delta \boldsymbol{Q}_{i+1,j+1} = \Delta \boldsymbol{Q}^{(1')}_{i+1,j+1} + \Delta \boldsymbol{Q}^{(5')}_{i+1,j+1} + \Delta \boldsymbol{Q}^{(3')}_{i+1,j+1} + \Delta \boldsymbol{Q}^{(6')}_{i+1,j+1}. \tag{2.76}$$

Each part of these two sets of expression has to be integrated for each component of the vector $\boldsymbol{\Psi}$. The resulting 48 integrals and final expressions for the updates in terms of these integrals are presented in the Appendix A.

Two schemes with preset diagonal orientation exhibit diagonal dependence since for the cases 1, 6, 1', and 6' the projection of the velocity on the diagonal is close to zero and the cross diffusion in its maximum, degrading quality of a solution to the one for dimensional-split first order schemes. This issue of directional dependence is discussed in [32] and numerical experiments with MKFS-NDU, MKFS-NDD

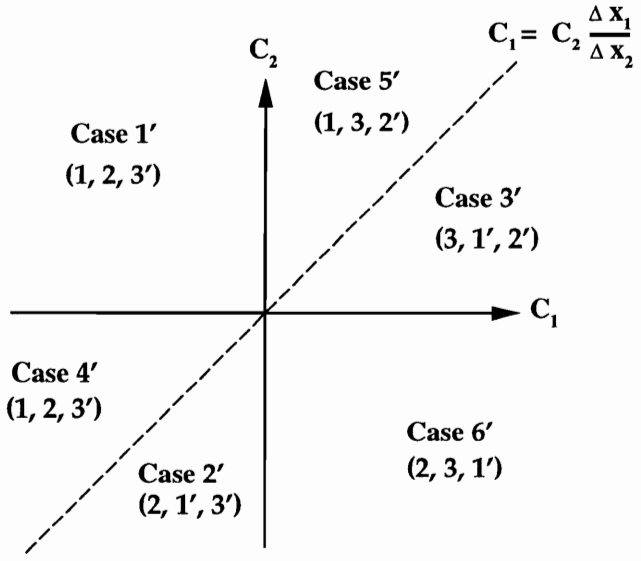

Figure 2.11: Velocity space decomposition for the upward diagonal triangulation.

schemes confirmed the problem. The elimination of this dependence was achieved by introducing the adaptive strategy into triangulation process, when the appropriate diagonal is chosen and the scheme is optimal in each velocity subspace. Eppard and Grossman [60] blended the two previous schemes in the following manner

$$\begin{aligned} \text{first and third quadrants:} \quad & c_1 \cdot c_2 > 0 \quad \text{MKFS-NDU is active;} \\ \text{second and fourth quadrants:} \quad & c_1 \cdot c_2 < 0 \quad \text{MKFS-NDD is active;} \end{aligned} \tag{2.77}$$

and the splitting method is illustrated in Figure 2.12. The velocity space has eight subspaces for eight cases that are shown in Figure 2.13 and for each vertex of the rectangular cell there are four velocity space subdomains contributing to its update. Despite visible complexity this adaptive procedure appears only at the kinetic level and the Euler scheme does not include any extra logical steps except for a few more integrals to compute.

2.4.2 Kinetic LDA Scheme

The MKFS-LDA scheme is based upon the application of the LDA-scheme at the kinetic level to a Cartesian triangulation with the orientation of the diagonal depending upon the velocity space quadrant. We use the same adaptive split-diagonal

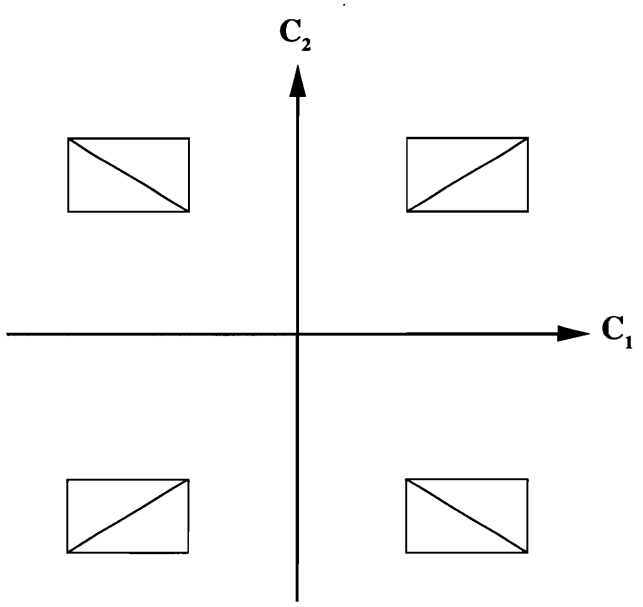

Figure 2.12: Adaptive triangulation.

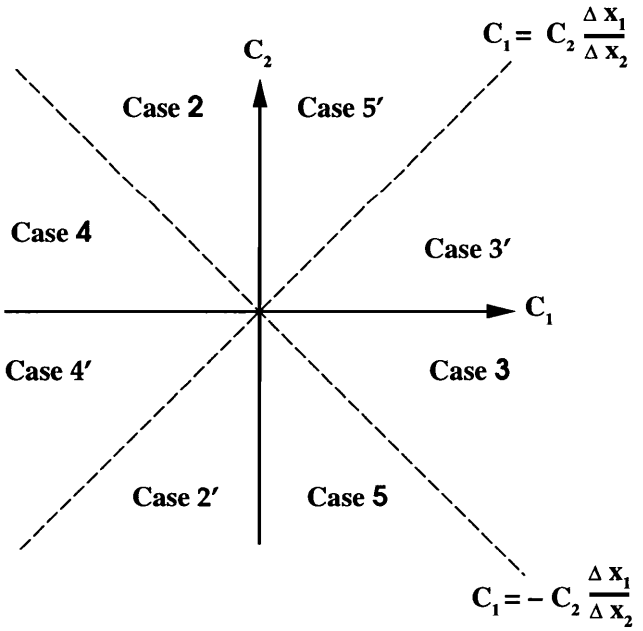

Figure 2.13: Velocity space decomposition for the adaptive triangulation.

approach, sketched in Figure 2.12, and the same velocity space decomposition, illustrated in Figure 2.13, as implemented in the NDA scheme. The fluctuations in the second and fourth velocity space quadrants are considered for a triangulation with the diagonal pointed down and to the right, *i.e.*, cases 2 – 5 in our notation. The fluctuations are calculated utilizing the Equation (2.58) for the one inflow-side triangles and Equations (2.63) and (2.65) for the two inflow-side triangles. The resulting global fluctuations for these two velocity space quadrants are given as:

$$\begin{aligned}
\Delta(nf_0)^{(2)}_{i,j+1} &= \frac{\nu_1}{2}\left[(nf_0)_{i,j} + (nf_0)_{i+1,j+1} - 2(nf_0)_{i+1,j}\right] + \frac{\nu_2}{2}\left[(nf_0)_{i,j}\right. \\
&\quad \left. -(nf_0)_{i,j+1}\right] + \frac{\nu_1^2}{2\nu_2}\left[(nf_0)_{i+1,j+1} - (nf_0)_{i,j+1}\right], \qquad (2.78) \\
\Delta(nf_0)^{(2)}_{i+1,j+1} &= \frac{\nu_1}{2}\left[(nf_0)_{i+1,j} + (nf_0)_{i,j+1} - 2(nf_0)_{i+1,j+1}\right] + \frac{\nu_2}{2}\left[(nf_0)_{i+1,j}\right. \\
&\quad \left. -(nf_0)_{i+1,j+1}\right] + \frac{\nu_1^2}{2\nu_2}\left[(nf_0)_{i,j+1} - (nf_0)_{i+1,j+1}\right], \qquad (2.79) \\
\Delta(nf_0)^{(3)}_{i+1,j} &= \frac{\nu_1}{2}\left[(nf_0)_{i,j} - (nf_0)_{i+1,j}\right] + \frac{\nu_2}{2}\left[(nf_0)_{i,j} + (nf_0)_{i+1,j+1}\right. \\
&\quad \left. -2(nf_0)_{i,j+1}\right] + \frac{\nu_2^2}{2\nu_1}\left[(nf_0)_{i+1,j+1} - (nf_0)_{i+1,j}\right], \qquad (2.80) \\
\Delta(nf_0)^{(3)}_{i+1,j+1} &= \frac{\nu_1}{2}\left[(nf_0)_{i,j+1} - (nf_0)_{i+1,j+1}\right] + \frac{\nu_2}{2}\left[(nf_0)_{i+1,j} + (nf_0)_{i,j+1}\right. \\
&\quad \left. -2(nf_0)_{i+1,j+1}\right] + \frac{\nu_2^2}{2\nu_1}\left[(nf_0)_{i+1,j} - (nf_0)_{i+1,j+1}\right], \qquad (2.81) \\
\Delta(nf_0)^{(4)}_{i,j+1} &= -\frac{\nu_1}{2}\left[(nf_0)_{i+1,j+1} - (nf_0)_{i,j+1}\right] - \frac{\nu_2}{2}\left[(nf_0)_{i+1,j+1} + (nf_0)_{i,j}\right. \\
&\quad \left. -2(nf_0)_{i+1,j}\right] - \frac{\nu_2^2}{2\nu_1}\left[(nf_0)_{i,j} - (nf_0)_{i,j+1}\right], \qquad (2.82) \\
\Delta(nf_0)^{(4)}_{i,j} &= -\frac{\nu_1}{2}\left[(nf_0)_{i+1,j} - (nf_0)_{i,j}\right] - \frac{\nu_2}{2}\left[(nf_0)_{i,j+1} + (nf_0)_{i+1,j}\right. \\
&\quad \left. -2(nf_0)_{i,j}\right] - \frac{\nu_2^2}{2\nu_1}\left[(nf_0)_{i,j+1} - (nf_0)_{i,j}\right], \qquad (2.83) \\
\Delta(nf_0)^{(5)}_{i,j} &= -\frac{\nu_1}{2}\left[(nf_0)_{i,j+1} + (nf_0)_{i+1,j} - 2(nf_0)_{i,j}\right] - \frac{\nu_2}{2}\left[(nf_0)_{i,j+1}\right. \\
&\quad \left. -(nf_0)_{i,j}\right] - \frac{\nu_1^2}{2\nu_2}\left[(nf_0)_{i+1,j} - (nf_0)_{i,j}\right], \qquad (2.84) \\
\Delta(nf_0)^{(5)}_{i+1,j} &= -\frac{\nu_1}{2}\left[(nf_0)_{i,j} + (nf_0)_{i+1,j+1} - 2(nf_0)_{i,j+1}\right] - \frac{\nu_2}{2}\left[(nf_0)_{i+1,j+1}\right. \\
&\quad \left. -(nf_0)_{i+1,j}\right] - \frac{\nu_1^2}{2\nu_2}\left[(nf_0)_{i,j} - (nf_0)_{i+1,j}\right], \qquad (2.85)
\end{aligned}$$

where we defined Courant numbers in the x_1 and x_2 directions respectively as

$$\nu_1 = \frac{c_1 \Delta t}{\Delta x_1}, \tag{2.86}$$

and

$$\nu_2 = \frac{c_2 \Delta t}{\Delta x_2}. \tag{2.87}$$

In the other two quadrants, *i.e.* cases $2' - 5'$, the fluctuations are determined using the LDA-scheme for the triangulation with the diagonal pointed up and to the right. The global fluctuations for these cases can be written in terms of the down-diagonal fluctuations through a symmetry transformation as

$$\begin{aligned}
\Delta(nf_0)^{(m')}_{i,j+1}(\nu_1,\nu_2) &= \Delta(nf_0)^{(m)}_{i,j}(-\nu_1,\nu_2), \\
\Delta(nf_0)^{(m')}_{i+1,j+1}(\nu_1,\nu_2) &= \Delta(nf_0)^{(m)}_{i+1,j}(-\nu_1,\nu_2), \\
\Delta(nf_0)^{(m')}_{i+1,j}(\nu_1,\nu_2) &= \Delta(nf_0)^{(m)}_{i+1,j+1}(-\nu_1,\nu_2), \\
\Delta(nf_0)^{(m')}_{i,j}(\nu_1,\nu_2) &= \Delta(nf_0)^{(m)}_{i,j+1}(-\nu_1,\nu_2),
\end{aligned} \tag{2.88}$$

where $m = 2, \ldots, 5$.

At the Euler level the total fluctuation is determined the same way as for the N scheme, through

$$\Delta \boldsymbol{Q} = \int_{-\infty}^{\infty}\int_{-\infty}^{\infty}\int_{-\infty}^{\infty} \boldsymbol{\Psi} \Delta(nf_0) dc_1 dc_2 dc_3 . \tag{2.89}$$

The integration over the entire velocity space is taken as the integration over eight discrete velocity subspaces shown in Figure 2.13 as

$$\begin{aligned}
\Delta \boldsymbol{Q} = \int_{-\infty}^{\infty} \Big\{ & \int_{-\infty}^{0}\int_{-c_1\alpha}^{\infty} \boldsymbol{\Psi} \Delta(nf_0)^{(2)} dc_2 dc_1 + \int_{0}^{\infty}\int_{-c_1\alpha}^{0} \boldsymbol{\Psi} \Delta(nf_0)^{(3)} dc_2 dc_1 \\
& + \int_{-\infty}^{0}\int_{0}^{-c_1\alpha} \boldsymbol{\Psi} \Delta(nf_0)^{(4)} dc_2 dc_1 + \int_{0}^{\infty}\int_{-\infty}^{-c_1\alpha} \boldsymbol{\Psi} \Delta(nf_0)^{(5)} dc_2 dc_1 \\
& + \int_{-\infty}^{0}\int_{-\infty}^{c_1\alpha} \boldsymbol{\Psi} \Delta(nf_0)^{(2')} dc_2 dc_1 + \int_{0}^{\infty}\int_{0}^{c_1\alpha} \boldsymbol{\Psi} \Delta(nf_0)^{(3')} dc_2 dc_1 \\
& + \int_{-\infty}^{0}\int_{c_1\alpha}^{0} \boldsymbol{\Psi} \Delta(nf_0)^{(4')} dc_2 dc_1 + \int_{0}^{\infty}\int_{c_1\alpha}^{\infty} \boldsymbol{\Psi} \Delta(nf_0)^{(5')} dc_2 dc_1 \Big\} dc_3 ,
\end{aligned} \tag{2.90}$$

where $(nf_0)^{(i)}$ is now given by the LDA-scheme. We assemble all the fluctuations in $\boldsymbol{Q}$ at the four nodes of the rectangular cell. The complete Euler scheme may be written as

$$\begin{aligned}
\Delta\boldsymbol{Q}_{i,j} &= -\frac{\Delta t}{2\Delta x_2}[-\alpha\boldsymbol{I}_{41_{i,j}} - 2\boldsymbol{I}_{42_{i,j}} - \frac{1}{\alpha}\boldsymbol{I}_{48_{i,j}} + \frac{1}{\alpha}\boldsymbol{I}_{48_{i,j+1}} \\
&+\boldsymbol{I}_{42_{i,j+1}} + \alpha\boldsymbol{I}_{41_{i+1,j}} + \boldsymbol{I}_{42_{i+1,j}} - \alpha\acute{\boldsymbol{I}}_{41_{i+1,j}} + \acute{\boldsymbol{I}}_{42_{i+1,j}} \\
&+\alpha\acute{\boldsymbol{I}}_{41_{i,j}} - 2\acute{\boldsymbol{I}}_{42_{i+1,j+1}} + \acute{\boldsymbol{I}}_{42_{i,j+1}} + \frac{1}{\alpha}\acute{\boldsymbol{I}}_{48_{i,j}} - \frac{1}{\alpha}\acute{\boldsymbol{I}}_{48_{i,j+1}}] \\
&-\frac{\Delta t}{2\Delta x_1}[-\alpha\boldsymbol{I}_{57_{i,j}} - 2\boldsymbol{I}_{51_{i,j}} - \frac{1}{\alpha}\boldsymbol{I}_{52_{i,j}} + \frac{1}{\alpha}\boldsymbol{I}_{52_{i,j+1}} \\
&+\boldsymbol{I}_{51_{i,j+1}} + \alpha\boldsymbol{I}_{57_{i+1,j}} + \boldsymbol{I}_{51_{i+1,j}} - \alpha\acute{\boldsymbol{I}}_{27_{i+1,j}} + \acute{\boldsymbol{I}}_{21_{i+1,j}} \\
&+\alpha\acute{\boldsymbol{I}}_{27_{i,j}} - 2\acute{\boldsymbol{I}}_{21_{i+1,j+1}} + \acute{\boldsymbol{I}}_{21_{i,j+1}} + \frac{1}{\alpha}\acute{\boldsymbol{I}}_{22_{i,j}} - \frac{1}{\alpha}\acute{\boldsymbol{I}}_{22_{i,j+1}}]\,,
\end{aligned} \tag{2.91}$$

$$\begin{aligned}
\Delta\boldsymbol{Q}_{i,j+1} &= -\frac{\Delta t}{2\Delta x_2}[\alpha\boldsymbol{I}_{41_{i+1,j+1}} + \boldsymbol{I}_{42_{i+1,j+1}} - \alpha\boldsymbol{I}_{41_{i,j+1}} - 2\boldsymbol{I}_{42_{i+1,j}} \\
&+\boldsymbol{I}_{42_{i,j}} + \frac{1}{\alpha}\boldsymbol{I}_{48_{i,j}} - \frac{1}{\alpha}\boldsymbol{I}_{48_{i,j+1}} + \alpha\acute{\boldsymbol{I}}_{41_{i,j+1}} - 2\acute{\boldsymbol{I}}_{42_{i,j+1}} \\
&+\frac{1}{\alpha}\acute{\boldsymbol{I}}_{48_{i,j+1}} - \frac{1}{\alpha}\acute{\boldsymbol{I}}_{48_{i,j}} + \acute{\boldsymbol{I}}_{42_{i,j}} - \alpha\acute{\boldsymbol{I}}_{41_{i+1,j+1}} + \acute{\boldsymbol{I}}_{42_{i+1,j+1}}] \\
&+\frac{\Delta t}{2\Delta x_1}[\alpha\boldsymbol{I}_{27_{i+1,j+1}} + \boldsymbol{I}_{21_{i+1,j+1}} - \alpha\boldsymbol{I}_{27_{i,j+1}} - 2\boldsymbol{I}_{21_{i+1,j}} \\
&+\boldsymbol{I}_{21_{i,j}} + \frac{1}{\alpha}\boldsymbol{I}_{22_{i,j}} - \frac{1}{\alpha}\boldsymbol{I}_{22_{i,j+1}} + \alpha\acute{\boldsymbol{I}}_{57_{i,j+1}} - 2\acute{\boldsymbol{I}}_{51_{i,j+1}} \\
&+\frac{1}{\alpha}\acute{\boldsymbol{I}}_{52_{i,j+1}} - \frac{1}{\alpha}\acute{\boldsymbol{I}}_{52_{i,j}} + \acute{\boldsymbol{I}}_{51_{i,j}} - \alpha\acute{\boldsymbol{I}}_{57_{i+1,j+1}} + \acute{\boldsymbol{I}}_{51_{i+1,j+1}}]\,,
\end{aligned} \tag{2.92}$$

$$\begin{aligned}
\Delta\boldsymbol{Q}_{i+1,j} &= -\frac{\Delta t}{2\Delta x_2}[-\alpha\boldsymbol{I}_{31_{i,j}} - \boldsymbol{I}_{32_{i,j}} + \frac{1}{\alpha}\boldsymbol{I}_{38_{i+1,j}} - \frac{1}{\alpha}\boldsymbol{I}_{38_{i+1,j+1}} \\
&+2\boldsymbol{I}_{32_{i,j+1}} + \alpha\boldsymbol{I}_{31_{i+1,j}} - \boldsymbol{I}_{32_{i+1,j+1}} - \alpha\acute{\boldsymbol{I}}_{31_{i+1,j}} - \acute{\boldsymbol{I}}_{32_{i,j}} \\
&+\alpha\acute{\boldsymbol{I}}_{31_{i,j}} + 2\acute{\boldsymbol{I}}_{32_{i+1,j}} - \acute{\boldsymbol{I}}_{32_{i+1,j+1}} - \frac{1}{\alpha}\acute{\boldsymbol{I}}_{38_{i+1,j}} + \frac{1}{\alpha}\acute{\boldsymbol{I}}_{38_{i+1,j+1}}] \\
&-\frac{\Delta t}{2\Delta x_1}[\alpha\boldsymbol{I}_{57_{i,j}} - 2\boldsymbol{I}_{51_{i,j+1}} - \frac{1}{\alpha}\boldsymbol{I}_{52_{i+1,j}} + \frac{1}{\alpha}\boldsymbol{I}_{52_{i+1,j+1}} \\
&+\boldsymbol{I}_{51_{i+1,j+1}} - \alpha\boldsymbol{I}_{57_{i+1,j}} + \boldsymbol{I}_{51_{i,j}} - \alpha\acute{\boldsymbol{I}}_{27_{i,j}} + \acute{\boldsymbol{I}}_{21_{i+1,j+1}} \\
&+\alpha\acute{\boldsymbol{I}}_{27_{i+1,j}} - 2\acute{\boldsymbol{I}}_{21_{i+1,j}} + \acute{\boldsymbol{I}}_{21_{i,j}} + \frac{1}{\alpha}\acute{\boldsymbol{I}}_{22_{i+1,j}} - \frac{1}{\alpha}\acute{\boldsymbol{I}}_{22_{i+1,j+1}}]\,,
\end{aligned} \tag{2.93}$$

and

$$\begin{aligned}
\Delta \boldsymbol{Q}_{i+1,j+1} \;=\; & -\frac{\Delta t}{2\Delta x_2}[\alpha \boldsymbol{I}_{31_{i+1,j+1}} - \boldsymbol{I}_{32_{i+1,j}} + \frac{1}{\alpha}\boldsymbol{I}_{38_{i+1,j+1}} - \frac{1}{\alpha}\boldsymbol{I}_{38_{i+1,j}} \\
& +2\boldsymbol{I}_{32_{i+1,j+1}} - \alpha \boldsymbol{I}_{31_{i,j+1}} - \boldsymbol{I}_{32_{i,j+1}} - \alpha \acute{\boldsymbol{I}}_{31_{i+1,j+1}} - \acute{\boldsymbol{I}}_{32_{i+1,j}} \\
& +\alpha \acute{\boldsymbol{I}}_{31_{i,j+1}} + 2\acute{\boldsymbol{I}}_{32_{i,j}} - \acute{\boldsymbol{I}}_{32_{i,j+1}} - \frac{1}{\alpha}\acute{\boldsymbol{I}}_{38_{i+1,j+1}} + \frac{1}{\alpha}\acute{\boldsymbol{I}}_{38_{i+1,j}}] \\
& +\frac{\Delta t}{2\Delta x_1}[\alpha \boldsymbol{I}_{27_{i,j+1}} + \boldsymbol{I}_{21_{i+1,j}} - \alpha \boldsymbol{I}_{27_{i+1,j+1}} - 2\boldsymbol{I}_{21_{i+1,j+1}} \\
& +\boldsymbol{I}_{21_{i,j}} + \frac{1}{\alpha}\boldsymbol{I}_{22_{i,j}} - \frac{1}{\alpha}\boldsymbol{I}_{22_{i,j+1}} + \alpha \acute{\boldsymbol{I}}_{57_{i+1,j+1}} - 2\acute{\boldsymbol{I}}_{51_{i,j}} \\
& +\frac{1}{\alpha}\acute{\boldsymbol{I}}_{52_{i+1,j+1}} - \frac{1}{\alpha}\acute{\boldsymbol{I}}_{52_{i+1,j}} + \acute{\boldsymbol{I}}_{51_{i+1,j}} - \alpha \acute{\boldsymbol{I}}_{57_{i,j+1}} + \acute{\boldsymbol{I}}_{51_{i,j+1}}] \,.
\end{aligned} \tag{2.94}$$

where the moments $\boldsymbol{I}_{\mathrm{kl}i,j}$ are defined in Appendix A.

Chapter 3

Numerical Results of MKFS Schemes

We consider two elementary two-dimensional flowfields to illustrate the methods discussed here. We consider three kinetic flux-split algorithms: MKFS-CIR, MKFS-NDA and MKFS-LDA. The MKFS-NDA scheme is the multi-dimensional scheme based on the N-scheme and is described in [60]. The MKFS-CIR scheme is a dimensionally-split scheme based on the CIR scheme applied to the Boltzmann equation and is also described in [60]. The MKFS-LDA scheme is the higher-order kinetic scheme described here and in [61].

In the contour plots we used fifteen levels between maximum and minimum values of plotted function.

3.1 Shock Reflection Problem

The shock reflection problem has been used before to test diagonal dependence of the N-scheme based Boltzmann solvers by Eppard and Grossman [60]. It was also used in numerical experiment with the boundary conditions for the Euler solvers by Dadone and Grossman [46]. We consider the 29 degree shock reflection off a flat plate with a Mach 2.9 freestream. The uniformly spaced grid was 2.75 length units long and 1.0 length unit high with 61×33 mesh. The incident oblique shock location was

fixed at a height of 0.75 length units at the inflow from the left. Lower wall was modelled using inviscid wall boundary conditions and the outflow on the right and upper boundaries were served using extrapolation. Density contours are plotted in Figures 3.1 - 3.3 for the MKFS-CIR scheme, MKFS-NDA scheme and the MKFS-LDA scheme respectively. Calculations by CIR and NDA schemes are first-order accurate in space; the LDA scheme is a second-order accurate for smooth solutions on uniform grids.

The results from the CIR scheme have excessive smearing of the shock wave as expected for a first-order dimensionally-split scheme. The NDA scheme produces a very sharp inflow using the down-running diagonal N-scheme for the incident part and reflected shock is captured efficiently by the up-running diagonal N scheme. The adaptive strategy provides resolution for both shocks in half the grid points that are necessary for the CIR solution. The one dimensional boundary conditions on the wall are responsible for the minor increase in the thickness of the the reflected shock. The results for the adaptive, higher order LDA-scheme indicate more accurate spatial resolution over the NDA scheme.

Figure 3.4 shows results for normalized density along the $j = 12$ grid line for the CIR scheme, the multi-dimensional NDA scheme, the multi-dimensional LDA scheme and the exact solution. This plot shows significant improvement for the results of the multi-dimensional NDA and LDA schemes over the results of the dimensionally-split CIR results. The results produced by the multi-dimensional schemes show much sharper shock profiles and agree much better with the exact solution, with the LDA scheme having significantly sharper shock profiles. It may be noted that the results for the LDA-scheme show no evidence of oscillations in the vicinity of the shock waves, which may have been expected, since the scheme is non-positive. The multi-dimensional schemes also capture the peak value of density behind the reflected shock while the CIR scheme slightly under-predicts this value.

The second case is the same Mach 2.9, 29 degree reflected shock, but on a 121×61 mesh. Density contours for this case are shown in Figures 3.5, 3.6 and 3.7 for the MKFS-CIR scheme, the MKFS-NDA scheme and the MKFS-LDA scheme respectively. For the first-order schemes we note that the multi-dimensional NDA scheme

produces highly resolved inflow and reflected shocks that are again much sharper than the corresponding CIR results. Moreover, the multi-dimensional NDA scheme produces results on the 61×33 grid shown in Figure 3.2 that are as good as the CIR results on the 121×61 grid shown in Figure 3.5. As expected, the higher-order LDA scheme produces sharper shocks than the NDA scheme.

3.2 Supersonic Oblique Shear Layer

The next case is a 45 degree shear discontinuity separating Mach 2.9 and Mach 2.4 flows. Calculations are performed on a 33×33 uniform grid with a length and height of 1.0 length unit. Supersonic inflow conditions were used for left and lower boundaries. Supersonic outflow conditions were applied on the right and upper boundaries. Density contours for this case are shown in Figures 3.8, 3.9 and 3.10 for the MKFS-CIR scheme, the MKFS-NDA scheme and the MKFS-LDA scheme, respectively. Again, the multi-dimensional NDA scheme captures the shear wave in approximately half the grid points necessary for the CIR solution. However, the LDA scheme is produces only slightly improved wave resolution over the NDA scheme. This may be seen directly in Figure 3.11, where we plot the Mach number distribution for the three cases versus x along a line at a constant value of y equal to 80% of the height of the domain. We see that both the NDA and LDA schemes produce a steeper jump through the wave than the CIR result and importantly, both the multidimensional schemes accurately predict the Mach number jump across the wave. However, there appears to be only a modest benefit for the LDA scheme over the NDA scheme in the resolution of shear waves.

3.3 Discussion of MKFS Schemes

Presented multi-dimensional kinetic fluctuation-splitting schemes were used to study issues related to the residual distribution schemes for triangle meshes and implementation of them at the Boltzmann level. Results show an advantage of the adaptive strategy when applied to triangulation of the uniform rectangular grid. This type of

the triangulation not only reduces diffusion of the scheme but also serves as a simple alternative to traditional adaptive grid methods. Result for LDA-scheme shows improvement over the N-scheme based solvers. Results for a simple oblique-shock reflection and a shear wave demonstrates that the adaptive procedure and the higher order low diffusion scheme provide sharper resolution then the dimensionally-split kinetic CIR scheme and the first order N-scheme. LDA-scheme for scalar advection equation does not guarantee a monotone profile through the jump. Nevertheless, no evidence of oscillations near discontinuities was observed but the order of accuracy is lower then the second order accuracy theoretically predicted for regular meshes. One possible explanation is that the integration of infinite number of waves on the kinetic level leads to cancellation of minor oscillations in each particular wave pattern, at the same time reducing order of accuracy. If this is correct, it might be interesting to explore possibilities to apply higher order schemes with close to monotone behavior at the kinetic level. In present form, the schemes are too complex and inefficient.

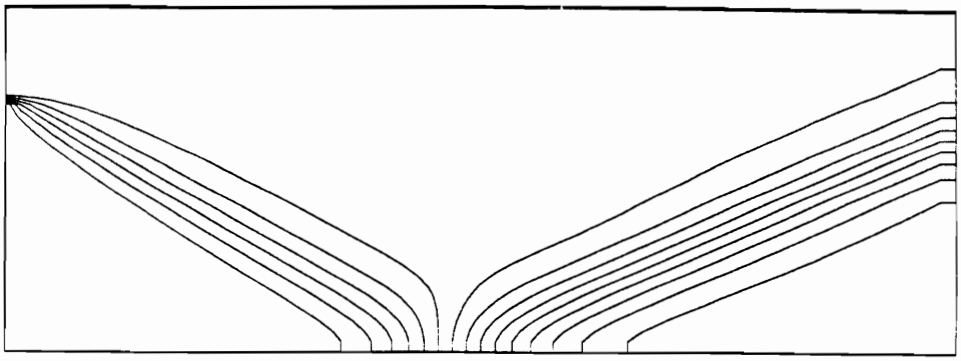

Figure 3.1: Shock reflection: MKFVS-CIR Scheme, 61x33 Grid

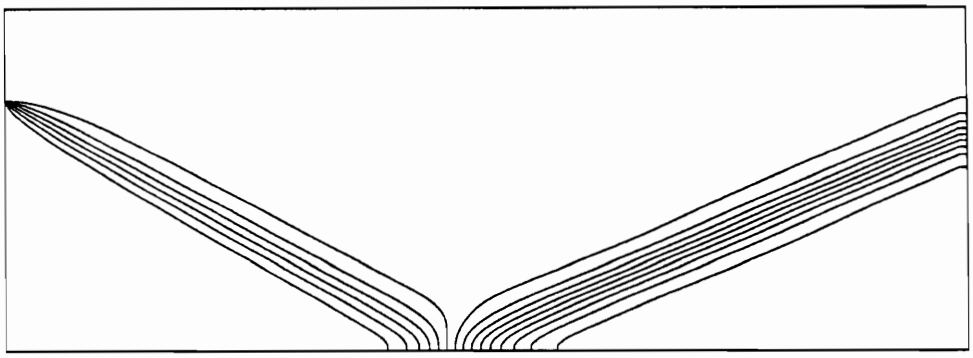

Figure 3.2: Shock reflection: MKFVS-NDA Scheme, 61x33 Grid

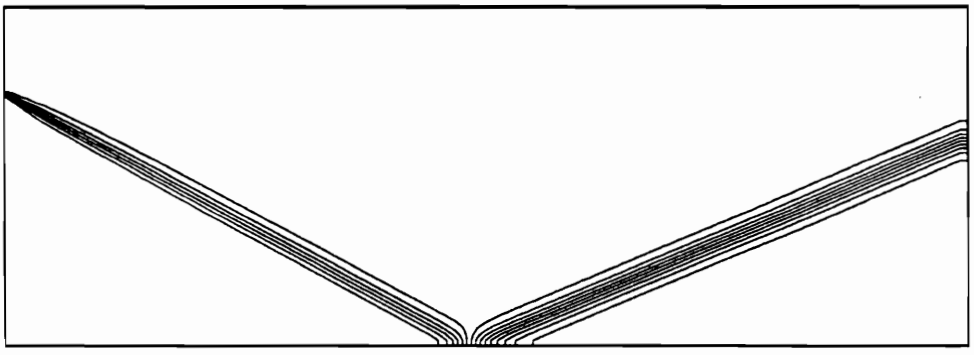

Figure 3.3: Shock reflection: MKFVS-LDA Scheme, 61x33 Grid

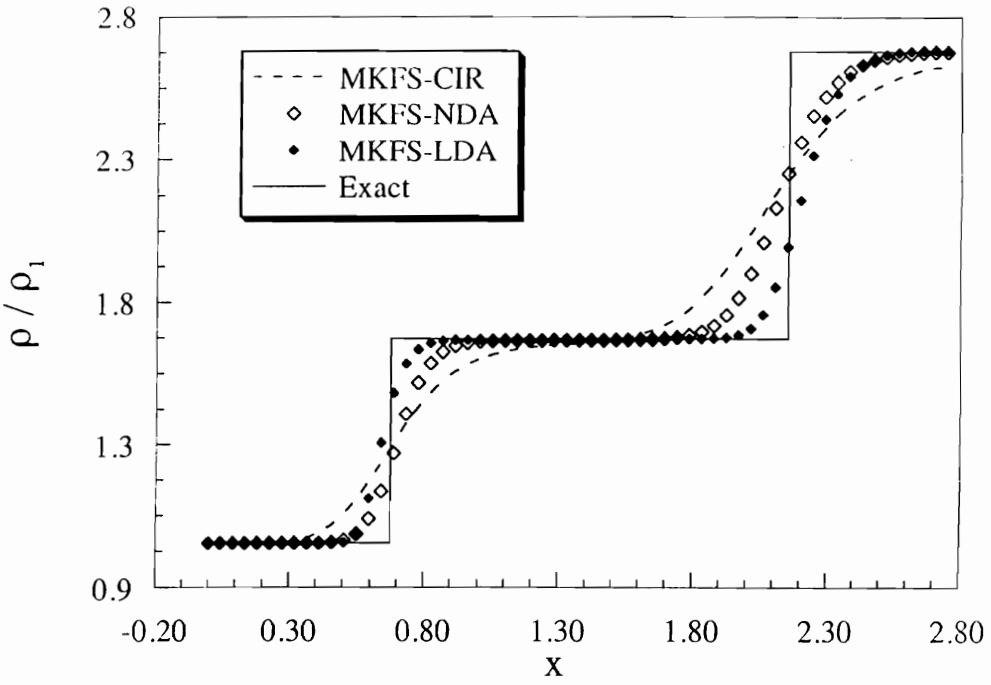

Figure 3.4: Density Distribution, 29^0 Shock Reflection, 61x33 Grid

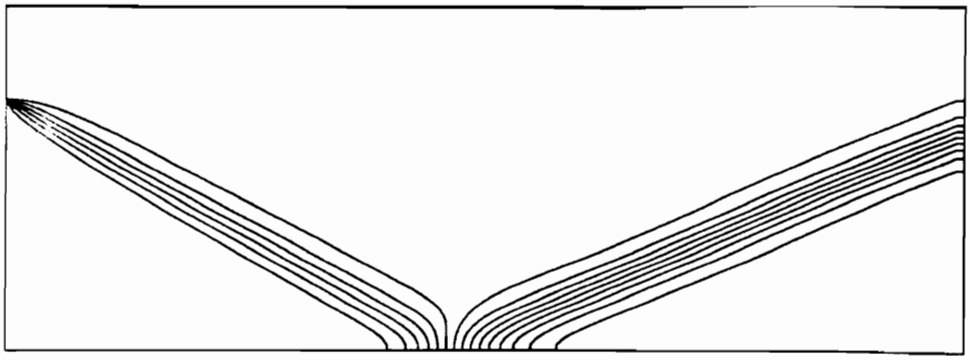

Figure 3.5: Shock reflection: MKFVS-CIR Scheme, 121x61

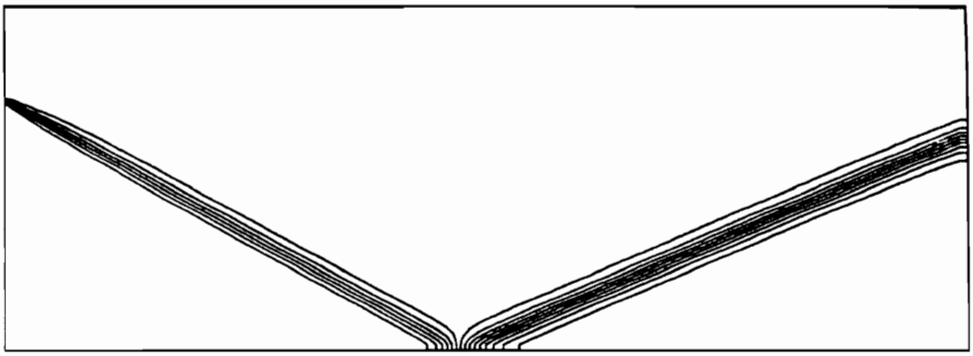

Figure 3.6: Shock reflection: MKFVS-NDA Scheme, 121x61

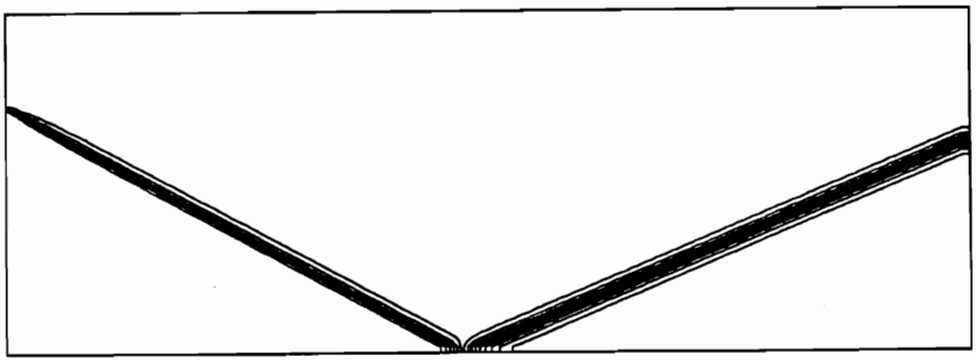

Figure 3.7: Shock reflection: MKFVS-LDA Scheme, 121x61

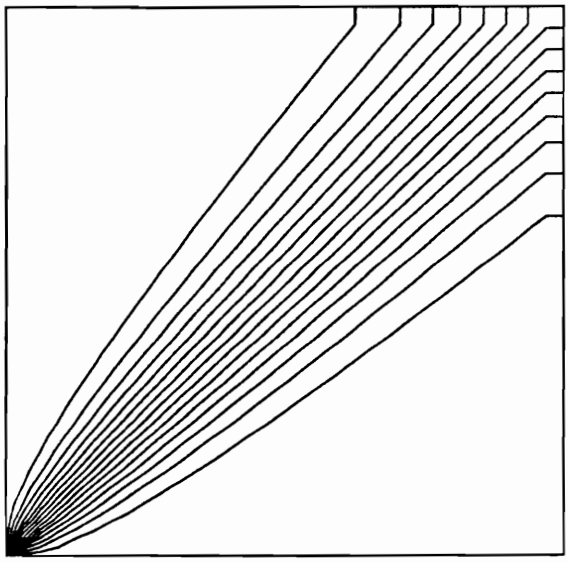

Figure 3.8: Shear Discontinuity: MKFVS-CIR Scheme

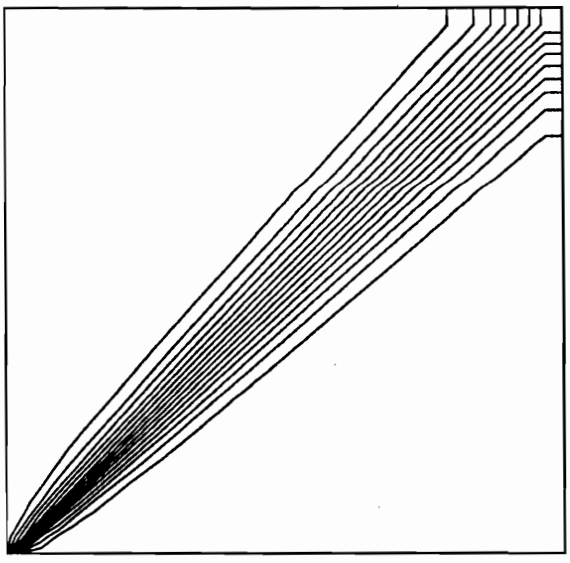

Figure 3.9: Shear Discontinuity: MKFVS-NDA Scheme

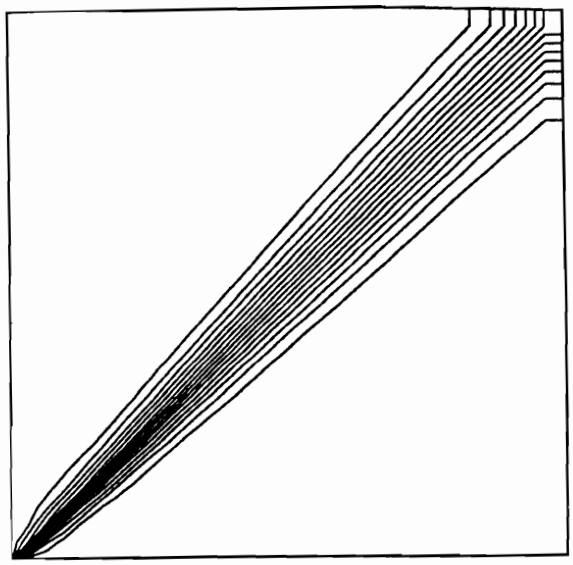

Figure 3.10: Shear Discontinuity: MKFVS-LDA Scheme

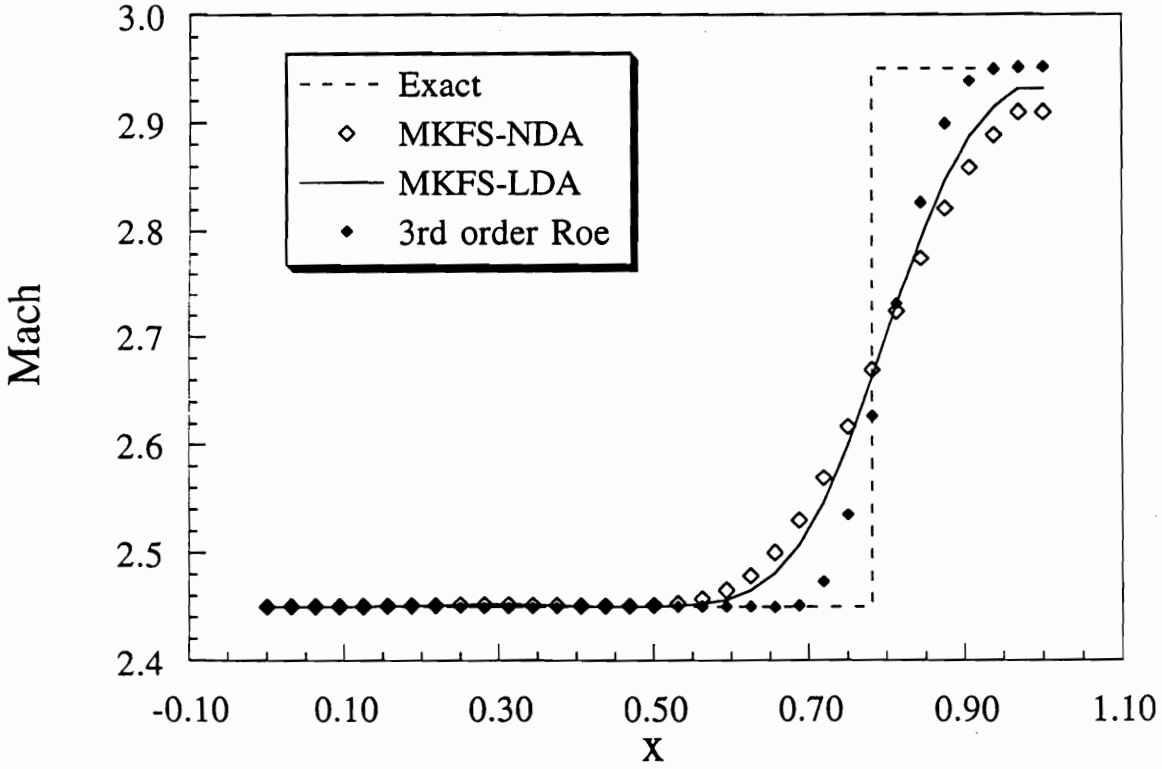

Figure 3.11: Density Distribution, Shear Discontinuity.

Chapter 4

Discontinuity Confinement Technique

4.1 Vortex Confinement Technique for Incompressible Flow

The *vorticity confinement* method was developed by Steinhoff and coworkers [54], [55], [56] for computing flows with concentrated vorticity and was originally applied to incompressible flows. Similar to the shock capturing methods, it treats vortical layers without a detailed resolution of their internal structure. A confinement procedure is constructed in such way that it preserves certain conservation laws outside and integrated over the vortical regions. The method is flexible and easily incorporated with standard Euler/Navier-Stokes methods on a fixed grid. Applied to various problems involving concentrated vorticity, the vorticity confinement approach has been proved to be capable of treating thin vortical structures in complicated flows, even on relatively coarse grids. The core of the method is a velocity correction, applied locally, that prevents vorticity from diffusing during propagation.

Numerical implementation of the vorticity confinement for an incompressible flow includes 3 main steps: convection of velocities based on momentum equations; velocity correction according to the confinement method; solution of the pressure to enforce

mass conservation, as in conventional "split velocity" methods [74]. For convecting vortices, a steady - state structure is reached when diffusion from the convection step and the pressure correction are balanced with the confinement. Details of the method and its numerous application can be found in the collection of the papers ([53], [54], [55], [57], [58], [59]).

Applied to incompressible flows, vorticity confinement has proved to be an efficient method in conjunction with simple first-order monotonic upwind schemes as a basic solver. Nonetheless, attempts to apply the vorticity confinement method directly to compressible flow described by the Euler equations turned out to be not straightforward. A partial explanation of this could be that vorticity confinement acts only on the velocity field and equilibrates numerical dissipation only for the momentum equations. At the same time, the velocity correction term works as an unbalanced source for the continuity and energy equations. Traditional compressible solvers do not include a mass/energy conservation step similar to the one in the "split-velocity" method, used for incompressible problems. As a result, there is no steady state solution for the modified system of equation *e.g.*, the original system plus confinement terms in the momentum equations. For the time-dependent problems this error is practically negligible for the subsonic flow. But, if we expand this approach to the transonic and supersonic problems with the regions with steep gradients and discontinuities, the conservation is the critical requirement. In addition, we will need a more universal type of confinement than just a vorticity confinement.

4.2 Confinement for the Acoustic Pulses

Following the same antidiffusive convection idea as in vorticity confinement, Steinhoff *et al.* [59] have developed a new confinement procedure for acoustic waves. There are several main notions, used in the construction of the method. The flows of interest include flow structures with at least one small dimension that propagates over long distances or period of time. Detailed resolution of this features is not necessary and the main requirement is that the governing laws are obeyed in integral form. The

method is intended to propagate information about that thin flow feature in non-diffusive manner, regardless of its internal structure. A similar "capture without detailed resolution" approach is used for the shock waves in conventional numerical methods. The second idea is to represent the "captured" features in terms of nonlinear "solitary waves". Being an exact solution of the resulting numerical scheme, this representation will propagate without changes and dissipation.

The simplest application of the described technique is the one for the advection of the passive scalar u with velocity c:

$$u_t = -cu_x. \tag{4.1}$$

The upwind discretization for the $c > 0$:

$$u_i^{n+1} = u_i^n - \nu(u_i^n - u_{i-1}^n) + \varepsilon\Delta u \tag{4.2}$$

where for the time step of Δt and the grid size of Δx the Courant number is:

$$\nu = \frac{c\Delta t}{\Delta x.} \tag{4.3}$$

They introduced a "confinement term" $\varepsilon\Delta u$ in their discretization with "confinement parameter" ε. Without this term the original upwind scheme will have second order contributions of the numerical diffusion that could be written using diffusion parameter μ_0:

$$\delta_{diff} \sim \mu_0 \frac{\Delta x^2}{\Delta t} u_{xx} = \frac{\nu(1-\nu)}{2} \frac{\Delta x^2}{\Delta t} u_{xx}. \tag{4.4}$$

The initial pulse will be spread after small number of time steps. The propagating pulse will have stable shape if we add proper amount of antidiffusion convection inward toward the pulse center. The direction of this convection is guided by means of a switch:

$$a_i^n = \frac{\delta_i^C u_i^n}{\bar{u}_i^n}. \tag{4.5}$$

In this chapter we will use the following notations:

$$\delta_i^- f_i = f_i - f_{i-1}, \tag{4.6}$$

$$\delta_i^C f_i = \frac{1}{2}\left(f_{i+1} - f_{i-1}\right), \tag{4.7}$$

$$\bar{f}_i = \frac{1}{2}\left(f_{i+1} + f_{i-1}\right). \tag{4.8}$$

The confinement term now can be written as a convection operator:

$$\Delta u = \delta_i^- \left[a_i^n u_i^n \right] \tag{4.9}$$

or as an artificial viscosity (a negative viscosity that prevents dissipation):

$$\begin{aligned} \Delta u &= \delta_i^- \left[\alpha_i^n \delta_i^C u_i^n \right], \\ \alpha_i^n &= \frac{u_i^n}{\bar{u}_i^n}. \end{aligned} \tag{4.10}$$

The setting of the parameter ε is explained in detail in [59] and the stable solutions are achieved for the wide range $-3.5\mu_0 \leq \varepsilon \leq -\mu_0$.

For practical purposes we need to apply the technique to functions with a general shape. To convert the previous formulation for pulses to the step discontinuities we use the simple relations:

$$\begin{aligned} \omega_i^n &= \sum_{l=0}^{i} u_l^n, \\ u_i^n &= \delta_i^- \omega_i^n. \end{aligned} \tag{4.11}$$

The final equation for the advection of a passive scalar field with discontinuities is now given by

$$\begin{aligned} \omega_i^{n+1} &= \omega_i^n - \nu(\omega_i^n - \omega_{i-1}^n) + \varepsilon \alpha_i^n \delta_i^C \delta_i^- \omega_i^n, \\ \alpha_i^n &= \delta_i^- \omega_i^n / \overline{\delta_i^- \omega_i^n}. \end{aligned} \tag{4.12}$$

Detailed discussion of the method and results for different types of problem with discontinuities could be found in [59].

The next step in a pulse confinement method testing is the extension to the two-dimensional wave equation:

$$\partial_t^2 u = c^2 \nabla^2 u. \tag{4.13}$$

A two stage central difference basic solver plus the confinement term for the scalar wave equation becomes [59]:

$$\begin{aligned} u_{ij}^* &= 2u_{ij}^n - u_{ij}^{n-1} + \sigma^2(\delta_i^2 + \delta_i^2) u_{ij}^n \\ u_{ij}^{n+1} &= u_{ij}^* + \mu_1(\delta_i^2 + \delta_i^2)\delta_n^- u_{ij}^* + \epsilon \Delta u \end{aligned} \tag{4.14}$$

where

$$\delta_n^- u_{ij}^* = u_{ij}^* - u_{ij}^n \tag{4.15}$$

and the confinement convection is written in terms of an upwind difference operator $\tilde{D}(\hat{n}_k)$ in the k direction:

$$\Delta u = \left(\tilde{D}(\hat{n}_1) + \tilde{D}(\hat{n}_2)\right) u_{ij}^*. \tag{4.16}$$

The unit vector $\hat{n} = (\hat{n}_1, \hat{n}_2)$ represents the direction of the antidiffusion confinement and points inside the pulse. Using a discretized of the gradients it can be written as the following

$$\hat{n} = \mathbf{B}\frac{\nabla u^*}{|\nabla u^*|}. \tag{4.17}$$

In order to reduce the confinement along the propagating pulse and, therefore, avoid a Raleigh-Taylor type of instability for the thin flow structure, the stabilizing matrix $\mathbf{B}$ is used:

$$B_{lm} = \frac{\partial_{l,m} u^*}{|\partial_1^2 u^*| + |\partial_2^2 u^*|}, \qquad l, m = 1, 2. \tag{4.18}$$

where the indices 1 and 2 denote i and j derivatives respectively.

The method in this formulation was tested on propagating circular pulses [59] and the efficiency of it for propagation over the long distances was demonstrated. However, the present formulation is not conservative and required additional development and testing for the practical applications.

The rest of this chapter will describe the ideas developed in search for multi-dimensional and conservative procedure to apply confinement to the system of the conservation laws.

4.3 Flux Correction Formulation

4.3.1 Discontinuity Confinement for Hyperbolic Conservation Laws

We consider the numerical solution of the hyperbolic conservation law

$$u_t + f(u)_x = 0 \tag{4.19}$$

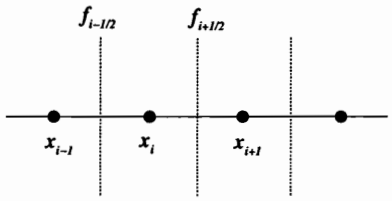

Figure 4.1: One dimensional finite volume notation.

on a mesh defined by fixed and equally spaced nodes $x = x_i$, Figure 4.1. Denote by $f^n_{i+1/2}$, a flux in a monotone finite-volume scheme, presented in conservative form

$$u_i^{n+1} = u_i^n - \frac{\Delta t}{\Delta x}[f^n_{i+1/2} - f^n_{i-1/2}]. \tag{4.20}$$

We define the linearized wave speed at the grid interface as

$$c_{i+1/2} = \frac{\partial f}{\partial u}|_{i+1/2}. \tag{4.21}$$

Accordingly, the local Courant number ν is given by

$$\nu_{i+1/2} = c_{i+1/2} \cdot \frac{\Delta t}{\Delta x}. \tag{4.22}$$

and the practical range for this factor is order one.

The confinement term will preserve the conservative formulation if it could be represented as a difference of flux correction terms at the cell faces. We transform original formulation in Equation (4.13) using linearization for the switch α and definition of the wave speed (4.21):

$$\begin{aligned} \varepsilon \alpha_i^n \delta_i^C \delta_i^- u_i^n = \varepsilon' \nu_i \alpha_i^n \delta_i^{C*} \delta_i^- u_i^n = \\ \varepsilon' c_i \frac{\Delta t}{\Delta x} \alpha_i^n \left(\delta_i^- u^n_{i+1/2} - \delta_i^- u^n_{i-1/2} \right) \approx \\ \varepsilon' \frac{\Delta t}{\Delta x} \left(\alpha^n c \; \delta_i^- u^n_{i+1/2} - \alpha^n c \; \delta_i^- u^n_{i-1/2} \right) = \\ \varepsilon' \frac{\Delta t}{\Delta x} \left(\alpha^n \delta_i^- f^n_{i+1/2} - \alpha^n \delta_i^- f^n_{i-1/2} \right), \end{aligned} \tag{4.23}$$

where the flux differences $\delta_i^- f^n$ are calculated based on the fluxes of the original solver Equation (4.20). We replaced ε by normalized ε' using local Courant number. For

the positive wave speed the first order upwind scheme gives us:

$$\delta_i^- f_{i+1/2}^n = f_{i+1/2}^n - f_{i-1/2}^n = f_i^n - f_{i-1}^n, \tag{4.24}$$

where we used first order upwind fluxes at the interfaces. The switch α is used in the same form (4.13) except for more compact support in the calculation of the average in the denominator:

$$\alpha_{i+1/2} = \frac{2\delta^- u_{i+1}^n}{\delta^- u_{i+1}^n + \delta^- u_i^n + \tau} \tag{4.25}$$

where τ is a small positive number that prevents from dividing by close to zero values at the smooth regions and an excitation of a numerical noise. After the same consideration for the negative wave speed counterpart, the flux correction will be given as:

$$\tilde{f}_{i+1/2}^n = \begin{cases} 2\epsilon[f_{i+1/2}^n - f_{i-1/2}^n]\ \delta^- u_{i+1}/(\delta^- u_{i+1} + \delta^- u_i + \tau) & \text{if } c_{i+1/2} > 0; \\ 2\epsilon[f_{i+1/2}^n - f_{i+3/2}^n]\ \delta^- u_{i+1}/(\delta^- u_{i+1} + \delta^- u_{i+2} + \tau) & \text{if } c_{i+1/2} < 0; \\ 0 & \text{if } c_{i+1/2} = 0. \end{cases} \tag{4.26}$$

The choice of parameters is determined by requirements of stability and monotonicity. The parameter τ serves as a sensitivity parameter as well. For those grid points where $\delta u_i < 10\tau$, no correction is applied to the fluxes. At the same time, according to Von Neumann stability analysis, it would remove components for which the amplification factor would be greater then one. The parameter ϵ is restricted to the range $0 \leq \epsilon \leq 0.7$.Based on numerical experiments, this value is a function of CFL number and ratio $(u_R - u_L)/c_{jump}$, where c_{jump} is the speed of discontinuity. Increases in both reduce the optimum value of ϵ with regard to a stable and monotone scheme with maximum confinement effect.

4.3.2 Discontinuity Confinement for 1-D Euler Equations

The Euler equations consist of a system of non-linear coupled hyperbolic equations. This makes application of the discontinuity confinement method in the flux correction form more complicated, since it is designed for a scalar equation. One method to apply it to a system of hyperbolic equations is to utilize the characteristic form of the system. For the one-dimensional Euler equations the characteristic form is

uniquely determined and the confinement method could be applied by considering each equation separately. This approach requires independent definition of τ_k and ϵ_k where $k = 1, 2, 3$. Further, the linearization that is used to transform the conservative variables and updates to characteristic level induces additional numerical "noise" near the discontinuity which imposes additional limits on τ.

For present calculations we used Roe's approximate Riemann solver [75]. It uses a matrix $\hat{A}$ that satisfies the conservative relation

$$F_{i+1} - F_i = \hat{A}(U_i, U_{i+1})(U_{i+1} - U_i). \tag{4.27}$$

where F_i is the flux vector for conservative variables

$$F_i = \begin{pmatrix} \rho u \\ \rho u^2 + p \\ \rho u H \end{pmatrix}. \tag{4.28}$$

and U_i is a vector of the conservative variables

$$U_i = \begin{pmatrix} \rho \\ \rho u \\ \rho E \end{pmatrix}. \tag{4.29}$$

After calculating the usual Roe-averages for density $\hat{\rho}$, speed $\hat{u}$ and stagnation enthalpy $\hat{H}$, the eigenvalues of the $\hat{A}$ matrix are obtained at the cell faces

$$\hat{\lambda}_{(1)} = \hat{u} \quad \hat{\lambda}_{(2)} = \hat{u} + \hat{c} \quad \hat{\lambda}_{(3)} = \hat{u} - \hat{c} \tag{4.30}$$

where $\hat{c}$ is the associated averaged speed of sound

$$\hat{c}^2 = (\gamma - 1)\left[\hat{H} - \frac{\hat{u}^2}{2}\right]. \tag{4.31}$$

If we denote by δw_k the characteristic wave amplitude

$$\begin{aligned} \delta w_1 &= \delta\rho - \frac{\delta p}{\hat{c}^2} \\ \delta w_2 &= \delta u - \frac{\delta p}{\hat{\rho}\hat{c}} \\ \delta w_3 &= \delta u + \frac{\delta p}{\hat{\rho}\hat{c}} \end{aligned} \tag{4.32}$$

then the fluxes differences on the characteristic level can be calculated as

$$\delta F_k^w|_i = F_k^w|_{i+1/2} - F_k^w|_{i-1/2} = (\hat{\lambda}^-_{(k)}\delta w_k)|_{i+1/2} + (\hat{\lambda}^+_{(k)}\delta w_k)|_{i-1/2} \tag{4.33}$$

where the $\pm$ superscript on the eigenvalues represents positive and negative values, respectively. Now the flux corrections for the characteristic wave equations are calculated according to Equation (4.26):

$$\tilde{F}^w_{i+1/2} = \begin{cases} 2\varepsilon\,(\delta F_k^w)\,|_i\ \delta^- w_{i+1}/(\delta^- w_{i+1} + \delta^- w_i + \tau) & \text{if } \hat{\lambda}_{(k)}\,|_{i+1/2} > 0; \\ -2\varepsilon\,(\delta F_k^w)\,|_{i+1}\ \delta^- w_{i+1}/(\delta^- w_{i+1} + \delta^- w_{i+2} + \tau) & \text{if } \hat{\lambda}_{(k)}\,|_{i+1/2} < 0; \\ 0 & \text{if } \hat{\lambda}_{(k)}\,|_{i+1/2} = 0. \end{cases} \tag{4.34}$$

The last step is to convert corrections to the conservative variable level

$$\tilde{F}_{i+1/2} = \hat{P}\tilde{F}^w_{i+1/2}, \tag{4.35}$$

and add them to the original Roe fluxes

$$U_i^{n+1} = U_i^n - \frac{\Delta t}{\Delta x}[F^n_{i+1/2} + \tilde{F}^n_{i+1/2} - F^n_{i-1/2} - \tilde{F}^n_{i-1/2}]. \tag{4.36}$$

The transformation matrix $\hat{P}$ is calculated at the cell face using Roe's averages

$$\hat{P} = \begin{pmatrix} 1 & \hat{\rho}/2\hat{c} & \hat{\rho} \\ \hat{u} & \hat{\rho}(\hat{u}+\hat{c})/2\hat{c} & -\hat{\rho}(\hat{u}-\hat{c})/2\hat{c} \\ \hat{u}^2/2 & \hat{\rho}(\frac{\hat{u}^2}{2} + \hat{u}\hat{c} + \frac{\hat{c}^2}{\gamma-1})/2\hat{c} & -\hat{\rho}(\frac{\hat{u}^2}{2} - \hat{u}\hat{c} + \frac{\hat{c}^2}{\gamma-1})/2\hat{c} \end{pmatrix}. \tag{4.37}$$

The parameters ε and τ have to be specified for each characteristic variables. Some simple scaling for τ based on the accuracy and the free stream values is possible. At the same time, to set ε to the optimum value requires some additional numerical experiments. A main problem for the multidimensional extension of the scheme is that flux-correction form depends on the grid interfaces and the characteristic decomposition is not truly multidimensional. Dimensionally-split usage did not demonstrate any serious improvement in the solution for test problems.

4.4 Fluctuation Correction Formulation

The second phase in our research was multi-dimensional implementation of the discontinuity confinement idea. At the same time we would like to have a simple conservative procedure to realize it. Instead of extending flux-correction approach we use

original fluctuation correction formulation as it was designed for the wave equation. We modify it to make sure all conservation laws are obeyed.

The conservation procedure was tested first for the one dimensional solver. We used Roe's solver and central difference scheme with a Jameson type artificial dissipation as basic solvers for this calculations.

4.4.1 Antidiffusion Convection

To control conservation for the Euler equations we use this time the conservative variables for the antidiffusive convection. First we calculate update according to the basic solver. We will denote the result of it as U^* instead of U^{n+1}. Now we compute a confinement fluctuation. For each component of the vector of the conservative variables Equation (4.29) we compute its own convection with its own speed:

$$\Phi_{(k)\ i} = W_i \cdot V_{(k)\ i} \cdot \delta_i^C u^*_{(k)} \tag{4.38}$$

where the speed of convection $V_{(k)\ i}$ is calculated as

$$V_{(k)\ i} = 2\frac{\left(\delta^C_{i+1}u^*_{(k)}\right)^2 - \left(\delta^C_{i-1}u^*_{(k)}\right)^2}{\left(\delta^C_{i+1}u^*_{(k)}\right)^2 + \left(\delta^C_{i-1}u^*_{(k)}\right)^2 + \tau_{(k)}}. \tag{4.39}$$

The typical discontinuity profile and corresponding direction of the vector $V_{(k)\ i}$ are shown on Figure 4.2. The function W_i eliminates confinement in a smooth regions based on the cut off value for the gradients and in expansions regions where the confinement could produce nonphysical expansion shocks. This function is zero if a local gradient of the conservative variable is less than a preset small value. It is also vanishes in a region where the following is true:

$$\frac{\partial \rho u}{\partial \rho} \cdot u < 0, \tag{4.40}$$

that we will call an expansion switch. For the one-dimensional case it is based on the propagation of the characteristics. For two and more dimensions the recognition of the expansion regions is not a trivial task.

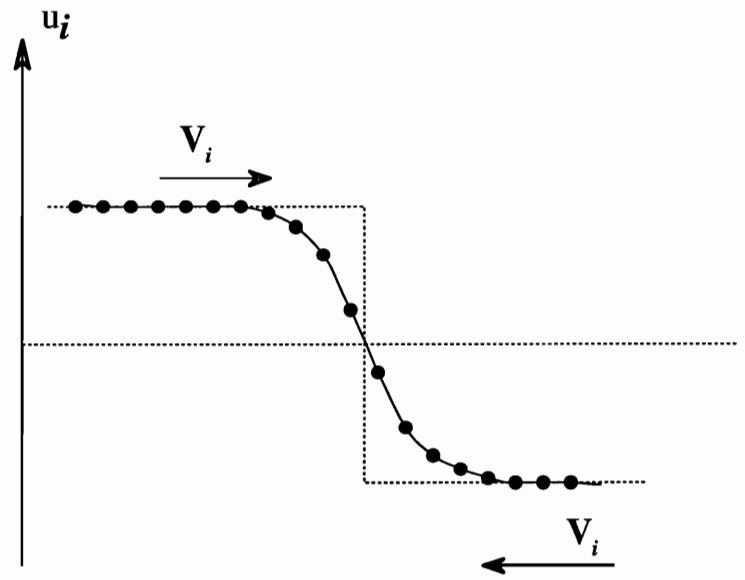

Figure 4.2: Direction of the antidiffusion convection.

4.4.2 Conservation Procedure

The fluctuation $\Phi_{(k)i}$ calculated in previous section is not conservative by design and integration over the whole computational domain is different from zero. We would like to construct a simple procedure that will preserve the conservation laws in an integral sense. Since the action of the confinement procedure is limited to the regions with steep gradients and discontinuities we can use this knowledge to remove nonconservative contributions from the fluctuation. The idea is illustrated in the Figures 4.3-4.5. A typical distribution of the confinement term is shown at Figure 4.3 and the local sum of the correction is small but not a negligible value. If we recall that the main idea is to capture, not to resolve the inner structure of the discontinuity, we can conclude that any reasonably simple way to subtract this contribution from the original fluctuation distribution will lead to conservative correction in integral sense. On two sides of the discontinuity we have fluctuations of the opposite sign. If we now convect these values toward the discontinuity they will partially cancel each other. If we perform conservative smoothing of the resulting function after each "cancellation" iteration, we will obtain a smooth function, localized near discontinuity and with an amplitude much smaller then original fluctuation distribution, see Figure

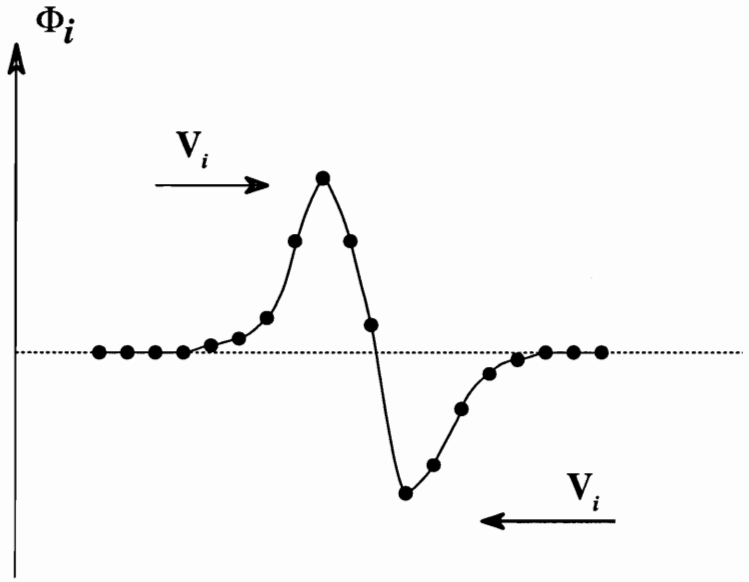

Figure 4.3: Fluctuation profile across discontinuity.

4.4. Subtraction of this calculated field of nonconservative contribution $\Phi^{nc}_{(k)\ i}$ from original field $\Phi_{(k)\ i}$ will not deteriorate the confinement properties of the correction. At the same time the resulting field $\Phi^{c}_{(k)\ i}$ will be strictly conservative.

For the one dimensional case we used a simple shifting procedure to "convect and cancel". According to the sign of the vector $V_{(k)\ i}$ the complete fluctuation is passed to the left of the right cell as shown in Figure 4.5:

$$\begin{aligned} \Phi^{*}_{(k)\ i+1} &= \Phi^{*}_{(k)\ i+1} + \Phi_{(k)\ i}, \quad if\ V_{(k)\ i} > 0 \\ \Phi^{*}_{(k)\ i-1} &= \Phi^{*}_{(k)\ i-1} + \Phi_{(k)\ i}, \quad if\ V_{(k)\ i} < 0 \\ \Phi^{*}_{(k)\ i} &= \Phi^{*}_{(k)\ i} + \Phi_{(k)\ i}, \quad if\ V_{(k)\ i} \neq 0. \end{aligned} \tag{4.41}$$

The solid line outines the original distribution and the gray regions are the profiles after we shifted them in appropriate directions. Then we apply a simple three point averaging among adjacent cells:

$$\Phi^{**}_{(k)\ i} = \frac{1}{4}\Phi^{*}_{(k)\ i+1} + \frac{1}{2}\Phi^{*}_{(k)\ i} + \frac{1}{4}\Phi^{*}_{(k)\ i} \tag{4.42}$$

and we repeat this process several times. This procedure results in a smooth function

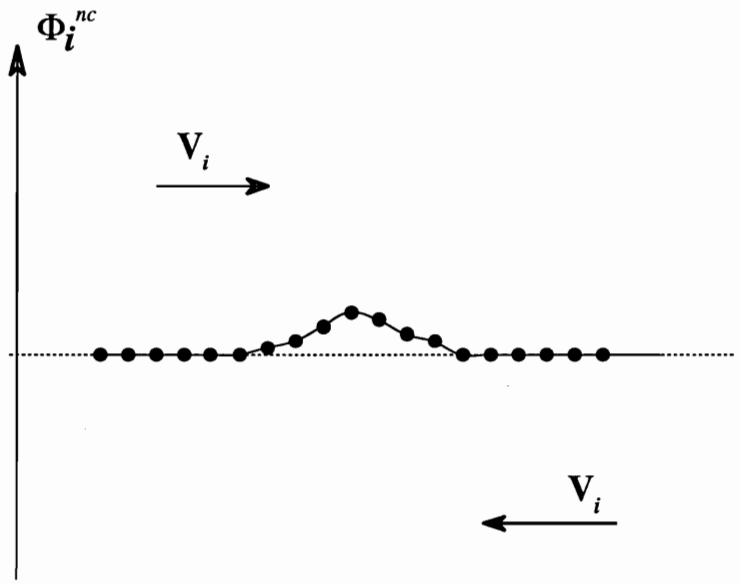

Figure 4.4: Nonconservative component.

$\Phi^{nc}_{(k)\ i}$. The last step will be simple subtraction

$$\Phi^{c}_{(k)\ i} = \Phi_{(k)\ i} - \Phi^{nc}_{(k)\ i} \tag{4.43}$$

and the final update of the conservative variables

$$U^{n+1} = U^{*} - \varepsilon \cdot \Phi^{c}_{(k)\ i}. \tag{4.44}$$

4.5 Multi-Dimensional Confinement Scheme

For the multi-dimensional confinement procedure we used a cell-vertex representation. The solution is stored at the vertices of the mesh. Rectangular grid cells are assumed and for simplicity we considered a uniform grid. This set up implies that after we calculate the confinement term for the grid cell, the fluctuation has to be distributed among the vertices.

The basic solver for the application is a complex issue by itself. The confinement procedure, even with carefully adjusted cut off values and eliminated in the expansion

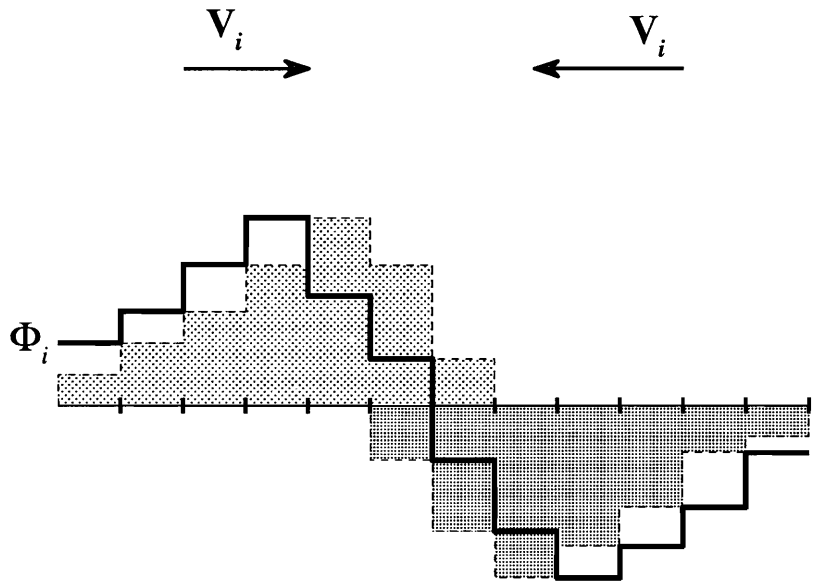

Figure 4.5: Shifting of the fluctuation along the convection vector.

regions, will not damp minor oscillations generated by the basic solver but will rather amplify them and generate problems with convergence and stability. In the case of a solver that uses linearization or approximation to the governing equations to calculate fluxes at the interface, additional problems will arise in the presence of the contact discontinuities. The pressure which is continuous across those feature according to an exact solution will have non-monotone profile for approximate solvers. The order of disturbances is related to the order of the linearization. In the case of confinement, if it is made sensitive to the pressure gradients, the amplitude of this numerical noise will grow without control.

The central difference solvers we used in presented calculations are simple by design and we have control over numerical dissipation that is added explicitly through the use of the artificial dissipation. Moreover, we do not have to deal with the issues of multi-dimensional upwinding or the complex high-order schemes with an involved logic. The central difference solvers will not eliminate the problems related to the approximation and linearization but for the test purposes they proved to be a good starting point.

4.5.1 Basic Solver

We begin with the Euler equations written in divergence form as

$$\frac{\partial Q}{\partial t} + \frac{\partial f}{\partial x} + \frac{\partial g}{\partial x} = 0 \tag{4.45}$$

where

$$Q = (\rho, \rho u, \rho v, \rho E)^t \tag{4.46}$$

represents the vector of dependent conservative variables, ρ is the density, u and v are the components of the velocity vector, p is the pressure and E is the specific total energy. For an ideal gas

$$p = (\gamma - 1)\rho[E - (u^2 + v^2)/2]. \tag{4.47}$$

Flux vectors f and g are given by

$$f = \left(\rho u, \rho u^2 + p, \rho uv, (\rho E + p)u\right)^t \tag{4.48}$$

and

$$g = \left(\rho v, \rho uv, \rho v^2 + p, (\rho E + p)v\right)^t. \tag{4.49}$$

The independent variables are the time t and Cartesian coordinates (x, y). The following analysis will be performed using uniform rectangular coordinates. We will transform the original complex physical domain to a computational domain. After transformation to arbitrary curvilinear coordinates $\xi = \xi(x, y)$ and $\eta = \eta(x, y)$ we obtain

$$\frac{\partial}{\partial t}\left(J^{-1}Q\right) + \frac{\partial F}{\partial \xi} + \frac{\partial G}{\partial \eta} = 0, \tag{4.50}$$

where J^{-1} is the inverse transformation Jacobian, and

$$F = f\frac{\partial y}{\partial \eta} - g\frac{\partial x}{\partial \eta}, \; G = f\frac{\partial y}{\partial \xi} - g\frac{\partial x}{\partial \xi}. \tag{4.51}$$

Time integration is performed with a four-stage Runge-Kutta time-stepping procedure[11]. The basic scheme utilizes a central-difference scheme that is second-order

accurate for sufficiently smooth mesh distributions and has an added artificial viscosity to eliminate unstable modes and improve the convergence rate. We denote spatial difference operators as D_ξ and D_η, where

$$\begin{aligned} D_\xi F_{i,j} &= F_{i+1/2,j} - F_{i-1/2,j} \\ D_\eta G_{i,j} &= G_{i,j+1/2} - G_{i,j-1/2} \end{aligned} \tag{4.52}$$

and the fluxes are approximated as

$$\begin{aligned} F_{i+1/2,j} &= \frac{1}{2}(F_{i+1,j} + F_{i,j}) \\ G_{i,j+1/2} &= \frac{1}{2}(G_{i,j+1} + G_{i,j}). \end{aligned} \tag{4.53}$$

The discretized system is given by

$$Q^k_{i,j} = Q^0_{i,j} - \alpha_k \frac{\Delta t}{J^{-1}_{i,j}} [D_\xi F_{i,j} + D_\eta G_{i,j} - AD_{i,j}]^{k-1}. \tag{4.54}$$

The dissipation term AD is a combination of second and fourth order differences

$$AD_{i,j} = (D^2_\xi + D^2_\eta - D^4_\xi - D^4_\eta) Q_{i,j} \ , \tag{4.55}$$

where

$$\begin{aligned} D^2_\xi Q_{i,j} &= \nabla_\xi \left[\left(\lambda_{i+1/2,j} \epsilon^{(2)}_{i+1/2,j} \right) \Delta_\xi \right] Q_{i,j} \\ D^4_\xi Q_{i,j} &= \nabla_\xi \left[\left(\lambda_{i+1/2,j} \epsilon^{(4)}_{i+1/2,j} \right) \Delta_\xi \nabla_\xi \Delta_\xi \right] Q_{i,j} \end{aligned} \tag{4.56}$$

The variable scaling factor λ was chosen as an average of the spectral radii

$$\lambda_{i+1/2,j} = \frac{1}{2}[(\lambda_\xi)_{i,j} + (\lambda_\xi)_{i+1,j} + (\lambda_\eta)_{i,j} + (\lambda_\eta)_{i+1,j}]. \tag{4.57}$$

The largest eigenvalues of the system λ_ξ and λ_η are given by

$$\begin{aligned} \lambda_\xi &= |u y_\eta - v x_\eta| + c\sqrt{x^2_\eta + y^2_\eta}, \\ \lambda_\eta &= |v x_\xi - u y_\xi| + c\sqrt{x^2_\xi + y^2_\xi}, \end{aligned} \tag{4.58}$$

where c is the speed of sound. In order to control the damping of high-frequency modes and to preserve the second-order accuracy of the scheme in smooth regions,

the coefficients $\epsilon^{(2)}$ and $\epsilon^{(4)}$ are related to local gradients of pressure and temperature. First we calculate $\epsilon^{(2)}$ which is of order one in the neighborhood of shocks and small in the smooth portions of the flowfield:

$$\epsilon^{(2)}_{i+1/2,j} = k^{(2)} max(\nu_{i-1,j}, \nu_{i,j}), \tag{4.59}$$

$$\nu_{i,j} = \frac{1}{\sqrt{x_\xi^2 + y_\xi^2}} max\left(\left|\frac{p_{i+1,j} - 2p_{i,j} + p_{i-1,j}}{p_{i+1,j} + 2p_{i,j} + p_{i-1,j}}\right|, \left|\frac{T_{i+1,j} - 2T_{i,j} + T_{i-1,j}}{T_{i+1,j} + 2T_{i,j} + T_{i-1,j}}\right|\right). \tag{4.60}$$

The fourth order term is switched off near the shocks where it would cause oscillations:

$$\epsilon^{(4)}_{i+1/2,j} = max\left[0, \left(k^{(4)} - \epsilon^{(2)}_{i+1/2,j}\right)\right]. \tag{4.61}$$

The value of $k^{(2)}$ and $k^{(4)}$ has to be specified. In the presented tests $k^{(2)}$ was set to 0.5 and $k^{(4)}$ to 0.01 .

4.5.2 Confinement Procedure

The present version of the discontinuity confinement technique includes three main parts: (a) calculation of the update for each grid cell; (b) elimination of nonconservative components; (c) distribution of the update among grid vertices. The core of the procedure is the convection of the conservative variables towards the discontinuity. The antidiffusion convection is based on the physics of the flow, instead of calculating separate convective directions for each variables we choose a *control variable* — $\rho|V|$ where $|V|$ is an absolute value of the local speed. All conservative variables are convected according to the gradients of this variable. The choice of a *control variable* has to be relevant to the feature of the flow to be resolved and in present form it can detect both contact discontinuities and slip lines. An additional change has to be made to the selection process that excludes expansion regions from influence of the confinement procedure. To identify the contact discontinuities we compare the magnitude of the gradients of the control variable and pressure at each grid cell. If the control variable has gradients of an order of magnitude (using local grid cell size $\sqrt{S_{i,j}}$) higher than pressure gradients, we calculate the confinement fluctuation at that grid cell. This switch is used for contact surfaces, for shock regions a more general shock/contact detecting switch has to be incorporated.

In the present code, the confinement is applied in the regions where the following is true:

$$\frac{|\nabla q^c|}{q^c_\infty} \Big/ \frac{|\nabla p|}{\rho_\infty V^2_\infty} \geq 0.9 \frac{1}{\sqrt{S_{i,j}}}, \tag{4.62}$$

where q^c is the control variable and $S_{i,j}$ is the cell area. If this is not the case, we either do not use the confinement or we use it with a reduced factor $\epsilon^{exp} = \epsilon^c \cdot \sqrt{S_{i,j}}$.

The confinement fluctuation for each grid cell is given by:

$$\mathbf{\Phi} = \epsilon^c \left(\hat{n}' \cdot \nabla Q\right) = \epsilon^c \left(n'_x \frac{\partial Q}{\partial x} + n'_y \frac{\partial Q}{\partial y} \right), \tag{4.63}$$

where factor ϵ^c will be determined by the switch we mentioned above and vector $\hat{n}'$ points toward the discontinuity,

$$\hat{n}' = \hat{n}^* \cdot \frac{|\hat{n}^c|}{|\hat{n}^*|} \tag{4.64}$$

$$\hat{n}^* = \mathbf{B} \cdot (\mathbf{B} \cdot \hat{n}^c) \tag{4.65}$$

$$\mathbf{B} = \begin{pmatrix} |\nabla q^c|_{xx} & |\nabla q^c|_{xy} \\ |\nabla q^c|_{yx} & |\nabla q^c|_{yy} \end{pmatrix} \tag{4.66}$$

$$\hat{n}^c = \begin{pmatrix} n^c_x \\ n^c_y \end{pmatrix} = \sqrt{S_{i,j}} \cdot \begin{pmatrix} \frac{\partial}{\partial x} |\nabla q^c| / \left(\overline{|\nabla q^c|} + \tau \right) \\ \frac{\partial}{\partial y} |\nabla q^c| / \left(\overline{|\nabla q^c|} + \tau \right) \end{pmatrix}. \tag{4.67}$$

Parameter τ prevents vanishing of the denominator for constant regions. All derivatives are of the box-scheme-type:

$$\begin{aligned} \frac{\partial Q}{\partial x}\Big|^{box}_{i,j} &= \frac{1}{2\Delta x} \cdot (Q^3_{i,j} - Q^1_{i,j} + Q^4_{i,j} - Q^2_{i,j}) \\ \frac{\partial Q}{\partial y}\Big|^{box}_{i,j} &= \frac{1}{2\Delta y} \cdot (Q^4_{i,j} - Q^3_{i,j} + Q^2_{i,j} - Q^1_{i,j}). \end{aligned} \tag{4.68}$$

We store $Q_{i,j}$ at cell vertices, as shown in Figure 4.6. For each grid cell we calculate the area $S_{i,j}$, the derivatives of the conservative variables $\left(\frac{\partial Q}{\partial x}\right)_{i,j}$ and $\left(\frac{\partial Q}{\partial y}\right)_{i,j}$, the control variable derivatives $\left(\frac{\partial q^c}{\partial x}\right)_{i,j}$ and $\left(\frac{\partial q^c}{\partial y}\right)_{i,j}$, and the magnitude of its gradient $|\nabla q^c|_{i,j}$. The two dimensional equivalent of (4.13) and (4.39) includes the gradients of the control variable and its derivatives (4.67) . A weak Raleigh-Taylor instability

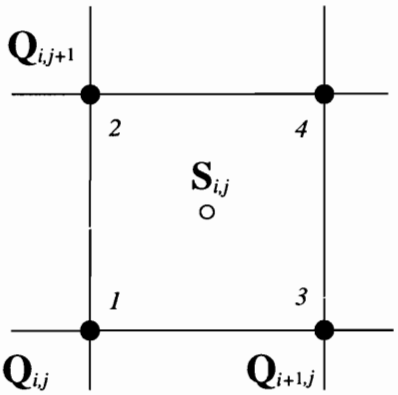

Figure 4.6: Two dimensional grid cell.

develops if original form of $\hat{n}^c$ is used. This problem is solved in the same manner as for the pulse confinement by using a $\mathbf{B}$ matrix that reduces the influence of the gradients tangent to the discontinuities. That is we reduce tangential components in the $\hat{n}^c$ vector by multiplication with the matrix of second order derivatives (4.65), (4.66) . There is an option of using a unit vector $\hat{n}^*/|\hat{n}^*|$ or preserving an original length of the vector $\hat{n}^c$ after multiplication by the matrix (4.64). Note that the calculation of the fluctuation for each cell includes the computational molecule of of 4 by 4 grid cells and that at the boundary we will either not use any confinement correction or the vector will be extrapolated using the values of the inside gradients and the boundary conditions. An additional issue is the switch that detects shock regions and if we have two features such as a nonconfined shock and a confined slip line intersecting or originating from the same source then the confined region of the slip line will "pull" the shock region inside. That will not occur if the shock region is identified and confined, so there will be a balance between the numerical confinement of the two discontinuities. At the present point, there are no numerically inexpensive, multi-dimensional detectors of shock/contacts available and several detectors used in different grid adaptation procedures are based on one dimensional decompositions.

The sum of fluctuations over all grid cells is not zero in general; which is equivalent to a nonconservative update. Fortunately, the fluctuations are proportional to local gradients and limited only to the region of steep gradients, and we can use the same approach as for the one-dimensional case. If we convect $\mathbf{\Phi}$ along vector $\hat{n}'$ and smooth

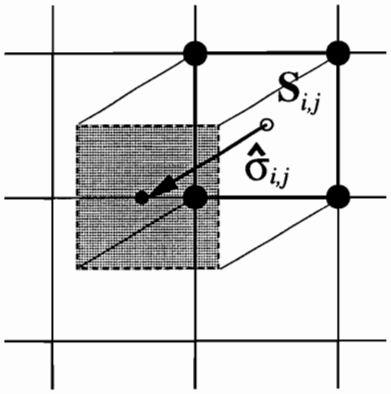

Figure 4.7: Control volume in a shifting procedure.

the resulting function after each iteration, we will have, after several iterations, a new field $\mathbf{\Phi}^{nc}$ that has the same sum, but the local value will be much smaller than $\mathbf{\Phi}$. The difference

$$\mathbf{\Phi}^{*}_{i,j} = \mathbf{\Phi}_{i,j} - \mathbf{\Phi}^{nc}_{i,j} \tag{4.69}$$

is strictly conservative and can be distributed among grid points.

The suggested convection of $\mathbf{\Phi}_{i,j}$ is accomplished by means of simple shifting procedure. First, we find the maximum value of $\hat{n}'$ vector, called $max|\hat{n}'|$ and scale all local vectors $(\hat{n}')_{i,j}$, as:

$$\hat{\sigma}_{i,j} = \hat{n}'_{i,j,} \cdot \sqrt{\frac{|n'_{i,j,}|}{max|\hat{n}'|}}. \tag{4.70}$$

For the boundary cell we have to modify this vector to prevent the correction from "spilling out" of the computational domain. All convection vectors onto the boundary are projected on the boundary so convection is directed in a tangent direction and there is no outward or inward convection of the conservative variables. Each grid cell is considered as a control volume and we assume that the fluctuation is uniformly distributed over that control volume. Now we shift this control volume according to vector $\hat{\sigma}_{i,j}$. Since this vector is less then one grid cell long, in its new location the control volume will overlap with four grid cells, including the original one, as shown on Figure 4.7. Now the portions of fluctuation are distributed to the corresponding grid cells. Since we assumed uniform distribution inside the control volume we distribute the fluctuation in proportion the areas of the control volume that overlap with each

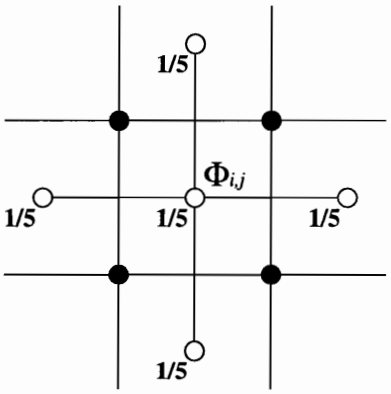

Figure 4.8: Five point stencil for the averaging procedure.

grid cell. This procedure is performed over the whole domain. After each iteration we smooth the resulting distribution, using a five point average, as in Figure 4.8:

$$\Phi_{i,j}^{smooth} = \frac{1}{5} \cdot (\Phi_{i,j} + \Phi_{i+1,j} + \Phi_{i,j+1} + \Phi_{i-1,j} + \Phi_{i,j-1}). \tag{4.71}$$

Several iterations (less then 10) will provide the smooth function that after subtraction will not destroy the effect of confinement but enforce exact conservation.

The last step is to distribute the conservative fluctuations to the grid points. As a result of previous calculation we know the fluctuations and the gradients for the control variable and the conservative variables for each grid cell. The mean gradient $\overline{|\nabla q^c|}$ is computed by averaging gradients in the vertices of the cell, as in Figure 4.9:

$$\overline{|\nabla q^c|}_{i,j} = \frac{1}{4} \cdot (|\nabla q^c|^{(1)} + |\nabla q^c|^{(2)} + |\nabla q^c|^{(3)} + |\nabla q^c|^{(4)}) \mid_{i,j} . \tag{4.72}$$

Those vertex gradients in their turn are calculated by averaging gradients from four adjacent grid cells where we used box-type derivatives. Now we compare vertex gradients with the mean gradient; so, the higher gradient at the node, the bigger the distribution weight:

$$\alpha^l = max(0, |\nabla q^c| - \overline{|\nabla q^c|}), \tag{4.73}$$

$$\alpha_\Sigma = \sum_{l=1}^{4} \alpha^l, \quad \beta^l = \frac{\alpha^l}{\alpha_\Sigma}, \tag{4.74}$$

where α^l is the weight of the vertex in the cell Figure 4.8 and β^l is the portion of the fluctuation sent to the corresponding vertex of the cell.

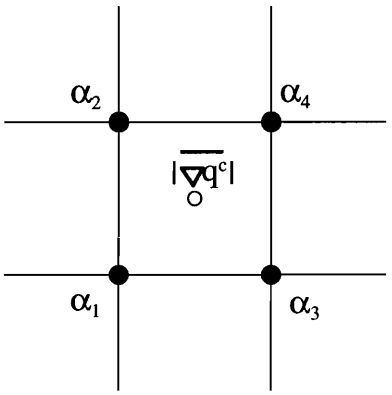

Figure 4.9: Distribution scheme for local fluctuation.

The global update is obtained by summing the contribution from all grid cells K meeting at vertex (i, j)

$$Q_{i,j} = Q_{i,j} - \mu_1 \sum_K \Phi_K^* \beta_K^l \tag{4.75}$$

where μ_1 is an analog of the constant used for Laplace-type dissipation in the pulse confinement procedures [59]. We used $\mu_1 = 0.04$ in all calculations, the same factor is used for the first order central difference scheme solver.

Chapter 5

Numerical Results of Discontinuity Confinement

We used the two-dimensional problems to test different basic solvers with confinement. A first order accurate central difference scheme is based on Laplace-type dissipation. Second order schemes are central difference schemes with scalar dissipation and matrix dissipation. Time integration is the four step Runge-Kutta procedure. Confinement is introduced as a separate stage at each time step.

5.1 Shock Reflection Problem

The shock reflection problem is the same that we used for the kinetic-based scheme. The only difference is that we use square cells so the mesh contains 56 nodes along the x axis and 21 along the y axes. As a result the grid is coarser than 56 by 33 traditionally used in presentations. Mach number contours are shown in Figures 5.1 - 5.6. It can be seen in Figure 5.1 that the first order accurate solution is smeared substantially. After we applied confinement to the first order solver a sharp monotone resolution over 6 grid points developed as can be seen in Figure 5.2 for contours and Figure 5.7 for density profiles. Second order accurate solution with the scalar dissipation is much sharper but as expected is not monotone for steep gradients, see Figure 5.3. Confinement procedure improves resolution and reduces the amplitude of

oscillations near an oblique shock as can be seen in Figure 5.7. Matrix dissipation computations demonstrate behavior similar to scalar dissipation, except that there is minor improvement in terms of oscillations, Figure 5.5 and confined profile is slightly better resolved then for scalar counterpart, see Figure 5.8.

5.2 Supersonic Shear Flow

The case of a long supersonic oblique shear layer demonstrates the important property of the multi-dimensional discontinuity confinement technique. It has to eliminate any sign of dissipation for the shear layer as it propagates over long space distance. We compare this to the results of the high-order flux-difference splitting scheme. A mesh of 330 by 330 square grid cells was used in this calculation. The upper region represents the flow with 2.9 Mach number and the lower region of the flow is at 2.4 Mach number. The numerical domain was initialized with the condition at the upper inflow region. Simple supersonic outflow boundary conditions of first order were used. Mach number contours for an oblique shear layer problem are depicted in Figure 5.9 for the high-order Roe scheme with Van Albada limiter. The same problem solved by central difference solver with the confinement procedure is shown in Figure 5.10. There is a clear sign of slow dissipation by the high order upwind scheme. Notice the highlighted squares which we denote initial and final locations. Magnified images of those regions are compared in Figures 5.11 – 5.14.

At the initial quadrants it can be seen that the confined shear layer developed its 3-4 grid cells resolution and did not change afterwords (see Figure 5.12). The upwind solver does not possess any stable profile and slowly smears out the shear layer, as shown in Figure 5.11. At the final location, the confined profile has the same sharp resolution as at the beginning (see Figure 5.14). The upwind solution spreads to at least twice as much as seen in Figure 5.11. Finally, the Mach number profiles normal to the shear layer demonstrate that the confined solution preserved a four grid cell resolution of the discontinuity over the whole domain (see Figure 5.15).

5.3 Supersonic Triple Point

The next problem is the triple point problem where two parallel flows with different Mach numbers and densities produce a shock, a contact surface and an expansion region as a result of their interaction. The basic solver without the confinement resolves most of the flow features and the shock is sharper than the contact surface. We used 15 uniformly spaced levels for this and the following contour plots. In Figure 5.17 the contour plot for the confined solution is presented. As we mentioned before, the switch in a solver only detects contact discontinuities and confinement procedure does not seriously affect the shock region and expansion region. At the same time the minor oscillations due to the basic solver result in more pronounced oscillations in the confined solution. To address this problem we tested the confinement procedure with two types of a basic solver. In addition to the central difference scheme with scalar artificial dissipation, the same central difference scheme was used, but with a matrix artificial dissipation that is described in details in Appendix C. Density contours in Figures 5.17, 5.18 demonstrated that the second approach results in less oscillations and sharper resolution at the triple point location. Moreover, the region between the shock wave and the contact surface is resolved with greater accuracy, Figure 5.19. The pressure profiles for the same problem show that near contact discontinuity the pressure is disturbed. Approximate linearization failed in the region with strong gradients and produced disturbances in the variables that are constant according to exact solution. Although it is hard to notice in the scheme with poor resolution for the contact discontinuity, this feature will greatly affect the quality of the solution when it sharply resolved.

5.4 Underexpanded Nozzle Flow

The last problem is an underexpanded nozzle flow. It represents the flowfield within the plumes of an underexpanded axisymmetric nozzle freejet. In particular, we studied a sonic jet exhausting into a quiescent atmosphere. The convection processes in such flow are dominant and we can disregard viscous effects and use the Euler equations

for the numerical simulation. A constant pressure boundary separates the supersonic core from the external quiescent ambient fluid. An accurate resolution of this contact discontinuity is the main requirement for the successful modelling of the problem. The contact surface interacts with the complex supersonic flow in the core region. This has applications to scramjet studies which are complicated by combustion processes and an accurate numerical scheme is an important issue. The only feasible way of solving such problems using traditional shock capturing finite volume or finite element methods is to perform a complicated grid adaptation [76], [77].

At the corner of the nozzle the Prandtl-Meyer expansion develops and after reflection from the constant pressure jet boundary it produces compression waves. For a strongly underexpanded jet with high pressure ratio of the exit and ambient regions they will form a compression waves. Figure 5.20 shows that downstream, the shock formed by coalescence of the waves will curve as it approaches the centerline and instead of the regular reflection from the centerline of symmetry, an imbedded shock wave will appear. An *incident shock* will be followed by *reflected shock*. The imbedded shock is similar to a normal shock wave and is called the *Mach disc* [78]. The subsonic flow behind the Mach disc is bounded by a *slip stream* that originates from the triple-shock point.

The axisymmetric flow is described by the modified system of two-dimensional compressible Euler equations, see Appendix D. The inflow in the exit is set to 1.01 Mach number and the temperature in the reservoir is equal to the temperature of the ambient atmosphere, the pressure ratio of exit to ambient is 6.69 and the pressure in the reservoir is 1.5 atm. The ambient co-flow with the axial velocity corresponding to 0.01 Mach number is used. Non-zero inflow simplifies the boundary conditions and eliminates negative effects of the excessive numerical diffusion near the conner. At the centerline which is used to reduce the numerical domain by one half, we impose the symmetry boundary condition. The outflow condition requires additional attention. Since the flow in the core assumed to be a mixture of supersonic and subsonic regions, the one condition for the subsonic outflow has to be prescribed for the characteristic running upstream. We use approach proposed by Prudhomme and Haj-Hariri [77] and assume quasi-one-dimensional flow inside the jet. The outflow is separated by

bounding supersonic jet. In the upper part of the flow we impose the condition related to the ambient atmosphere and inside the jet we use an interpolated pressure from the supersonic flow region surrounding it as shown in Figure 5.21.

In Figure 5.22 the Mach number contour plot for the central difference calculations with the scalar dissipation is presented. The jet boundary is poorly resolved that leads to poor resolution of the *incident shock* region and the *reflected shock* is hard to recognize. The afterdisk slip line is dissipated also and numerical dissipation make the downstream solution meaningless. Results of 4th-order finite difference (SPARK) code with the Navier-Stokes terms demonstrates similar quality of the solution even with finer mesh [77]. The same code in the inviscid form produces highly unstable results.

The second order central difference solver with the confinement term, Figure 5.23, demonstrates sharp resolution of the free surface and the slip line inside the jet. Note that confinement applied only to the contact discontinuity regions; so, no serious improvement in the shock regions was expected. Moreover, the first ten grid lines on the left are eliminated from the confinement procedure due to problem with the region where two discontinuities, free boundary and shock formation region in our case, are tangent to each other.

The calculations presented here are performed on uniform rectangular grid (40 by 100 grid cells).

5.5 Discussion of Discontinuity Confinement Scheme

Presented discontinuity confinement technique is a new simple method that allows to capture the discontinuities in 3-4 grid cells, whether they are aligned with the grid interfaces or not. Results for the contact surface propagation demonstrate ability of the scheme to preserve the original sharp profile without any sign of dissipation over a very large number of iterations. The two dimensional discontinuity confinement technique uses an anti-diffusion convection idea and the residual distribution approach to

generate multi-dimensional procedure. An additional procedure is required to insure conservative nature of the method. A simple and flexible central difference solver with artificial dissipation was used as a base for the two dimensional solver. Combined with the matrix dissipation, the discontinuity confinement provides sharp resolution with close to monotone profiles across the contact discontinuities. More work remains to be done on a confinement parameter ϵ and sensitivity parameter. Complex geometry with complex boundary conditions will also require special attention to preserve high resolution properties of the procedure on the boundaries. Monotone methods with high resolution in smooth regions and dissipative but monotone behavior in the regions with steep gradient are the best candidates for basic schemes.

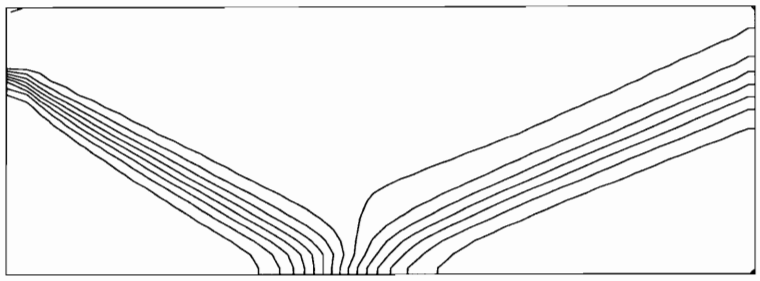

Figure 5.1: Mach number contours, 29^0 shock reflection, 1^{st} order central difference scheme w/o confinement

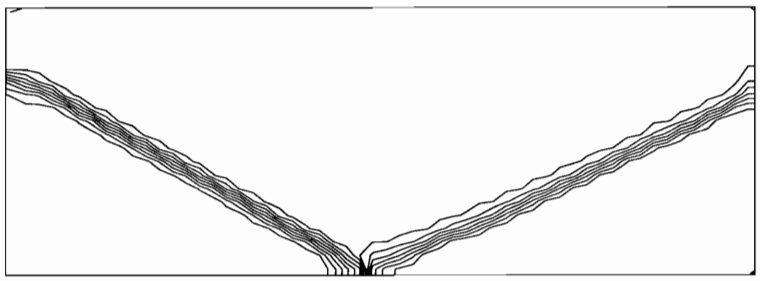

Figure 5.2: Mach number contours, 29^0 shock reflection, 1^{st} order central difference scheme with confinement

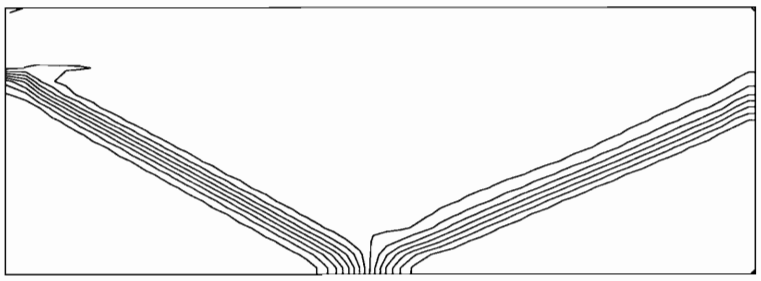

Figure 5.3: Mach number contours, 29^0 shock reflection, central difference scheme with scalar dissipation and w/o confinement

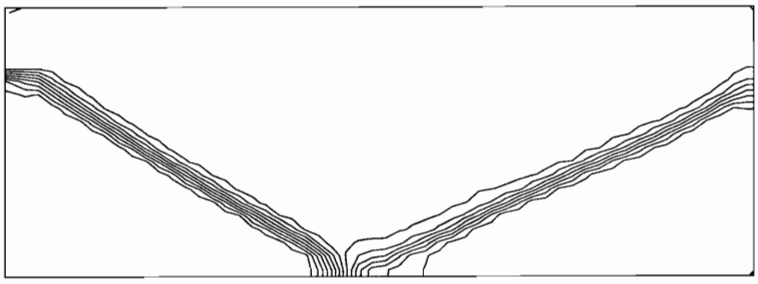

Figure 5.4: Mach number contours, 29^0 shock reflection, 1^{st} order central difference scheme with scalar dissipation and confinement

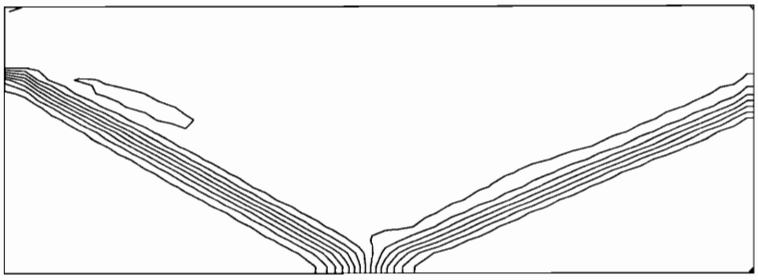

Figure 5.5: Mach number contours, 29^0 shock reflection, central difference scheme with matrix dissipation and w/o confinement

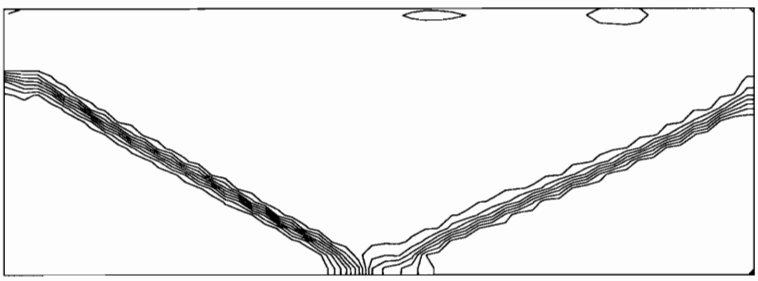

Figure 5.6: Mach number contours, 29^0 shock reflection, 1^{st} order central difference scheme with matrix dissipation and confinement

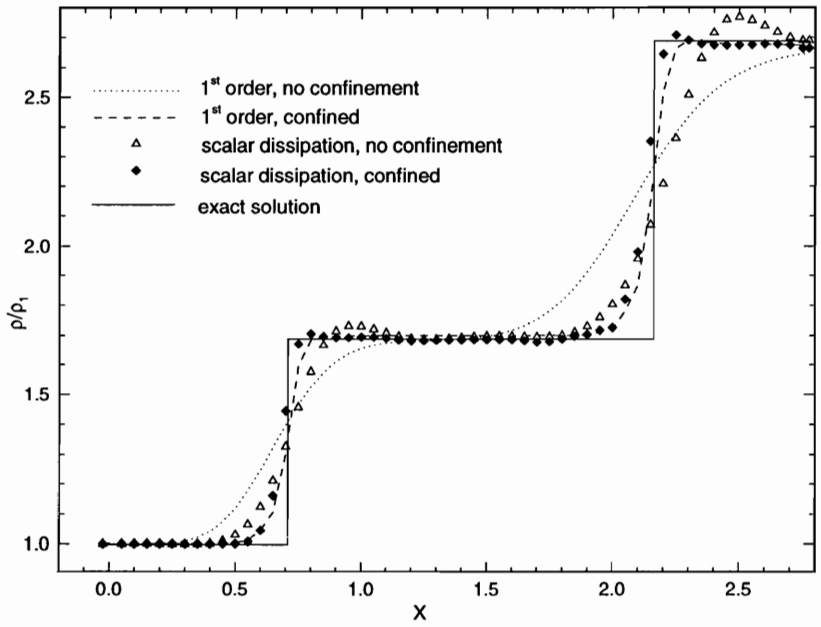

Figure 5.7: Density distribution, 29^0 shock reflection, 1^{st} order and second order central difference with scalar dissipation.

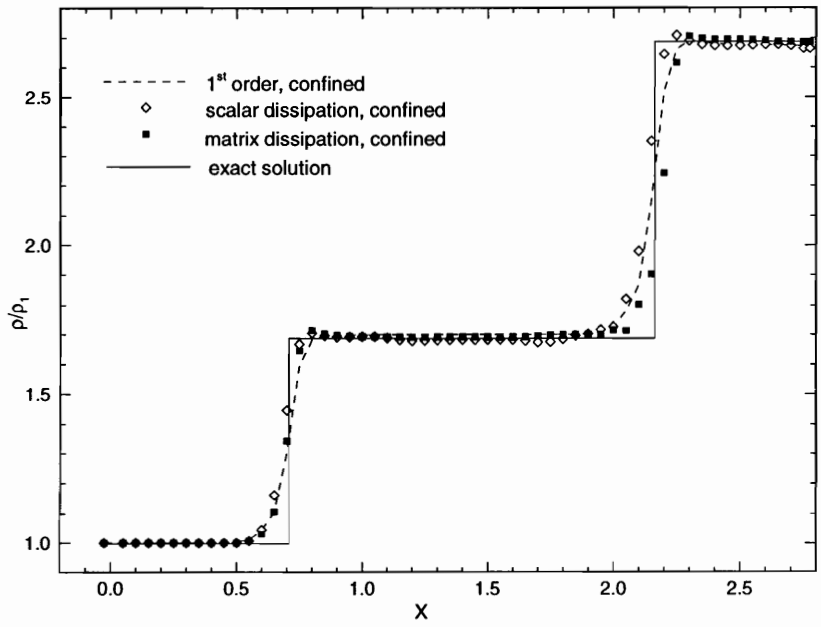

Figure 5.8: Density distribution, 29^0 shock reflection, confined solutions by different schemes.

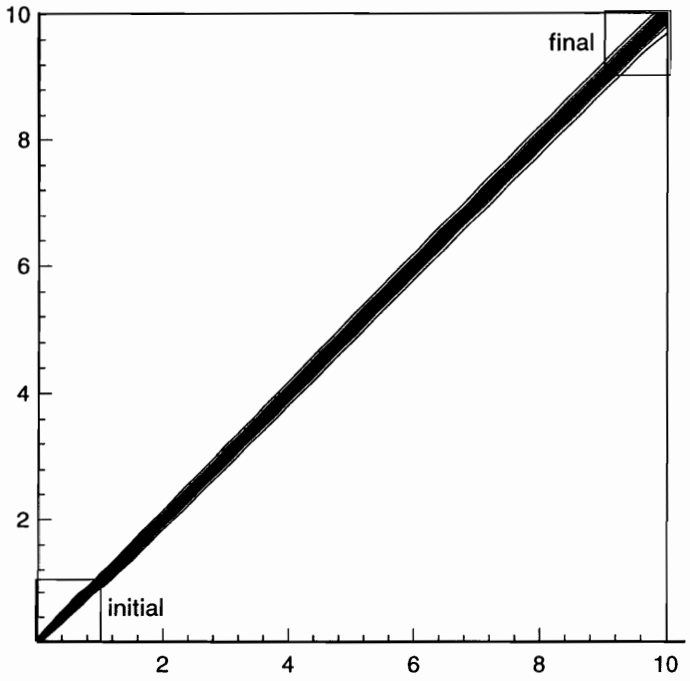

Figure 5.9: An oblique shear layer problem: High-order Roe solver

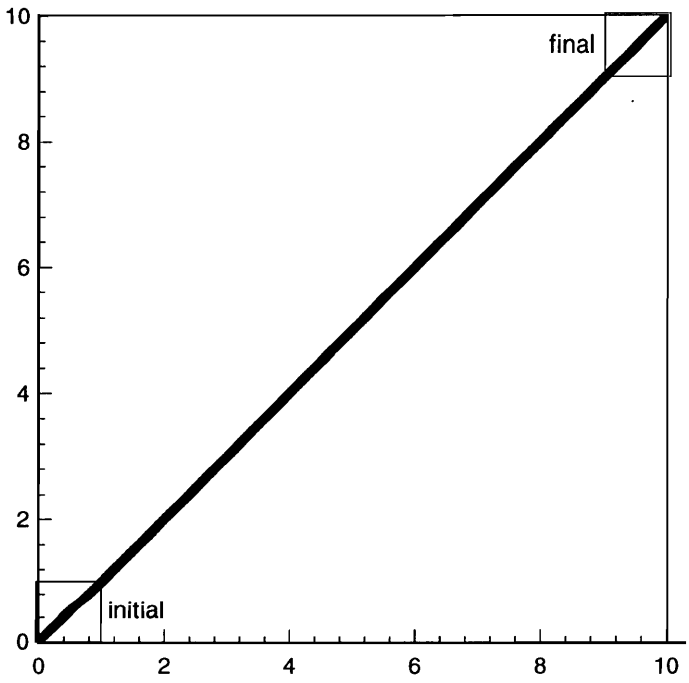

Figure 5.10: An oblique shear layer problem: central difference solver with confinement.

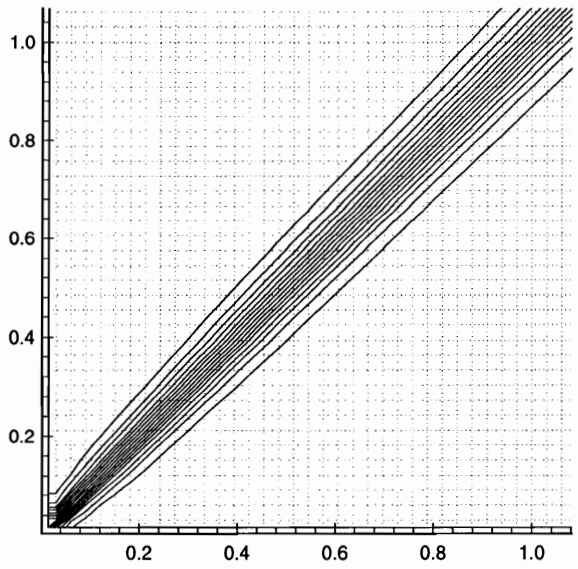

Figure 5.11: Contours at the initial location for the High order Roe solver.

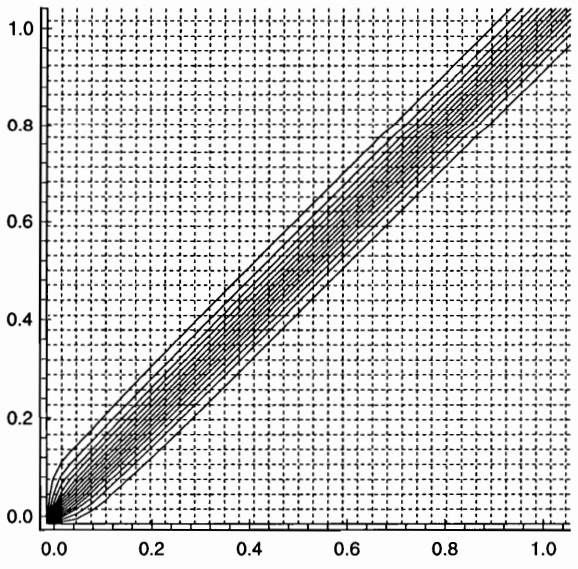

Figure 5.12: Contours at the initial location for the confined solution.

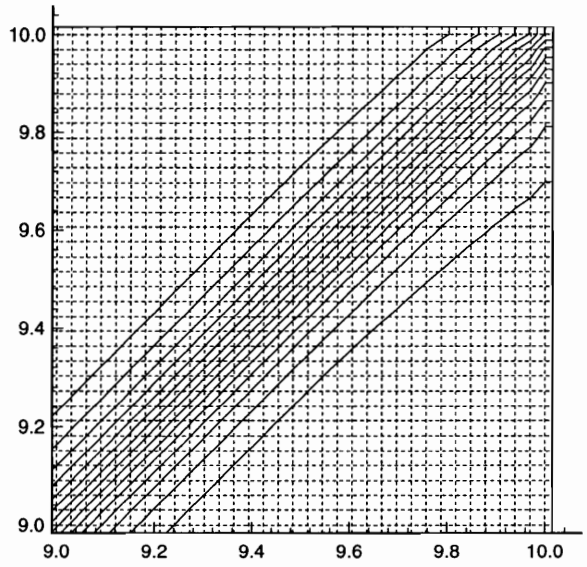

Figure 5.13: Contours at the final location for the High order Roe solver.

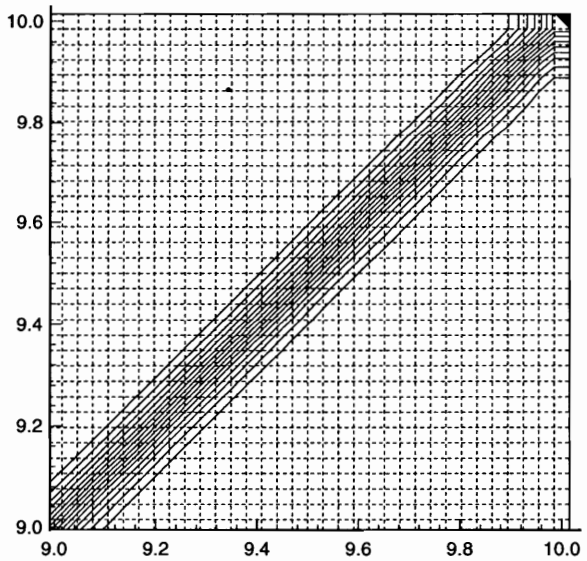

Figure 5.14: Contours at the final location for the confined solution.

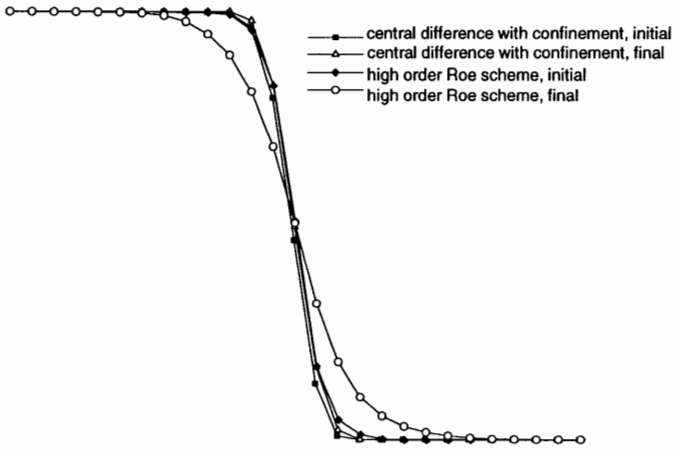

Figure 5.15: Mach number profiles normal to discontinuity for oblique shear layer problem.

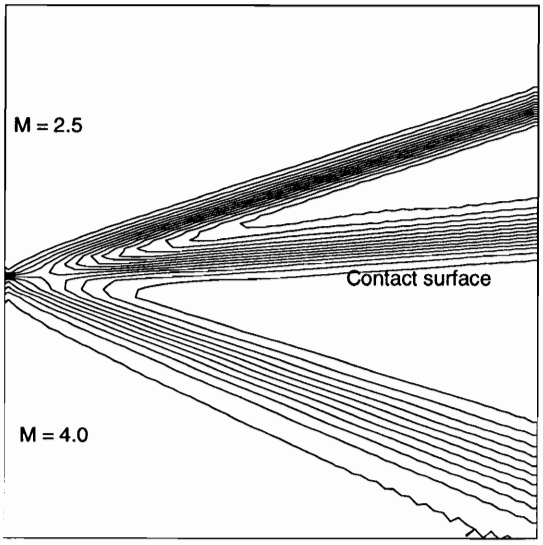

Figure 5.16: Triple point problem, density contours w/o confinement.

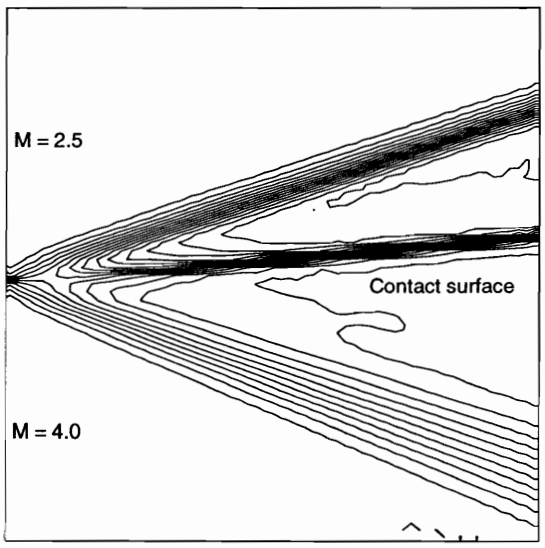

Figure 5.17: Density contours with a scalar artificial dissipation and confinement.

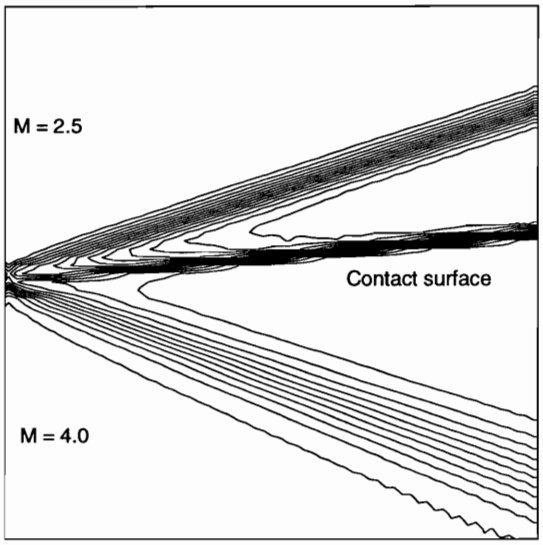

Figure 5.18: Density contours with a matrix artificial dissipation and confinement.

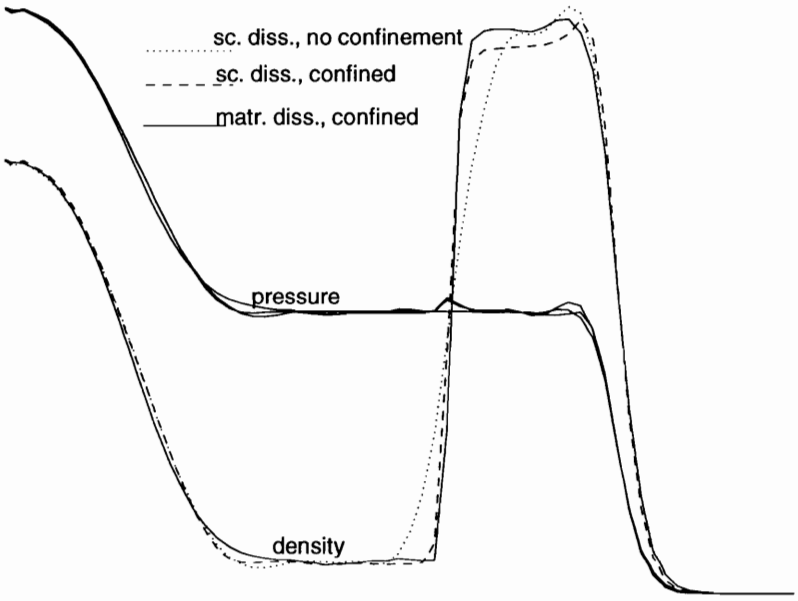

Figure 5.19: Density and pressure profiles at the X=Xmax location.

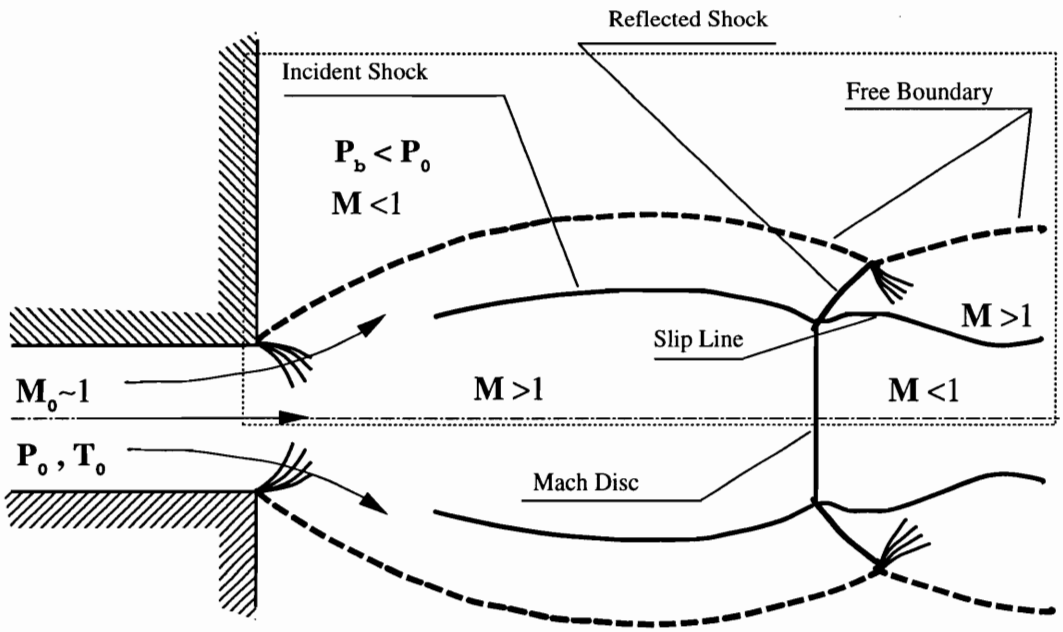

Figure 5.20: A strongly underexpanded jet. Main flow features.

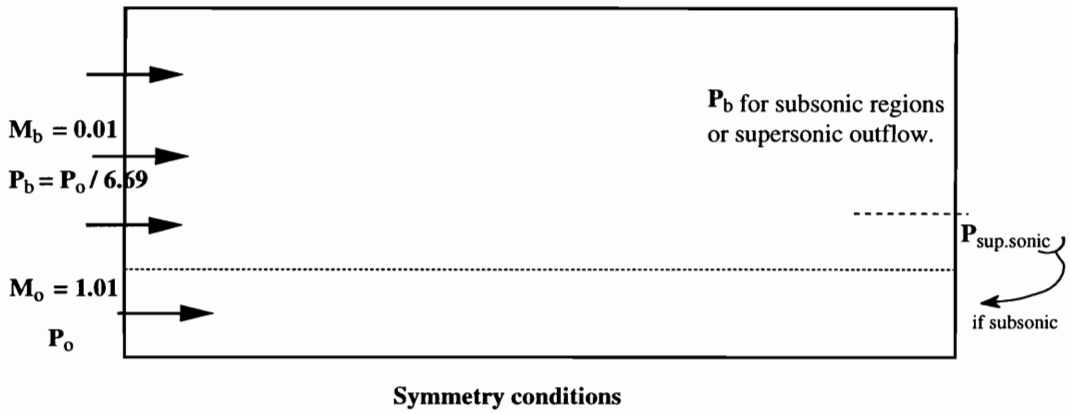

Figure 5.21: A strongly underexpanded jet. Initial and boundary conditions.

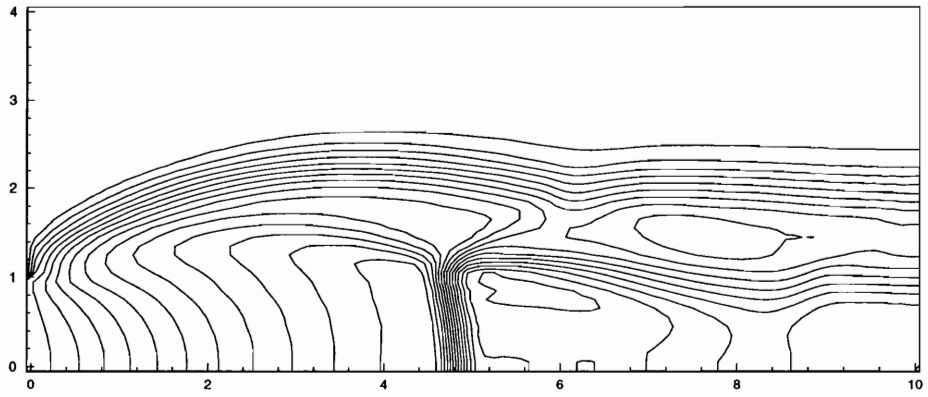

Figure 5.22: A strongly underexpanded jet. Mach number contours w/o confinement.

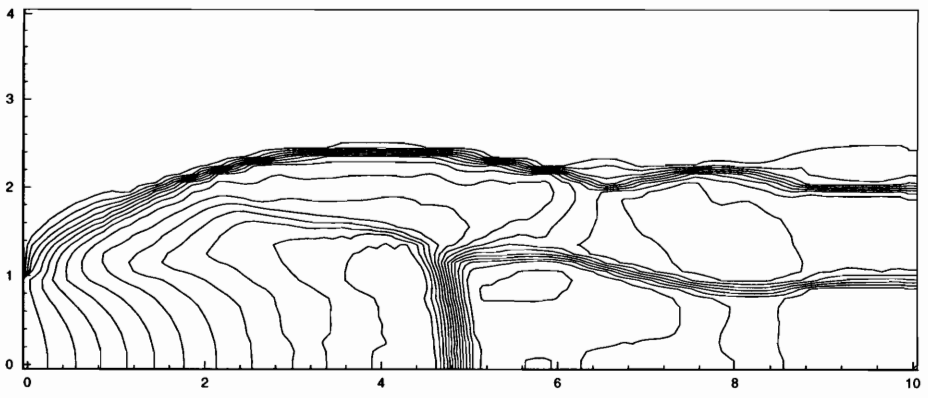

Figure 5.23: A strongly underexpanded jet. Mach number contours with confinement.

Chapter 6

Conclusions

Two distinct approaches to design of the multi-dimensional high resolution methods for the compressible Euler equations were presented. The first is the kinetic fluctuation-splitting scheme based on an LDA-scheme discretization which is a Boltzmann type scheme on a triangulated Cartesian mesh that uses diagonal adaptive strategy. The method follows the work of Eppard and Grossman and completes the series of multi-dimensional Euler solvers with upwinding applied at the kinetic level. The second approach uses an original discontinuity confinement procedure developed in collaboration with Steinhoff and coworkers at UTSI.

The MKFS-LDA scheme is a cell-vertex scheme. It was obtained by taking the moments of the fluctuation in the distribution function that are calculated according to the LDA fluctuation splitting procedure on a kinetic level. The diagonal-adaptive procedure designed by Eppard and Grossman for MKFS-NDA scheme was applied to eliminate the diagonal dependence. Results show improvement over the N-scheme based solvers. Results for a simple oblique-shock reflection and a shear wave demonstrate that the adaptive procedure and the higher order low diffusion scheme provide sharper resolution than the dimensionally-split kinetic CIR scheme and the first order N-scheme. Moreover, no evidence of oscillations near discontinuities was observed but the order of accuracy is probably lower than the second order theoretically predicted accuracy on regular meshes. The extension to the nonlinear scheme, for higher-order spatial accuracy with the positivity property, appears to be very complex to be used

with an analytical integration. The analytical integration which provides acceptable CPU time consumption is not feasible for the non-linear scheme unless a distribution function simpler than Maxwellian is used. Even for the linear schemes the resulting Euler solvers are complex and computationally costly. Comparative study demonstrated four times CPU usage increase for MKFS-LDA scheme compared to dimensional-split high order Roe solver with Van Albada limiter and a similar convergence rate in terms of number of iterations before the steady state solution is reached. Nevertheless, the Boltzmann type schemes are not to be discarded as a CFD tools. The recent success of a kinetic solver based on the BGK approximation to the Boltzmann equation shows the potential of the schemes which are closely related to the physics of the process rather than the mathematical models often used in numerical methods.

The discontinuity procedure is presented in two stages as it was developed. The one dimensional solver in the form of the flux correction was developed and tested on a shock tube problem and on the contact surface propagation problems. It demonstrated exceptional performance and no dissipation over a very large number of iterations. The two dimensional discontinuity confinement technique follows the same trend to use "fluctuation distribution" rather than "flux integration" ideas. The confinement procedure when added to the stable monotone solver provides high quality resolution in the regions of the discontinuities without deteriorating the solution in the smooth regions. Two basic solvers were tested with the new procedure: the Roe flux difference splitting scheme with a first order and a high order MUSCL reconstruction step, and the central difference solver with scalar and matrix artificial dissipation. The Roe scheme in its one-dimensional formulation limits the solver to the dimensional-splitting and was only used in the preliminary one-dimensional tests. A simple and flexible central difference solver with artificial dissipation was used as a base for the two dimensional solver. Combined with the matrix dissipation, the discontinuity confinement provides sharp resolution with close to monotone profiles across the contact discontinuities. There is no sign of smearing in time iteration or over the space domain. Preliminary results for the underexpanded jet problem demonstrate the ability of the discontinuity confinement scheme to provide sharp

profiles in the complex flow.

Future development of the discontinuity confinement method will depend on resolution of the following issues: a) stable second order basic solver with monotone resolution for discontinuous regions has to be used, b) multi-dimensional switch to exclude expansion regions from effect of the confinement is needed for complex flow applications. As numerical study showed, central difference scheme with matrix dissipation generates close to monotone resolution in steep gradient regions and in combination with confinement it provides sharply resolved flow features. One of possible candidates for basic solver is Godunov scheme that will also eliminate problems with linearization and approximation of the physical solution, when nonzero update generated for continuous variables in the discontinuos regions. Multi-dimensional switch that will detect expansion regions and limit or vanish discontinuity confinement in those locations is necessary for a successful implementation of the method for complex flows. It is possible to use multi-dimensional wave decomposition to detect shocks, contact discontinuities, and slip lines. In present study we tried to avoid the use of expensive and unreliable wave decompositions that are used for multi-dimensional upwind schemes.

There is trade-off in CPU consumption when confinement is added to an original solver. Because of the costly conservation procedure included in the discontinuity confinement technique, single time iterations requires three times more CPU time than original central difference solver with matrix dissipation. At the same time for steady state calculations, we used the nonconfined solution as initial solution. The confined solution was recovered after M iterations, where M is the number of grid nodes in the longest dimension of the computational domain. As a result, it does not require threefold CPU usage to calculate confinement solution to problems, and computational overhead is reasonably low.

Appendix A

MKFS schemes: analytical and numerical integration.

A.1 Nomenclature for Integrals in MKFS Schemes

Expressions for the moments that appear in the MKFS-NDD scheme, the MKFS-NDU scheme and the MKFS-LDA scheme are in the following appendices. The results are written in terms of β, defined by Eq. (4), the cell aspect ratio α, defined by Eq. (40), and the Cartesian velocity components u_1 and u_2. The error function $erf(x)$, defined in Eq. (14d), and its complement

$$erfc(x) = 1 - erf(x)\,, \tag{A.1}$$

also appear. It is also convenient to introduce the following notation

$$\bar{u}_1 = \sqrt{\beta} u_1\,, \qquad \bar{u}_2 = \sqrt{\beta} u_2\,, \tag{A.2}$$

$$\bar{v}_1 = \bar{u}_1 \alpha + \bar{u}_2\,, \qquad \bar{v}_2 = \bar{u}_1 - \bar{u}_2 \alpha\,, \tag{A.3}$$

$$\bar{\alpha}_1 = 1/(\sqrt{1+\alpha^2})\,, \qquad \bar{\alpha}_2 = \alpha \bar{\alpha}_1\,, \tag{A.4}$$

$$\bar{w}_1 = \bar{v}_1 \alpha_1\,, \qquad \bar{w}_2 = \bar{v}_2 \alpha_1\,, \tag{A.5}$$

and

$$\bar{\rho}_1 = \frac{\rho}{4\sqrt{\beta\pi}}\,, \quad \bar{\rho}_2 = \frac{\rho}{4\beta\pi}\,, \quad \bar{\rho}_3 = \frac{\rho}{8\pi\beta\sqrt{\beta}}\,. \tag{A.6}$$

One portion of the integration could not be performed analytically. These integrals are given by

$$\Omega_{1,2} = \int_{\mp\bar{u}_1}^{\infty} e^{-z^2} erf(\pm z\alpha + \bar{v}_1) dz \,. \tag{A.7}$$

$$\Omega_3 = \int_{-\bar{u}_1}^{\infty} \frac{e^{-z^2}}{z+\bar{u}_1} [e^{(z\alpha+\bar{v}_1)^2} - e^{-\bar{u}_2^2}] dz \,. \tag{A.8}$$

$$\Omega_4 = \int_{-\bar{u}_1}^{\infty} \frac{e^{-z^2}}{z+\bar{u}_1} [erfc(z\alpha+\bar{v}_1) - erfc(\bar{u}_2)] dz \,. \tag{A.9}$$

Integrals Ω_1, Ω_2 are used for the MKFS-NDA scheme and Ω_3, Ω_4 are used for the MKFS-LDA scheme. Approximate numerical methods for the evaluation of this integral will be presented in Appendix A5.

A.2 Moments for MKFS-NDD Scheme

Expressions for the 48 moments that appear in the MKFS-NDD scheme, defined in Eqs. (43), (51)–(55) are given in this section.

ψ_1 Moments

The ψ_1 moments are determined when the first element of the moment function vector is considered, *i.e.*, $\psi_1 = m$, the molecular mass. The corresponding 12 integrals are given as

$$\begin{aligned} I_D^1(\psi_1) &= \int_{-\infty}^{\infty}\int_{-\infty}^{0}\int_{-\infty}^{0} \rho c_1 f_0 dc_2 dc_1 dc_3 \qquad (A.10)\\ &= \bar{\rho}_1[-e^{-\bar{u}_1^2} + \bar{u}_1\sqrt{\pi}\, erfc(\bar{u}_1)] erfc(\bar{u}_2)\,, \\ I_D^2(\psi_1) &= \int_{-\infty}^{\infty}\int_{-\infty}^{0}\int_{-\infty}^{0} \rho c_2 f_0 dc_2 dc_1 dc_3 \qquad (A.11)\\ &= \bar{\rho}_1[-e^{-\bar{u}_2^2} + \bar{u}_2\sqrt{\pi}\, erfc(\bar{u}_2)] erfc(\bar{u}_1)\,, \\ I_D^3(\psi_1) &= \int_{-\infty}^{\infty}\int_{-\infty}^{0}\int_{0}^{-c_1\alpha} \rho c_1 f_0 dc_2 dc_1 dc_3 \qquad (A.12)\\ &= \bar{\rho}_1[\bar{u}_1\sqrt{\pi}\, erfc(\bar{u}_1) erf(\bar{u}_2) - \bar{\alpha}_2 e^{-\bar{w}_1^2} erfc(\bar{w}_2) - 2\bar{u}_1\Omega_2]\,, \\ I_D^4(\psi_1) &= \int_{-\infty}^{\infty}\int_{-\infty}^{0}\int_{0}^{-c_1\alpha} \rho c_2 f_0 dc_2 dc_1 dc_3 \qquad (A.13) \end{aligned}$$

$$= \bar{\rho}_1[e^{-\bar{u}_2^2} erfc(\bar{u}_1) + \bar{u}_2\sqrt{\pi}\, erf(\bar{u}_2) erfc(\bar{u}_1) - \bar{\alpha}_1 e^{-\bar{w}_1^2} erfc(\bar{w}_2) - 2\bar{u}_2\Omega_2]\,,$$

$$I_D^5(\psi_1) = \int_{-\infty}^{\infty}\int_{0}^{\infty}\int_{-\infty}^{-c_1\alpha} \rho c_1 f_0 dc_2 dc_1 dc_3 \tag{A.14}$$

$$= \bar{\rho}_1[e^{-\bar{u}_1^2} erfc(\bar{u}_2) + \bar{u}_1\sqrt{\pi}\, erfc(-\bar{u}_1) - \bar{\alpha}_2 e^{-\bar{w}_1^2} erfc(-\bar{w}_2) - 2\bar{u}_1\Omega_1]\,,$$

$$I_D^6(\psi_1) = \int_{-\infty}^{\infty}\int_{0}^{\infty}\int_{-\infty}^{-c_1\alpha} \rho c_2 f_0 dc_2 dc_1 dc_3 \tag{A.15}$$

$$= \bar{\rho}_1[\bar{u}_2\sqrt{\pi}\, erfc(-\bar{u}_1) - \bar{\alpha}_1 e^{-\bar{w}_1^2} erfc(-\bar{w}_2) - 2\bar{u}_2\Omega_1]\,,$$

$$I_D^7(\psi_1) = \int_{-\infty}^{\infty}\int_{0}^{\infty}\int_{-c_1\alpha}^{0} \rho c_1 f_0 dc_2 dc_1 dc_3 \tag{A.16}$$

$$= \bar{\rho}_1[-\bar{u}_1\sqrt{\pi}\, erfc(-\bar{u}_1) erf(\bar{u}_2) + \bar{\alpha}_2 e^{-\bar{w}_1^2} erfc(-\bar{w}_2) + 2\bar{u}_1\Omega_1]\,,$$

$$I_D^8(\psi_1) = \int_{-\infty}^{\infty}\int_{0}^{\infty}\int_{-c_1\alpha}^{0} \rho c_2 f_0 dc_2 dc_1 dc_3 \tag{A.17}$$

$$= \bar{\rho}_1[-e^{-\bar{u}_2^2} erfc(-\bar{u}_1) - \bar{u}_2\sqrt{\pi}\, erf(\bar{u}_2) erfc(-\bar{u}_1)$$
$$+\bar{\alpha}_1 e^{-\bar{w}_1^2} erfc(-\bar{w}_2) + 2\bar{u}_2\Omega_1]\,,$$

$$I_D^9(\psi_1) = \int_{-\infty}^{\infty}\int_{0}^{\infty}\int_{0}^{\infty} \rho c_1 f_0 dc_2 dc_1 dc_3 \tag{A.18}$$

$$= \bar{\rho}_1[e^{-\bar{u}_1^2} + \bar{u}_1\sqrt{\pi}\, erfc(-\bar{u}_1)] erfc(-\bar{u}_2)\,,$$

$$I_D^{10}(\psi_1) = \int_{-\infty}^{\infty}\int_{0}^{\infty}\int_{0}^{\infty} \rho c_2 f_0 dc_2 dc_1 dc_3 \tag{A.19}$$

$$= \bar{\rho}_1[e^{-\bar{u}_2^2} + \bar{u}_2\sqrt{\pi}\, erfc(-\bar{u}_2)] erfc(-\bar{u}_1)\,,$$

$$I_D^{11}(\psi_1) = \int_{-\infty}^{\infty}\int_{-\infty}^{0}\int_{-c_1\alpha}^{\infty} \rho c_1 f_0 dc_2 dc_1 dc_3 \tag{A.20}$$

$$= \bar{\rho}_1[-e^{-\bar{u}_1^2} erfc(-\bar{u}_2) + \bar{u}_1\sqrt{\pi}\, erfc(\bar{u}_1) + \bar{\alpha}_2 e^{-\bar{w}_1^2} erfc(\bar{w}_2) + 2\bar{u}_1\Omega_2]\,,$$

$$I_D^{12}(\psi_1) = \int_{-\infty}^{\infty}\int_{-\infty}^{0}\int_{-c_1\alpha}^{\infty} \rho c_2 f_0 dc_2 dc_1 dc_3 \tag{A.21}$$

$$= \bar{\rho}_1[\bar{u}_2\sqrt{\pi}\, erfc(\bar{u}_1) + \bar{\alpha}_1 e^{-\bar{w}_1^2} erfc(\bar{w}_2) + 2\bar{u}_2\Omega_2]\,.$$

ψ_2 Moments

The ψ_2 moments are determined when the second element of the moment function vector is considered,

i.e., $\psi_2 = mc_1$, the molecular momentum in the x_1-direction. The corresponding 12

integrals are given as

$$I_D^1(\psi_2) = \int_{-\infty}^{\infty}\int_{-\infty}^{0}\int_{-\infty}^{0} \rho c_1^2 f_0 dc_2 dc_1 dc_3 \tag{A.22}$$
$$= \bar{\rho}_2[\bar{u}_1\sqrt{\pi}\, e^{-\bar{u}_1^2} erfc(\bar{u}_2) + \frac{\pi}{2}(1+2\bar{u}_1^2) erfc(\bar{u}_1) erfc(\bar{u}_2)]\,,$$

$$I_D^2(\psi_2) = \int_{-\infty}^{\infty}\int_{-\infty}^{0}\int_{-\infty}^{0} \rho c_1 c_2 f_0 dc_2 dc_1 dc_3 \tag{A.23}$$
$$= \bar{\rho}_2[e^{-(\bar{u}_1^2+\bar{u}_2^2)} - \bar{u}_2\sqrt{\pi}\, e^{-\bar{u}_1^2} erfc(\bar{u}_2) - \bar{u}_1\sqrt{\pi}\, e^{-\bar{u}_2^2} erfc(\bar{u}_1)$$
$$+\bar{u}_1\bar{u}_2\pi\, erfc(\bar{u}_1) erfc(\bar{u}_2)]\,,$$

$$I_D^3(\psi_2) = \int_{-\infty}^{\infty}\int_{-\infty}^{0}\int_{0}^{-c_1\alpha} \rho c_1^2 f_0 dc_2 dc_1 dc_3 \tag{A.24}$$
$$= \bar{\rho}_2[\bar{\alpha}_1\bar{\alpha}_2 e^{-(\bar{u}_1^2+\bar{u}_2^2)} + \frac{\pi}{2}(1+2\bar{u}_1^2) erfc(\bar{u}_1) erf(\bar{u}_2)$$
$$-2\sqrt{\pi}\,\bar{\alpha}_1\bar{\alpha}_2\bar{w}_2 e^{-\bar{w}_1^2} erfc(\bar{w}_2) - \sqrt{\pi}\,(1+2\bar{u}_1^2)\Omega_2]\,,$$

$$I_D^4(\psi_2) = \int_{-\infty}^{\infty}\int_{-\infty}^{0}\int_{0}^{-c_1\alpha} \rho c_1 c_2 f_0 dc_2 dc_1 dc_3 \tag{A.25}$$
$$= \bar{\rho}_2[-\bar{\alpha}_2^2 e^{-(\bar{u}_1^2+\bar{u}_2^2)} + \bar{u}_1\sqrt{\pi}\, e^{-\bar{u}_2^2} erfc(\bar{u}_1) + \bar{u}_1\bar{u}_2\pi\, erf(\bar{u}_2) erfc(\bar{u}_1)$$
$$-\sqrt{\pi}\,(\bar{u}_1\bar{\alpha}_1^3 + \bar{u}_2\bar{\alpha}_2^3) e^{-\bar{w}_1^2} erfc(\bar{w}_2) - 2\sqrt{\pi}\,\bar{u}_1\bar{u}_2\Omega_2]\,,$$

$$I_D^5(\psi_2) = \int_{-\infty}^{\infty}\int_{0}^{\infty}\int_{-\infty}^{-c_1\alpha} \rho c_1^2 f_0 dc_2 dc_1 dc_3 \tag{A.26}$$
$$= \bar{\rho}_2[-\bar{\alpha}_1\bar{\alpha}_2 e^{-(\bar{u}_1^2+\bar{u}_2^2)} + \bar{u}_1\sqrt{\pi}\, e^{-\bar{u}_1^2} erfc(\bar{u}_2) + \frac{\pi}{2}(1+2\bar{u}_1^2) erfc(-\bar{u}_1)$$
$$-2\sqrt{\pi}\,\bar{\alpha}_1\bar{\alpha}_2\bar{w}_2 e^{-\bar{w}_1^2} erfc(-\bar{w}_2) - \sqrt{\pi}\,(1+2\bar{u}_1^2)\Omega_1]\,,$$

$$I_D^6(\psi_2) = \int_{-\infty}^{\infty}\int_{0}^{\infty}\int_{-\infty}^{-c_1\alpha} \rho c_1 c_2 f_0 dc_2 dc_1 dc_3 \tag{A.27}$$
$$= \bar{\rho}_2[-\bar{\alpha}_1^2 e^{-(\bar{u}_1^2+\bar{u}_2^2)} + \bar{u}_2\sqrt{\pi}\, e^{-\bar{u}_1^2} erfc(\bar{u}_2) + \bar{u}_1\bar{u}_2\pi\, erfc(-\bar{u}_1)$$
$$-\sqrt{\pi}\,(\bar{u}_1\bar{\alpha}_1^3 + \bar{u}_2\bar{\alpha}_2^3) e^{-\bar{w}_1^2} erfc(-\bar{w}_2) - 2\sqrt{\pi}\,\bar{u}_1\bar{u}_2\Omega_1]\,,$$

$$I_D^7(\psi_2) = \int_{-\infty}^{\infty}\int_{0}^{\infty}\int_{-\infty}^{-c_1\alpha} \rho c_1^2 f_0 dc_2 dc_1 dc_3 \tag{A.28}$$
$$= \bar{\rho}_2[\bar{\alpha}_1\bar{\alpha}_2 e^{-(\bar{u}_1^2+\bar{u}_2^2)} - \frac{\pi}{2}(1+2\bar{u}_1^2) erfc(-\bar{u}_1) erf(\bar{u}_2)$$
$$+2\sqrt{\pi}\,\bar{\alpha}_1\bar{\alpha}_2\bar{w}_2 e^{-\bar{w}_1^2} erfc(-\bar{w}_2) + \sqrt{\pi}\,(1+2\bar{u}_1^2)\Omega_1]\,,$$

$$I_D^8(\psi_2) = \int_{-\infty}^{\infty}\int_{0}^{\infty}\int_{-c_1\alpha}^{0} \rho c_1 c_2 f_0 dc_2 dc_1 dc_3 \tag{A.29}$$

$$= \bar{\rho}_2[-\bar{\alpha}_2^2 e^{-(\bar{u}_1^2+\bar{u}_2^2)} - \bar{u}_1\sqrt{\pi}\, e^{-\bar{u}_2^2} erfc(-\bar{u}_1) - \bar{u}_1\bar{u}_2\pi\, erf(\bar{u}_2)erfc(-\bar{u}_1)$$
$$+\sqrt{\pi}\,(\bar{u}_1\bar{\alpha}_1^3 + \bar{u}_2\bar{\alpha}_2^3)e^{-\bar{w}_1^2} erfc(-\bar{w}_2) + 2\sqrt{\pi}\,\bar{u}_1\bar{u}_2\Omega_1]\,,$$

$$I_D^9(\psi_2) = \int_{-\infty}^{\infty}\int_{0}^{\infty}\int_{-c_1\alpha}^{0} \rho c_1^2 f_0 dc_2 dc_1 dc_3 \tag{A.30}$$
$$= \bar{\rho}_2[\bar{u}_1\sqrt{\pi}\, e^{-\bar{u}_1^2} erfc(-\bar{u}_2) + \frac{\pi}{2}(1+2\bar{u}_1^2)erfc(-\bar{u}_1)erfc(-\bar{u}_2)]\,,$$

$$I_D^{10}(\psi_2) = \int_{-\infty}^{\infty}\int_{0}^{\infty}\int_{0}^{\infty} \rho c_1 c_2 f_0 dc_2 dc_1 dc_3 \tag{A.31}$$
$$= \bar{\rho}_2[e^{-(\bar{u}_1^2+\bar{u}_2^2)} + \bar{u}_2\sqrt{\pi}\, e^{-\bar{u}_1^2} erfc(-\bar{u}_2) + \bar{u}_1\sqrt{\pi}\, e^{-\bar{u}_2^2} erfc(-\bar{u}_1)$$
$$+\bar{u}_1\bar{u}_2\pi\, erfc(-\bar{u}_1)erfc(-\bar{u}_2)]\,,$$

$$I_D^{11}(\psi_2) = \int_{-\infty}^{\infty}\int_{0}^{\infty}\int_{0}^{\infty} \rho c_1^2 f_0 dc_2 dc_1 dc_3 \tag{A.32}$$
$$= \bar{\rho}_2[-\bar{\alpha}_1\bar{\alpha}_2 e^{-(\bar{u}_1^2+\bar{u}_2^2)} - \bar{u}_1\sqrt{\pi}\, e^{-\bar{u}_1^2} erfc(-\bar{u}_2) + \frac{\pi}{2}(1+2\bar{u}_1^2)erfc(\bar{u}_1)$$
$$+2\sqrt{\pi}\,\bar{\alpha}_1\bar{\alpha}_2\bar{w}_2 e^{-\bar{w}_1^2} erfc(\bar{w}_2) + \sqrt{\pi}\,(1+2\bar{u}_1^2)\Omega_2]\,,$$

$$I_D^{12}(\psi_2) = \int_{-\infty}^{\infty}\int_{-\infty}^{0}\int_{-c_1\alpha}^{\infty} \rho c_1 c_2 f_0 dc_2 dc_1 dc_3 \tag{A.33}$$
$$= \bar{\rho}_2[-\bar{\alpha}_1^2 e^{-(\bar{u}_1^2+\bar{u}_2^2)} - \bar{u}_2\sqrt{\pi}\, e^{-\bar{u}_1^2} erfc(-\bar{u}_2) + \bar{u}_1\bar{u}_2\pi\, erfc(\bar{u}_1)$$
$$+\sqrt{\pi}\,(\bar{u}_1\bar{\alpha}_1^3 + \bar{u}_2\bar{\alpha}_2^3)e^{-\bar{w}_1^2} erfc(\bar{w}_2) + 2\sqrt{\pi}\,\bar{u}_1\bar{u}_2\Omega_2]\,.$$

ψ_3 Moments

Likewise, the ψ_3 moments are determined when the third element of the moment function vector is considered, *i.e.*, $\psi_3 = mc_2$, the molecular momentum in the x_2-direction. Here, the odd numbered integrals can be directly related to the even numbered ones in the previous subsection. The 12 integrals are

$$I_D^1(\psi_3) = \int_{-\infty}^{\infty}\int_{-\infty}^{0}\int_{-\infty}^{0} \rho c_1 c_2 f_0 dc_2 dc_1 dc_3 = I_D^2(\psi_2)\,, \tag{A.34}$$

$$I_D^2(\psi_3) = \int_{-\infty}^{\infty}\int_{-\infty}^{0}\int_{-\infty}^{0} \rho c_2^2 f_0 dc_2 dc_1 dc_3 \tag{A.35}$$
$$= \bar{\rho}_2[-\bar{u}_2\sqrt{\pi}\, e^{-\bar{u}_2^2} erfc(\bar{u}_1) + \frac{\pi}{2}(1+2\bar{u}_2^2)erfc(\bar{u}_2)erfc(\bar{u}_1)]\,,$$

$$I_D^3(\psi_3) = \int_{-\infty}^{\infty}\int_{-\infty}^{0}\int_{0}^{-c_1\alpha} \rho c_1 c_2 f_0 dc_2 dc_1 dc_3 = I_D^4(\psi_2)\,, \tag{A.36}$$

$$\begin{aligned} I_D^4(\psi_3) &= \int_{-\infty}^{\infty}\int_{-\infty}^{0}\int_{0}^{-c_1\alpha} \rho c_2^2 f_0 dc_2 dc_1 dc_3 \qquad (A.37)\\ &= \bar{\rho}_2[-\bar{\alpha}_1\bar{\alpha}_2 e^{-(\bar{u}_1^2+\bar{u}_2^2)} + \bar{u}_2\sqrt{\pi}\, e^{-\bar{u}_2^2} erfc(\bar{u}_1) + \frac{\pi}{2}(1+2\bar{u}_2^2) erf(\bar{u}_2) erfc(\bar{u}_1)\\ &\quad +\sqrt{\pi}\,\bar{\alpha}_1(-\bar{\alpha}_1\bar{w}_1 + 2\bar{\alpha}_2\bar{w}_2) e^{-\bar{w}_1^2} erfc(\bar{w}_2) - \sqrt{\pi}\,(1+2\bar{u}_2^2)\Omega_2]\,, \end{aligned}$$

$$I_D^5(\psi_3) = \int_{-\infty}^{\infty}\int_{0}^{\infty}\int_{-\infty}^{-c_1\alpha} \rho c_1 c_2 f_0 dc_2 dc_1 dc_3 = I_D^6(\psi_2)\,, \tag{A.38}$$

$$\begin{aligned} I_D^6(\psi_3) &= \int_{-\infty}^{\infty}\int_{0}^{\infty}\int_{-\infty}^{-c_1\alpha} \rho c_2^2 f_0 dc_2 dc_1 dc_3 \qquad (A.39)\\ &= \bar{\rho}_2[\bar{\alpha}_1\bar{\alpha}_2 e^{-(\bar{u}_1^2+\bar{u}_2^2)} + \frac{\pi}{2}(1+2\bar{u}_2^2) erfc(-\bar{u}_1)\\ &\quad +\sqrt{\pi}\,\bar{\alpha}_1(-\bar{\alpha}_1\bar{w}_1 + 2\bar{\alpha}_2\bar{w}_2) e^{-\bar{w}_1^2} erfc(-\bar{w}_2) - \sqrt{\pi}\,(1+2\bar{u}_2^2)\Omega_1]\,, \end{aligned}$$

$$I_D^7(\psi_3) = \int_{-\infty}^{\infty}\int_{0}^{\infty}\int_{-c_1\alpha}^{0} \rho c_1 c_2 f_0 dc_2 dc_1 dc_3 = I_D^8(\psi_2)\,, \tag{A.40}$$

$$\begin{aligned} I_D^8(\psi_3) &= \int_{-\infty}^{\infty}\int_{0}^{\infty}\int_{-c_1\alpha}^{0} \rho c_2^2 f_0 dc_2 dc_1 dc_3 \qquad (A.41)\\ &= \bar{\rho}_2[-\bar{\alpha}_1\bar{\alpha}_2 e^{-(\bar{u}_1^2+\bar{u}_2^2)} - \bar{u}_2\sqrt{\pi}\, e^{-\bar{u}_2^2} erfc(-\bar{u}_1) - \frac{\pi}{2}(1+2\bar{u}_2^2) erf(\bar{u}_2) erfc(-\bar{u}_1)\\ &\quad -\sqrt{\pi}\,\bar{\alpha}_1(-\bar{\alpha}_1\bar{w}_1 + 2\bar{\alpha}_2\bar{w}_2) e^{-\bar{w}_1^2} erfc(-\bar{w}_2) + \sqrt{\pi}\,(1+2\bar{u}_2^2)\Omega_1]\,, \end{aligned}$$

$$I_D^9(\psi_3) = \int_{-\infty}^{\infty}\int_{0}^{\infty}\int_{0}^{\infty} \rho c_1 c_2 f_0 dc_2 dc_1 dc_3 = I_D^{10}(\psi_2)\,, \tag{A.42}$$

$$\begin{aligned} I_D^{10}(\psi_3) &= \int_{-\infty}^{\infty}\int_{0}^{\infty}\int_{0}^{\infty} \rho c_2^2 f_0 dc_2 dc_1 dc_3 \qquad (A.43)\\ &= \bar{\rho}_2[\bar{u}_2\sqrt{\pi}\, e^{-\bar{u}_2^2} erfc(-\bar{u}_1) + \frac{\pi}{2}(1+2\bar{u}_2^2) erfc(-\bar{u}_2) erfc(-\bar{u}_1)]\,, \end{aligned}$$

$$I_D^{11}(\psi_3) = \int_{-\infty}^{\infty}\int_{-\infty}^{0}\int_{-c_1\alpha}^{\infty} \rho c_1 c_2 f_0 dc_2 dc_1 dc_3 = I_D^{12}(\psi_2)\,, \tag{A.44}$$

$$\begin{aligned} I_D^{12}(\psi_3) &= \int_{-\infty}^{\infty}\int_{-\infty}^{0}\int_{-c_1\alpha}^{\infty} \rho c_2^2 f_0 dc_2 dc_1 dc_3 \qquad (A.45)\\ &= \bar{\rho}_2[\bar{\alpha}_1\bar{\alpha}_2 e^{-(\bar{u}_1^2+\bar{u}_2^2)} + \frac{\pi}{2}(1+2\bar{u}_2^2) erfc(\bar{u}_1)\\ &\quad -\sqrt{\pi}\,\bar{\alpha}_1(-\bar{\alpha}_1\bar{w}_1 + 2\bar{\alpha}_2\bar{w}_2) e^{-\bar{w}_1^2} erfc(\bar{w}_2) + \sqrt{\pi}\,(1+2\bar{u}_2^2)\Omega_2]\,. \end{aligned}$$

ψ_4 Moments

The ψ_4 moments correspond to the integration with respect to the total molecular energy, the fourth element in the moment function vector. It is noted that e' corresponds to average internal energy per unit mass not including the thermal energy of translation. Each of the 12 integrals has the form

$$I_D^j(\psi_4) = I_{jA} + I_{jB} + (\frac{1}{4\beta} + e')I_D^j(\psi_1)\,, \qquad j = 1, 2, ..., 12\,. \tag{A.46}$$

Each of the ψ_4 integrals has a contribution from the corresponding ψ_1 integral and the I_{jA} and I_{jB} terms are given as

$$\begin{aligned} I_{1A} &= \int_{-\infty}^{\infty}\int_{-\infty}^{0}\int_{-\infty}^{0} \rho\left(\frac{c_1^3}{2}\right) f_0 dc_2 dc_1 dc_3 \qquad (A.47)\\ &= \bar{\rho}_3[-\sqrt{\pi}(1+\bar{u}_1^2)e^{-\bar{u}_1^2} erfc(\bar{u}_2) + \frac{\pi}{2}(3\bar{u}_1 + 2\bar{u}_1^3) erfc(\bar{u}_1) erfc(\bar{u}_2)]\,, \end{aligned}$$

$$\begin{aligned} I_{1B} &= \int_{-\infty}^{\infty}\int_{-\infty}^{0}\int_{-\infty}^{0} \rho\left(\frac{c_2^2 c_1}{2}\right) f_0 dc_2 dc_1 dc_3 \qquad (A.48)\\ &= \bar{\rho}_3[\bar{u}_2 e^{-(\bar{u}_1^2+\bar{u}_2^2)} - \bar{u}_1\bar{u}_2\sqrt{\pi}\, e^{-\bar{u}_2^2} erfc(\bar{u}_1) - \frac{\sqrt{\pi}}{2}(1+2\bar{u}_2^2)e^{-\bar{u}_1^2} erfc(\bar{u}_2)\\ &\quad + \frac{\sqrt{\pi}}{2}\bar{u}_1(1+2\bar{u}_2^2) erfc(\bar{u}_2) erfc(\bar{u}_1)]\,, \end{aligned}$$

$$\begin{aligned} I_{2A} &= \int_{-\infty}^{\infty}\int_{-\infty}^{0}\int_{-\infty}^{0} \rho\left(\frac{c_1^2 c_2}{2}\right) f_0 dc_2 dc_1 dc_3 \qquad (A.49)\\ &= \bar{\rho}_3[\bar{u}_1 e^{-(\bar{u}_1^2+\bar{u}_2^2)} - \bar{u}_1\bar{u}_2\sqrt{\pi}\, e^{-\bar{u}_1^2} erfc(\bar{u}_2) - \frac{\sqrt{\pi}}{2}(1+2\bar{u}_1^2)e^{-\bar{u}_2^2} erfc(\bar{u}_1)\\ &\quad + \frac{\pi}{2}\bar{u}_2(1+2\bar{u}_1^2) erfc(\bar{u}_1) erfc(\bar{u}_2)]\,, \end{aligned}$$

$$\begin{aligned} I_{2B} &= \int_{-\infty}^{\infty}\int_{-\infty}^{0}\int_{-\infty}^{0} \rho\left(\frac{c_2^3}{2}\right) f_0 dc_2 dc_1 dc_3 \qquad (A.50)\\ &= \bar{\rho}_3[-\sqrt{\pi}(1+\bar{u}_2^2)e^{-\bar{u}_2^2} erfc(\bar{u}_1) + \frac{\pi}{2}(3\bar{u}_2 + 2\bar{u}_2^3) erfc(\bar{u}_2) erfc(\bar{u}_1)]\,, \end{aligned}$$

$$\begin{aligned} I_{3A} &= \int_{-\infty}^{\infty}\int_{-\infty}^{0}\int_{0}^{-c_1\alpha} \rho\left(\frac{c_1^3}{2}\right) f_0 dc_2 dc_1 dc_3 \qquad (A.51)\\ &= \bar{\rho}_3[\bar{\alpha}_1\bar{\alpha}_2(\bar{\alpha}_2\bar{w}_1 + 2\bar{\alpha}_1\bar{w}_2)e^{-(\bar{u}_1^2+\bar{u}_2^2)} + \frac{\pi}{2}(3\bar{u}_1 + 2\bar{u}_1^3) erfc(\bar{u}_1) erf(\bar{u}_2)\\ &\quad - \frac{\sqrt{\pi}}{2}\{3\bar{\alpha}_1^2\bar{\alpha}_2 + 2\bar{\alpha}_2^3 + \bar{\alpha}_1\bar{\alpha}_2(2\bar{\alpha}_1\bar{\alpha}_2\bar{v}_1^2 + 6\bar{\alpha}_1^2\bar{\alpha}_2\bar{v}_1\bar{v}_2 + 6\bar{\alpha}_1^3\bar{v}_2^2)\}e^{-\bar{w}_1^2} erfc(\bar{w}_2) \end{aligned}$$

$$-\sqrt{\pi}\,\bar{u}_1(3+2\bar{u}_1^2)\Omega_2]\,,$$

$$I_{3B} = \int_{-\infty}^{\infty}\int_{-\infty}^{0}\int_{-\infty}^{-c_1\alpha}\rho\left(\frac{c_2^2c_1}{2}\right)f_0dc_2dc_1dc_3 \tag{A.52}$$

$$= \bar{\rho}_3[-\bar{\alpha}_2(\bar{\alpha}_1^3\bar{u}_1+\bar{\alpha}_2^3\bar{u}_2)e^{-(\bar{u}_1^2+\bar{u}_2^2)}+\sqrt{\pi}\bar{u}_1\bar{u}_2e^{-\bar{u}_2^2}erfc(\bar{u}_1)$$
$$+\frac{\pi}{2}\bar{u}_1(1+2\bar{u}_2^2)erf(\bar{u}_2)erfc(\bar{u}_1)-\frac{\sqrt{\pi}}{2}\{\bar{\alpha}_2^3+2\bar{\alpha}_1^4\bar{\alpha}_2\bar{v}_1^2+2\bar{\alpha}_1^3(3\bar{\alpha}_1^2-2)\bar{v}_1\bar{v}_2$$
$$+2\bar{\alpha}_1^2\bar{\alpha}_2(1-3\bar{\alpha}_1^2)\bar{v}_2^2\}e^{-\bar{w}_1^2}erfc(\bar{w}_2)-\sqrt{\pi}\,\bar{u}_1(1+2\bar{u}_1^2)\Omega_2]\,,$$

$$I_{4A} = \int_{-\infty}^{\infty}\int_{-\infty}^{0}\int_{-\infty}^{-c_1\alpha}\rho\left(\frac{c_1^2c_2}{2}\right)f_0dc_2dc_1dc_3 \tag{A.53}$$

$$= \bar{\rho}_3[-\bar{\alpha}_2^2(\bar{\alpha}_2\bar{w}_1+2\bar{\alpha}_1\bar{w}_2)e^{-(\bar{u}_1^2+\bar{u}_2^2)}+\frac{\sqrt{\pi}}{2}(1+2\bar{u}_1^2)e^{-\bar{u}_2^2}erfc(\bar{u}_1)$$
$$+\frac{\pi}{2}\bar{u}_2(1+2\bar{u}_1^2)erf(\bar{u}_2)erfc(\bar{u}_1)-\frac{\sqrt{\pi}}{2}\{\bar{\alpha}_1^3+4\bar{\alpha}_1^4\bar{\alpha}_2\bar{v}_1\bar{v}_2+2\bar{\alpha}_1(\bar{\alpha}_1^4$$
$$-2\bar{\alpha}_1^2\bar{\alpha}_2^2)\bar{v}_2^2\}e^{-\bar{w}_1^2}erfc(\bar{w}_2)-\sqrt{\pi}\,\bar{u}_2(1+2\bar{u}_1^2)\Omega_2]\,,$$

$$I_{4B} = \int_{-\infty}^{\infty}\int_{-\infty}^{0}\int_{-\infty}^{-c_1\alpha}\rho\left(\frac{c_2^3}{2}\right)f_0dc_2dc_1dc_3 \tag{A.54}$$

$$= \bar{\rho}_3[\bar{\alpha}_1\bar{\alpha}_2(-\bar{\alpha}_1\bar{w}_1+2\bar{\alpha}_2\bar{w}_2)e^{-(\bar{u}_1^2+\bar{u}_2^2)}+\sqrt{\pi}\,(1+\bar{u}_2^2)e^{-\bar{u}_2^2}erfc(\bar{u}_1)$$
$$+\frac{\pi}{2}(3\bar{u}_2+2\bar{u}_2^3)erf(\bar{u}_2)erfc(\bar{u}_1)-\frac{\sqrt{\pi}}{2}(2\bar{\alpha}_1^3+3\bar{\alpha}_1\bar{\alpha}_2^2+2\bar{\alpha}_1^5\bar{v}_1^2-6\bar{\alpha}_1^4\bar{\alpha}_2\bar{v}_1\bar{v}_2$$
$$+6\bar{\alpha}_1^3\bar{\alpha}_2^2\bar{v}_2^2)e^{-\bar{w}_1^2}erfc(\bar{w}_2)-\sqrt{\pi}\,\bar{u}_2(3+2\bar{u}_2^2)\Omega_2]\,,$$

$$I_{5A} = \int_{-\infty}^{\infty}\int_{0}^{\infty}\int_{-\infty}^{-c_1\alpha}\rho\left(\frac{c_1^3}{2}\right)f_0dc_2dc_1dc_3 \tag{A.55}$$

$$= \bar{\rho}_3[-\bar{\alpha}_1\bar{\alpha}_2(\bar{\alpha}_2\bar{w}_1+2\bar{\alpha}_1\bar{w}_2)e^{-(\bar{u}_1^2+\bar{u}_2^2)}+\sqrt{\pi}\,(1+\bar{u}_1^2)e^{-\bar{u}_1^2}erfc(\bar{u}_2)$$
$$+\frac{\pi}{2}(3\bar{u}_1+2\bar{u}_1^3)erfc(-\bar{u}_1)-\frac{\sqrt{\pi}}{2}\{3\bar{\alpha}_1^2\bar{\alpha}_2+2\bar{\alpha}_2^3+\bar{\alpha}_1\bar{\alpha}_2(2\bar{\alpha}_1\bar{\alpha}_2^2\bar{v}_1^2$$
$$+6\bar{\alpha}_1^2\bar{\alpha}_2\bar{v}_1\bar{v}_2+6\bar{\alpha}_1^3\bar{v}_2^2)\}e^{-\bar{w}_1^2}erfc(-\bar{w}_2)-\sqrt{\pi}\,\bar{u}_1(3+2\bar{u}_1^2)\Omega_1]\,,$$

$$I_{5B} = \int_{-\infty}^{\infty}\int_{0}^{\infty}\int_{-\infty}^{-c_1\alpha}\rho\left(\frac{c_2^2c_1}{2}\right)f_0dc_2dc_1dc_3 \tag{A.56}$$

$$= \bar{\rho}_3[\bar{\alpha}_1^2(-\bar{\alpha}_1\bar{w}_1+2\bar{\alpha}_2\bar{w}_2)e^{-(\bar{u}_1^2+\bar{u}_2^2)}+\frac{\sqrt{\pi}}{2}(1+2\bar{u}_2^2)e^{-\bar{u}_1^2}erfc(\bar{u}_2)$$
$$+\frac{\pi}{2}\bar{u}_1(1+2\bar{u}_2^2)erfc(-\bar{u}_1)-\frac{\sqrt{\pi}}{2}\{\bar{\alpha}_2^3+2\bar{\alpha}_1^4\bar{\alpha}_2\bar{v}_1^2+2\bar{\alpha}_1^3(3\bar{\alpha}_1^2-2)\bar{v}_1\bar{v}_2$$
$$+2\bar{\alpha}_1^2\bar{\alpha}_2(1-3\bar{\alpha}_1^2)\bar{v}_2^2\}e^{-\bar{w}_1^2}erfc(-\bar{w}_2)-\sqrt{\pi}\,\bar{u}_1(1+2\bar{u}_2^2)\Omega_1]\,,$$

$$I_{6A} = \int_{-\infty}^{\infty}\int_{0}^{\infty}\int_{-\infty}^{-c_1\alpha}\rho\left(\frac{c_1^2c_2}{2}\right)f_0dc_2dc_1dc_3 \tag{A.57}$$

$$= \bar{\rho}_3[-\bar{\alpha}_1(\bar{\alpha}_1^3\bar{u}_1+\bar{\alpha}_2^3\bar{u}_2)e^{-(\bar{u}_1^2+\bar{u}_2^2)}+\sqrt{\pi}\bar{u}_1\bar{u}_2e^{-\bar{u}_1^2}erfc(\bar{u}_2)$$
$$+\frac{\pi}{2}\bar{u}_2(1+2\bar{u}_1^2)erfc(-\bar{u}_1)-\frac{\sqrt{\pi}}{2}\{\bar{\alpha}_1^3+4\bar{\alpha}_1^4\bar{\alpha}_2\bar{v}_1\bar{v}_2$$
$$+2\bar{\alpha}_1(\bar{\alpha}_1^4-2\bar{\alpha}_1^2\bar{\alpha}_2^2)\bar{v}_2^2\}e^{-\bar{w}_1^2}erfc(-\bar{w}_2)-\sqrt{\pi}\,\bar{u}_2(1+2\bar{u}_1^2)\Omega_1]\,,$$

$$I_{6B} = \int_{-\infty}^{\infty}\int_{0}^{\infty}\int_{-\infty}^{-c_1\alpha}\rho\left(\frac{c_2^3}{2}\right)f_0dc_2dc_1dc_3 \tag{A.58}$$

$$= \bar{\rho}_3[-\bar{\alpha}_1\bar{\alpha}_2(-\bar{\alpha}_1\bar{w}_1+2\bar{\alpha}_2\bar{w}_2)e^{-(\bar{u}_1^2+\bar{u}_2^2)}+\frac{\pi}{2}\,(3\bar{u}_2+2\bar{u}_2^3)erfc(-\bar{u}_1)$$
$$-\frac{\sqrt{\pi}}{2}(2\bar{\alpha}_1^3+3\bar{\alpha}_1\bar{\alpha}_2^2+2\bar{\alpha}_1^5\bar{v}_1^2-6\bar{\alpha}_1^4\bar{\alpha}_2\bar{v}_1\bar{v}_2+6\bar{\alpha}_1^3\bar{\alpha}_2^2\bar{v}_2^2)e^{-\bar{w}_1^2}erfc(-\bar{w}_2)$$
$$-\sqrt{\pi}\,\bar{u}_2(3+2\bar{u}_2^2)\Omega_1]\,,$$

$$I_{7A} = \int_{-\infty}^{\infty}\int_{0}^{\infty}\int_{-c_1\alpha}^{0}\rho\left(\frac{c_1^3}{2}\right)f_0dc_2dc_1dc_3 \tag{A.59}$$

$$= \bar{\rho}_3[\bar{\alpha}_1\bar{\alpha}_2(\bar{\alpha}_2\bar{w}_1+2\bar{\alpha}_1\bar{w}_2)e^{-(\bar{u}_1^2+\bar{u}_2^2)}-\frac{\pi}{2}(3\bar{u}_1+2\bar{u}_1^3)erfc(-\bar{u}_1)erf(\bar{u}_2)$$
$$+\frac{\sqrt{\pi}}{2}\{3\bar{\alpha}_1^2\bar{\alpha}_2+2\bar{\alpha}_2^3+\bar{\alpha}_1\bar{\alpha}_2(2\bar{\alpha}_1\bar{\alpha}_2^2\bar{v}_1^2+6\bar{\alpha}_1^2\bar{\alpha}_2\bar{v}_1\bar{v}_2+\bar{\alpha}_1^3\bar{v}_2^2)\}e^{-\bar{w}_1^2}erfc(-\bar{w}_2)$$
$$+\sqrt{\pi}\,\bar{u}_1(3+2\bar{u}_1^2)\Omega_1]\,,$$

$$I_{7B} = \int_{-\infty}^{\infty}\int_{0}^{\infty}\int_{-c_1\alpha}^{0}\rho\left(\frac{c_2^2c_1}{2}\right)f_0dc_2dc_1dc_3 \tag{A.60}$$

$$= \bar{\rho}_3[-\bar{\alpha}_2(\bar{\alpha}_1^3\bar{u}_1+\bar{\alpha}_2^3\bar{u}_2)e^{-(\bar{u}_1^2+\bar{u}_2^2)}-\sqrt{\pi}\bar{u}_1\bar{u}_2e^{-\bar{u}_2^2}erfc(-\bar{u}_1)$$
$$-\frac{\pi}{2}\bar{u}_1(1+2\bar{u}_2^2)erf(\bar{u}_2)erfc(-\bar{u}_1)+\frac{\sqrt{\pi}}{2}\{\bar{\alpha}_2^3+2\bar{\alpha}_1^4\bar{\alpha}_2\bar{v}_1^2+2\bar{\alpha}_1^3(3\bar{\alpha}_1^2-2)\bar{v}_1\bar{v}_2$$
$$+2\bar{\alpha}_1^2\bar{\alpha}_2(1-3\bar{\alpha}_1^2)\bar{v}_2^2\}e^{-\bar{w}_1^2}erfc(-\bar{w}_2)+\sqrt{\pi}\,\bar{u}_1(1+2\bar{u}_2^2)\Omega_1]\,,$$

$$I_{8A} = \int_{-\infty}^{\infty}\int_{0}^{\infty}\int_{-c_1\alpha}^{0}\rho\left(\frac{c_1^2c_2}{2}\right)f_0dc_2dc_1dc_3 \tag{A.61}$$

$$= \bar{\rho}_3[-\bar{\alpha}_2^2(\bar{\alpha}_2\bar{w}_1+2\bar{\alpha}_1\bar{w}_2)e^{-(\bar{u}_1^2+\bar{u}_2^2)}-\frac{\sqrt{\pi}}{2}(1+2\bar{u}_1^2)e^{-\bar{u}_2^2}erfc(-\bar{u}_1)$$
$$-\frac{\pi}{2}\bar{u}_2(1+2\bar{u}_1^2)erf(\bar{u}_2)erfc(-\bar{u}_1)+\frac{\sqrt{\pi}}{2}\{\bar{\alpha}_1^3+4\bar{\alpha}_1^4\bar{\alpha}_2\bar{v}_1\bar{v}_2+2\bar{\alpha}_1(\bar{\alpha}_1^4$$
$$-2\bar{\alpha}_1^2\bar{\alpha}_2^2)\bar{v}_2^2\}e^{-\bar{w}_1^2}erfc(-\bar{w}_2)+\sqrt{\pi}\,\bar{u}_2(1+2\bar{u}_1^2)\Omega_1]\,,$$

$$I_{8B} = \int_{-\infty}^{\infty}\int_{0}^{\infty}\int_{-c_1\alpha}^{0}\rho\left(\frac{c_2^3}{2}\right)f_0dc_2dc_1dc_3 \tag{A.62}$$

$$
\begin{aligned}
&= \bar{\rho}_3[\bar{\alpha}_1\bar{\alpha}_2(-\bar{\alpha}_1\bar{w}_1+2\bar{\alpha}_2\bar{w}_2)e^{-(\bar{u}_1^2+\bar{u}_2^2)}-\sqrt{\pi}\,(1+\bar{u}_2^2)e^{-\bar{u}_2^2}erfc(-\bar{u}_1)\\
&\quad -\frac{\pi}{2}(3\bar{u}_2+2\bar{u}_2^3)erf(\bar{u}_2)erfc(-\bar{u}_1)+\frac{\sqrt{\pi}}{2}(2\bar{\alpha}_1^3+3\bar{\alpha}_1\bar{\alpha}_2^2+2\bar{\alpha}_1^5\bar{v}_1^2-6\bar{\alpha}_1^4\bar{\alpha}_2\bar{v}_1\bar{v}_2\\
&\quad +6\bar{\alpha}_1^3\bar{\alpha}_2^2\bar{v}_2^2)e^{-\bar{w}_1^2}erfc(-\bar{w}_2)+\sqrt{\pi}\,\bar{u}_2(3+2\bar{u}_2^2)\Omega_1]\,,
\end{aligned}
$$

$$
I_{9A} = \int_{-\infty}^{\infty}\int_{0}^{\infty}\int_{0}^{\infty}\rho\left(\frac{c_1^3}{2}\right)f_0 dc_2 dc_1 dc_3 \tag{A.63}
$$

$$
= \bar{\rho}_3[\sqrt{\pi}(1+\bar{u}_1^2)e^{-\bar{u}_1^2}erfc(-\bar{u}_2)+\frac{\pi}{2}(3\bar{u}_1+2\bar{u}_1^3)erfc(-\bar{u}_1)erfc(-\bar{u}_2)]\,,
$$

$$
I_{9B} = \int_{-\infty}^{\infty}\int_{0}^{\infty}\int_{0}^{\infty}\rho\left(\frac{c_2^2c_1}{2}\right)f_0 dc_2 dc_1 dc_3 \tag{A.64}
$$

$$
\begin{aligned}
&= \bar{\rho}_3[\bar{u}_2e^{-(\bar{u}_1^2+\bar{u}_2^2)}+\bar{u}_1\bar{u}_2\sqrt{\pi}\,e^{-\bar{u}_2^2}erfc(-\bar{u}_1)+\frac{\sqrt{\pi}}{2}(1+2\bar{u}_2^2)e^{-\bar{u}_1^2}erfc(-\bar{u}_2)\\
&\quad +\frac{\pi}{2}\bar{u}_1(1+2\bar{u}_2^2)erfc(-\bar{u}_2)erfc(-\bar{u}_1)]\,,
\end{aligned}
$$

$$
I_{10A} = \int_{-\infty}^{\infty}\int_{0}^{\infty}\int_{0}^{\infty}\rho\left(\frac{c_1^2c_2}{2}\right)f_0 dc_2 dc_1 dc_3 \tag{A.65}
$$

$$
\begin{aligned}
&= \bar{\rho}_3[\bar{u}_1e^{-(\bar{u}_1^2+\bar{u}_2^2)}+\bar{u}_1\bar{u}_2\sqrt{\pi}\,e^{-\bar{u}_1^2}erfc(-\bar{u}_2)+\frac{\sqrt{\pi}}{2}(1+2\bar{u}_1^2)e^{-\bar{u}_2^2}erfc(-\bar{u}_1)\\
&\quad +\frac{\pi}{2}\bar{u}_2(1+2\bar{u}_1^2)erfc(-\bar{u}_1)erfc(-\bar{u}_2)]\,,
\end{aligned}
$$

$$
I_{10B} = \int_{-\infty}^{\infty}\int_{0}^{\infty}\int_{0}^{\infty}\rho\left(\frac{c_2^3}{2}\right)f_0 dc_2 dc_1 dc_3 \tag{A.66}
$$

$$
= \bar{\rho}_3[\sqrt{\pi}(1+\bar{u}_2^2)e^{-\bar{u}_2^2}erfc(-\bar{u}_1)+\frac{\pi}{2}(3\bar{u}_2+2\bar{u}_2^3)erfc(-\bar{u}_2)erfc(-\bar{u}_1)]\,,
$$

$$
I_{11A} = \int_{-\infty}^{\infty}\int_{-\infty}^{0}\int_{-c_1\alpha}^{\infty}\rho\left(\frac{c_1^3}{2}\right)f_0 dc_2 dc_1 dc_3 \tag{A.67}
$$

$$
\begin{aligned}
&= \bar{\rho}_3[-\bar{\alpha}_1\bar{\alpha}_2(\bar{\alpha}_2\bar{w}_1+2\bar{\alpha}_1\bar{w}_2)e^{-(\bar{u}_1^2+\bar{u}_2^2)}-\sqrt{\pi}\,(1+\bar{u}_1^2)e^{-\bar{u}_1^2}erfc(-\bar{u}_2)\\
&\quad +\frac{\pi}{2}(3\bar{u}_1+2\bar{u}_1^3)erfc(\bar{u}_1)+\frac{\sqrt{\pi}}{2}\{3\bar{\alpha}_1^2\bar{\alpha}_2+2\bar{\alpha}_2^3+\bar{\alpha}_1\bar{\alpha}_2(2\bar{\alpha}_1\bar{\alpha}_2^2\bar{v}_1^2\\
&\quad +6\bar{\alpha}_1^2\bar{\alpha}_2\bar{v}_1\bar{v}_2+6\bar{\alpha}_1^3\bar{v}_2^2)\}e^{-\bar{w}_1^2}erfc(\bar{w}_2)+\sqrt{\pi}\,\bar{u}_1(3+2\bar{u}_1^2)\Omega_2]\,,
\end{aligned}
$$

$$
I_{11B} = \int_{-\infty}^{\infty}\int_{-\infty}^{0}\int_{-c_1\alpha}^{\infty}\rho\left(\frac{c_2^2c_1}{2}\right)f_0 dc_2 dc_1 dc_3 \tag{A.68}
$$

$$
= \bar{\rho}_3[\bar{\alpha}_1^2(-\bar{\alpha}_1\bar{w}_1+2\bar{\alpha}_2\bar{w}_2)e^{-(\bar{u}_1^2+\bar{u}_2^2)}-\frac{\sqrt{\pi}}{2}(1+2\bar{u}_2^2)e^{-\bar{u}_1^2}erfc(-\bar{u}_2)
$$

$$+\frac{\pi}{2}\bar{u}_1(1+2\bar{u}_2^2)erfc(\bar{u}_1)+\frac{\sqrt{\pi}}{2}\{\bar{\alpha}_2^3+2\bar{\alpha}_1^4\bar{\alpha}_2\bar{v}_1^2+2\bar{\alpha}_1^3(3\bar{\alpha}_1^2-2)\bar{v}_1\bar{v}_2$$
$$+2\bar{\alpha}_1^2\bar{\alpha}_2(1-3\bar{\alpha}_1^2)\bar{v}_2^2\}e^{-\bar{w}_1^2}erfc(\bar{w}_2)+\sqrt{\pi}\,\bar{u}_1(1+2\bar{u}_2^2)\Omega_2]\,,$$

$$I_{12A} = \int_{-\infty}^{\infty}\int_{-\infty}^{0}\int_{-c_1\alpha}^{\infty}\rho\left(\frac{c_1^2c_2}{2}\right)f_0dc_2dc_1dc_3 \tag{A.69}$$
$$= \bar{\rho}_3[-\bar{\alpha}_1(\bar{\alpha}_1^3\bar{u}_1+\bar{\alpha}_2^3\bar{u}_2)e^{-(\bar{u}_1^2+\bar{u}_2^2)}-\sqrt{\pi}\bar{u}_1\bar{u}_2e^{-\bar{u}_1^2}erfc(-\bar{u}_2)$$
$$+\frac{\pi}{2}\bar{u}_2(1+2\bar{u}_1^2)erfc(\bar{u}_1)+\frac{\sqrt{\pi}}{2}\{\bar{\alpha}_1^3+4\bar{\alpha}_1^4\bar{\alpha}_2\bar{v}_1\bar{v}_2$$
$$+2\bar{\alpha}_1(\bar{\alpha}_1^4-2\bar{\alpha}_1^2\bar{\alpha}_2^2)\bar{v}_2^2\}e^{-\bar{w}_1^2}erfc(\bar{w}_2)+\sqrt{\pi}\,\bar{u}_2(1+2\bar{u}_1^2)\Omega_2]\,,$$

$$I_{12B} = \int_{-\infty}^{\infty}\int_{-\infty}^{0}\int_{-c_1\alpha}^{\infty}\rho\left(\frac{c_2^3}{2}\right)f_0dc_2dc_1dc_3 \tag{A.70}$$
$$= \bar{\rho}_3[-\bar{\alpha}_1\bar{\alpha}_2(-\bar{\alpha}_1\bar{w}_1+2\bar{\alpha}_2\bar{w}_2)e^{-(\bar{u}_1^2+\bar{u}_2^2)}+\frac{\pi}{2}(3\bar{u}_2+2\bar{u}_2^3)erfc(\bar{u}_1)$$
$$+\frac{\sqrt{\pi}}{2}(2\bar{\alpha}_1^3+3\bar{\alpha}_1\bar{\alpha}_2^2+2\bar{\alpha}_1^5\bar{v}_1^2-6\bar{\alpha}_1^4\bar{\alpha}_2\bar{v}_1\bar{v}_2+6\bar{\alpha}_1^3\bar{\alpha}_2^2\bar{v}_2^2)e^{-\bar{w}_1^2}erfc(\bar{w}_2)$$
$$+\sqrt{\pi}\,\bar{u}_2(3+2\bar{u}_2^2)\Omega_2]\,.$$

A.3 Moments for MKFS-NDU Scheme

The moments necessary for the MKFS-NDU scheme can be written in terms of the moments for the NDD-scheme through a change in variables. The relationships are given using a compact notation as follows. For the (l,m) pairs $(1,1)$, $(3,5)$, $(5,7)$, $(7,9)$, $(9,11)$, $(11,3)$,

$$I_U^l(\psi_1)[\bar{u}_1,\bar{u}_2] = I_D^m(\psi_1)[\bar{u}_1,-\bar{u}_2]\,, \tag{A.71}$$
$$I_U^l(\psi_2)[\bar{u}_1,\bar{u}_2] = I_D^m(\psi_2)[\bar{u}_1,-\bar{u}_2]\,, \tag{A.72}$$
$$I_U^l(\psi_3)[\bar{u}_1,\bar{u}_2] = -I_D^m(\psi_3)[\bar{u}_1,-\bar{u}_2]\,, \tag{A.73}$$
$$I_U^l(\psi_4)[\bar{u}_1,\bar{u}_2] = I_D^m(\psi_4)[\bar{u}_1,-\bar{u}_2]\,, \tag{A.74}$$

and for the (l,m) pairs $(2,2)$, $(4,6)$, $(6,8)$, $(8,10)$, $(10,12)$, $(12,4)$,

$$I_U^l(\psi_1)[\bar{u}_1, \bar{u}_2] = -I_D^m(\psi_1)[\bar{u}_1, -\bar{u}_2]\,, \tag{A.75}$$

$$I_U^l(\psi_2)[\bar{u}_1, \bar{u}_2] = -I_D^m(\psi_2)[\bar{u}_1, -\bar{u}_2]\,, \tag{A.76}$$

$$I_U^l(\psi_3)[\bar{u}_1, \bar{u}_2] = I_D^m(\psi_3)[\bar{u}_1, -\bar{u}_2]\,, \tag{A.77}$$

$$I_U^l(\psi_4)[\bar{u}_1, \bar{u}_2] = -I_D^m(\psi_4)[\bar{u}_1, -\bar{u}_2]\,. \tag{A.78}$$

A.4 Moments for MKFS-LDA Scheme

The expressions for the moments for the MKFS-LDA Scheme are given in terms of the moments for the MKFS-NDD Scheme and several new integrals. The following integrals are defined through a change in variables as:

$$I_{21}(\Psi)[\bar{u}_1, \bar{u}_2] = I_D^{11}(\Psi)[\bar{u}_1, -\bar{u}_2]\,, \tag{A.79}$$

$$I_{22}(\boldsymbol{\Psi})[\bar{u}_1, \bar{u}_2] = I_D^{12}(\boldsymbol{\Psi})[\bar{u}_1, -\bar{u}_2]\,, \tag{A.80}$$

$$I_{31}(\boldsymbol{\Psi})[\bar{u}_1, \bar{u}_2] = I_D^{7}(\boldsymbol{\Psi})[\bar{u}_1, -\bar{u}_2]\,, \tag{A.81}$$

$$I_{32}(\boldsymbol{\Psi})[\bar{u}_1, \bar{u}_2] = I_D^{8}(\boldsymbol{\Psi})[\bar{u}_1, -\bar{u}_2]\,, \tag{A.82}$$

$$I_{41}(\boldsymbol{\Psi})[\bar{u}_1, \bar{u}_2] = I_D^{3}(\boldsymbol{\Psi})[\bar{u}_1, -\bar{u}_2]\,, \tag{A.83}$$

$$I_{42}(\boldsymbol{\Psi})[\bar{u}_1, \bar{u}_2] = I_D^{4}(\boldsymbol{\Psi})[\bar{u}_1, -\bar{u}_2]\,, \tag{A.84}$$

$$I_{51}(\boldsymbol{\Psi})[\bar{u}_1, \bar{u}_2] = I_D^{5}(\boldsymbol{\Psi})[\bar{u}_1, -\bar{u}_2]\,, \tag{A.85}$$

$$I_{52}(\boldsymbol{\Psi})[\bar{u}_1, \bar{u}_2] = I_D^{6}(\boldsymbol{\Psi})[\bar{u}_1, -\bar{u}_2]\,, \tag{A.86}$$

$$\tag{A.87}$$

where $\boldsymbol{\Psi} = (\psi_1,\ \psi_2,\ \psi_3,\ \psi_4)^T$.

We define the following new integrals $I\!I_k$ for values of k equal to 32, 34, and 36 as:

$$I\!I_{32} = \int_{-\infty}^{0}\int_{-c_1\alpha}^{\infty}\left[\frac{e^{-\beta(c_2-u_2)^2}}{c_2}dc_2\right]c_1^2 e^{-\beta(c_1-u_1)^2}dc_1 \tag{A.88}$$

$$= \frac{\pi\bar{\rho}_1}{\rho\beta}[-\bar{\alpha}_2 e^{-\bar{w}_1^2} erfc(-\bar{w}_2) + \frac{2}{\sqrt{\pi}}\bar{u}_2\Omega_3 + (1+2\bar{u}_2^2)\Omega_4]\,,$$

$$I\!I_{34} = \int_{-\infty}^{0}\int_{-c_1\alpha}^{\infty}\left[\frac{e^{-\beta(c_2-u_2)^2}}{c_2}dc_2\right]c_1^3 e^{-\beta(c_1-u_1)^2}dc_1 \tag{A.89}$$

$$
\begin{aligned}
&= \frac{\pi\bar{\rho}_2}{\rho\beta}[\sqrt{\pi}\,\bar{\alpha}_2(\bar{\alpha}_1\bar{\alpha}_2\bar{v}_2 - \bar{u}_2)e^{-\bar{w}_1^2}erfc(-\bar{w}_2) \\
&\quad +\bar{\alpha}_2^2 e^{-(\bar{u}_1^2+\bar{u}_2^2)} + 2(1+\bar{u}_2^2)\Omega_3 + \sqrt{\pi}\bar{u}_2(2\bar{u}_2^2+3)\Omega_4]\,, \\
I\!I_{36} &= \int_{-\infty}^{0}\int_{-c_1\alpha}^{\infty}\left[\frac{e^{-\beta(c_2-u_2)^2}}{c_2}dc_2\right]c_1^4 e^{-\beta(c_1-u_1)^2}dc_1 \qquad \text{(A.90)} \\
&= \frac{\pi\bar{\rho}_3}{\rho\beta}[\bar{\alpha}_2^2 e^{-(\bar{u}_1^2+\bar{u}_2^2)}(\bar{u}_2 - \bar{\alpha}_1\bar{\alpha}_2\bar{v}_2) + \frac{\sqrt{\pi}}{2}(3\bar{\alpha}_2 - \bar{\alpha}_2^3 + 4\bar{\alpha}_1^3\bar{\alpha}_2^2\bar{v}_1\bar{v}_2 - \bar{\alpha}_1^4\bar{\alpha}_2\bar{v}_1^2 \\
&\quad -5\bar{\alpha}_2^3\bar{\alpha}_1^2\bar{v}_2^2)e^{-\bar{w}_1^2}erfc(-\bar{w}_2) + \bar{u}_2(2\bar{u}_2^2+5)\Omega_3 + \frac{\sqrt{\pi}}{2}(3+12\bar{u}_2^2+4\bar{u}_2^4)\Omega_4]\,.
\end{aligned}
$$

The remaining $I\!I$ integrals may be evaluated as

$$
\begin{aligned}
I\!I_{42}(\bar{u}_1,\bar{u}_2,\alpha) &= I\!I_{32}(-\bar{u}_1,\bar{u}_2,-\alpha)\,, \\
I\!I_{44}(\bar{u}_1,\bar{u}_2,\alpha) &= I\!I_{34}(-\bar{u}_1,\bar{u}_2,-\alpha)\,, \\
I\!I_{46}(\bar{u}_1,\bar{u}_2,\alpha) &= I\!I_{36}(-\bar{u}_1,\bar{u}_2,-\alpha)\,, \\
I\!I_{21}(\bar{u}_1,\bar{u}_2,\alpha) &= I\!I_{32}(\bar{u}_2,\bar{u}_1,1/\alpha)\,, \\
I\!I_{23}(\bar{u}_1,\bar{u}_2,\alpha) &= I\!I_{34}(\bar{u}_2,\bar{u}_1,1/\alpha)\,, \qquad \text{(A.91)} \\
I\!I_{25}(\bar{u}_1,\bar{u}_2,\alpha) &= I\!I_{36}(\bar{u}_2,\bar{u}_1,1/\alpha)\,, \\
I\!I_{51}(\bar{u}_1,\bar{u}_2,\alpha) &= I\!I_{32}(-\bar{u}_2,\bar{u}_1,-1/\alpha)\,, \\
I\!I_{53}(\bar{u}_1,\bar{u}_2,\alpha) &= I\!I_{34}(-\bar{u}_2,\bar{u}_1,-1/\alpha)\,, \\
I\!I_{55}(\bar{u}_1,\bar{u}_2,\alpha) &= I\!I_{36}(-\bar{u}_2,\bar{u}_1,-1/\alpha)\,,
\end{aligned}
$$

The remaining moments may be written as:

$$
\begin{aligned}
I_{27}(\psi_1) &= \frac{\rho\beta}{\pi}I\!I_{21}\,, \qquad \text{(A.92)} \\
I_{27}(\psi_2) &= \frac{\rho\beta}{\pi}I\!I_{23}\,, \qquad \text{(A.93)} \\
I_{27}(\psi_3) &= I_{21}(\psi_2)\,, \qquad \text{(A.94)} \\
I_{27}(\psi_4) &= (\frac{1}{4\beta}+e')I_{27}(\psi_1) + \frac{\rho\beta}{2\pi}(I_{12A}+I\!I_{25})\,, \qquad \text{(A.95)} \\
I_{57}(\psi_1) &= \frac{\rho\beta}{\pi}I\!I_{51}\,, \qquad \text{(A.96)} \\
I_{57}(\psi_2) &= \frac{\rho\beta}{\pi}I\!I_{53}\,, \qquad \text{(A.97)}
\end{aligned}
$$

$$I_{57}(\psi_3) = I_{51}(\psi_2)\,, \tag{A.98}$$

$$I_{57}(\psi_4) = (\frac{1}{4\beta} + e')I_{57}(\psi_1) + \frac{\rho\beta}{2\pi}(I_{6A} + I\!I_{55})\,, \tag{A.99}$$

$$I_{38}(\psi_1) = \frac{\rho\beta}{\pi} I\!I_{32}\,, \tag{A.100}$$

$$I_{38}(\psi_2) = I_{32}(\psi_3)\,, \tag{A.101}$$

$$I_{38}(\psi_3) = \frac{\rho\beta}{\pi} I\!I_{34}\,, \tag{A.102}$$

$$I_{38}(\psi_4) = (\frac{1}{4\beta} + e')I_{38}(\psi_1) + \frac{\rho\beta}{2\pi}(I_{7B} + I\!I_{36})\,, \tag{A.103}$$

$$I_{48}(\psi_1) = \frac{\rho\beta}{\pi} I\!I_{42}\,, \tag{A.104}$$

$$I_{48}(\psi_2) = I_{42}(\psi_3)\,, \tag{A.105}$$

$$I_{48}(\psi_3) = \frac{\rho\beta}{\pi} I\!I_{44}\,, \tag{A.106}$$

$$I_{48}(\psi_4) = (\frac{1}{4\beta} + e')I_{48}(\psi_1) + \frac{\rho\beta}{2\pi}(I_{3B} + I\!I_{46})\,. \tag{A.107}$$

The LDA-scheme utilizes a set of primed integrals, I'_k which correspond to up-diagonal triangulations. They may be evaluated in terms of non-primed down-diagonal triangulations I'_k. For values of k equal to 21, 31, 41, 51, 38 and 48 we have:

$$I'_k(\Psi_1)[\bar{u}_1, \bar{u}_2] = I_k(\Psi_1)[\bar{u}_1, -\bar{u}_2]\,, \tag{A.108}$$

$$I'_k(\Psi_2)[\bar{u}_1, \bar{u}_2] = I_k(\Psi_2)[\bar{u}_1, -\bar{u}_2]\,, \tag{A.109}$$

$$I'_k(\Psi_3)[\bar{u}_1, \bar{u}_2] = -I_k(\Psi_3)[\bar{u}_1, -\bar{u}_2]\,, \tag{A.110}$$

$$I'_k(\Psi_4)[\bar{u}_1, \bar{u}_2] = I_k(\Psi_4)[\bar{u}_1, -\bar{u}_2]\,, \tag{A.111}$$

and for values of k equal to 22, 32, 42, 52, 27 and 57 we have:

$$I'_k(\Psi_1)[\bar{u}_1, \bar{u}_2] = -I_k(\Psi_1)[\bar{u}_1, -\bar{u}_2]\,, \tag{A.112}$$

$$I'_k(\Psi_2)[\bar{u}_1, \bar{u}_2] = -I_k(\Psi_2)[\bar{u}_1, -\bar{u}_2]\,, \tag{A.113}$$

$$I'_k(\Psi_3)[\bar{u}_1, \bar{u}_2] = I_k(\Psi_3)[\bar{u}_1, -\bar{u}_2]\,, \tag{A.114}$$

$$I'_k(\Psi_4)[\bar{u}_1, \bar{u}_2] = -I_k(\Psi_4)[\bar{u}_1, -\bar{u}_2]\,, \tag{A.115}$$

A.5 Approximate Integration

Approximate integration techniques are needed to evaluate the integrals given by Eqs. (A.7 - A.9). In the present analysis, a Gauss-Laguerre quadrature has been utilized. Here, the integrals are rewritten using the change of variables $\xi^{\pm} = z \pm \bar{u}_1$ as

$$\Omega_{1,2} = \int_0^{\infty} e^{-\xi^{\pm}} F(\xi^{\pm}) d\xi^{\pm} , \tag{A.116}$$

where

$$F(\xi^{\pm}) = e^{\xi^{\pm}} e^{-(\xi^{\pm} \mp \bar{u}_1)^2} erf[(\pm\xi^{\pm} - \bar{u}_1)\alpha + \bar{v}_1] , \tag{A.117}$$

and

$$\Omega_{3,4} = \int_0^{\infty} e^{-\xi^{+}} F^{3,4}(\xi^{+}) d\xi^{+} , \tag{A.118}$$

where

$$F^3(\xi^+) = \frac{e^{\xi^+} e^{-(\xi^+ - \bar{u}_1)^2}}{\xi^+} [e^{-((\xi^+ - \bar{u}_1)\alpha + \bar{v}_1)^2} - e^{-\bar{u}_2^2}] , \tag{A.119}$$

$$F^4(\xi^+) = \frac{e^{\xi^+} e^{-(\xi^+ - \bar{u}_1)^2}}{\xi^+} [erfc((\xi^+ - \bar{u}_1)\alpha + \bar{v}_1) - erfc(\bar{u}_2)] . \tag{A.120}$$

The integral Ω_k may now be approximated as

$$\Omega_k \approx \sum_{i=0}^{n} \omega_i F^k(\xi_i) , \tag{A.121}$$

where ω_i are the Gauss-Laguerre coefficients and ξ_i are the quadrature points. Calculations were performed using a 28 point quadrature.

Appendix B

Flux-Difference Upwind Splitting

Roe's approximate Riemann solver presented here is an ingenious way of extending the linear wave decomposition to the system of non-linear equations, particularly to the two-dimensional Euler equations. It is based on characteristic decomposition of the flux differences while ensuring the conservation properties of the scheme. Being one of the Godunov-type methods, it represents physical fluxes at the cell interface by solving the one-dimensional Riemann problem across that interface. The general formulation according to proposed by Roe approach is written as

$$f^*_{i+1/2} = \frac{1}{2}\left[f\left(U^L_{i+1/2}\right) + f\left(U^R_{i+1/2}\right) - \left\|\tilde{A}\right\|_{i+1/2}\left(U^L_{i+1/2} - U^R_{i+1/2}\right)\right], \tag{B.1}$$

where the subscripts R and L are for the right and left states at the cell interface. *Roe matrix* $\tilde{A}$ is constructed using Roe averaged variables and the transformation from conservative to characteristic variables:

$$\left\|\tilde{A}\right\| = \tilde{P}\left\|\tilde{\Lambda}\right\|\tilde{P}^{-1}, \tag{B.2}$$

where $\tilde{P}$ is the matrix columns of which are right eigenvectors of $\tilde{A}$

$$P = \begin{Vmatrix} 1 & 0 & \frac{\rho}{2c} & \frac{\rho}{2c} \\ u & \rho\hat{k}_y & \frac{\rho}{2c}(u + c\hat{k}_x) & \frac{\rho}{2c}(u - c\hat{k}_x) \\ \tilde{v} & -\rho\hat{k}_x & \frac{\rho}{2c}(v + c\hat{k}_y) & \frac{\rho}{2c}(v - c\hat{k}_y) \\ \frac{|V|^2}{2} & \rho(u\hat{k}_y - v\hat{k}_x) & \frac{\rho}{2c}(H + c\vec{v}\cdot\vec{1}_k) & \frac{\rho}{2c}(H - c\vec{v}\cdot\vec{1}_k) \end{Vmatrix}, \tag{B.3}$$

calculated using Roe averaged variables and the diagonal matrix of eigenvalues, $\tilde{\Lambda}$, is

$$\tilde{\Lambda} = \left\| \begin{array}{cccc} \tilde{u} & 0 & 0 & 0 \\ 0 & \tilde{u} & 0 & 0 \\ 0 & 0 & \tilde{u}+\tilde{c} & 0 \\ 0 & 0 & 0 & \tilde{u}-\tilde{c} \end{array} \right\|. \tag{B.4}$$

We used normal unit vector $\vec{k} = (\hat{k}_x, \hat{k}_y)$ and its orthogonal counterpart $\vec{1}_k = (\hat{k}_y, -\hat{k}_x)$ to define the cell interface and H is the total enthalpy.

The matrix $\tilde{A}$ has to satisfy the conservation principles and the conservative decomposition of the flux difference will be represented as

$$\tilde{A}_{i+1/2}\left(U^L_{i+1/2} - U^R_{i+1/2}\right) = f\left(U^R_{i+1/2}\right) - f\left(U^L_{i+1/2}\right). \tag{B.5}$$

Particular choice of the averaged variables that make this linearization conservative is the average weighted by the square root of the densities. We define average function

$$\Psi_{L,R} = \frac{\sqrt{\rho_{L,R}}}{\sqrt{\rho}_L + \sqrt{\rho}_R} \tag{B.6}$$

and the averages will be defined as

$$\begin{aligned} \tilde{\rho} &= \sqrt{\rho_L \rho_R}, \\ \tilde{u} &= \Psi_L u_L + \Psi_R u_R, \\ \tilde{v} &= \Psi_L v_L + \Psi_R v_R, \\ \tilde{H} &= \Psi_L H_L + \Psi_R H_R, \\ \tilde{c}^2 &= (\gamma - 1)\left[\tilde{H} - \frac{1}{2}(\tilde{u}^2 + \tilde{v}^2)\right]. \end{aligned}$$

The flux-difference splitting of Roe may violate the entropy condition fi the eigenvalues λ_l of the Jacobian matrix $\tilde{A}_{i+1/2}$ vanish. To prevent expansion shocks, the eigenvalues should be modified as recommended by Harten [11]:

$$|\lambda| = \frac{\lambda^2 + \delta^2}{2\delta} \quad if |\lambda| < \delta \tag{B.7}$$

where δ is a small threshold.

Appendix C

Matrix Dissipation

The scalar dissipation model applies the same dissipation scaling by the spectral radius $|u|+c$ for all governing equations. This approach is not optimal for the resolution of the shocks and contacts because of excessive smearing. Turkel [2] suggested this scalar coefficients to be replaced by the absolute values of the Jacobian matrices. The matrix $A = \partial F/\partial Q$ can be diagonalized

$$\Lambda_\xi = T^{-1}AT = Diag[\lambda_1\lambda_2\lambda_3\lambda_3] \tag{C.1}$$

where

$$\lambda_{1,2} = \xi_x u + \xi_y v \pm \sqrt{\xi_x^2 + \xi_y^2}, \quad \lambda_3 = \xi_x u + \xi_y v. \tag{C.2}$$

The absolute value of the matrix is

$$\begin{aligned} |A| &= T\Lambda_\xi T^{-1} = \\ &= |\lambda_3|\boldsymbol{I} + \left(\frac{|\lambda_1| + |\lambda_2|}{2} - |\lambda_3|\right)\left[\frac{\gamma-1}{c^2}\boldsymbol{E}_1 + \frac{1}{\xi_1^2+\xi_2^2}\boldsymbol{E}_2\right] \\ &= \frac{|\lambda_1| - |\lambda_2|}{2}\left(\frac{1}{\sqrt{\xi_1^2+\xi_2^2}}\right)[\boldsymbol{E}_3 + (\gamma-1)\boldsymbol{E}_4]\,. \end{aligned}$$

There 4×4 matrices $\boldsymbol{E}_l$ can be expressed as the products of the four vectors

$$\begin{aligned} \boldsymbol{R}_1 &= \{1, u, v, H\}^T \\ \boldsymbol{R}_2 &= \{-(\xi_x u + \xi_y v), \xi_x, \xi_y, 0\} \end{aligned}$$

$$\begin{aligned}\boldsymbol{R}_3 &= \{0, \xi_x, \xi_y, \xi_x u + \xi_y v\}^T \\ \boldsymbol{R}_4 &= \{\frac{u^2+v^2}{2}, -u, -v, 1\}\end{aligned}$$

in the following combinations:

$$\begin{aligned}\boldsymbol{E}_1 &= \boldsymbol{R}_1\boldsymbol{R}_2, \quad \boldsymbol{E}_2 = \boldsymbol{R}_3\boldsymbol{R}_4, \\ \boldsymbol{E}_3 &= \boldsymbol{R}_1\boldsymbol{R}_4, \quad \boldsymbol{E}_4 = \boldsymbol{R}_3\boldsymbol{R}_2.\end{aligned}$$

The presented changes in the scaling procedure require additional transformation of the eigenvalues λ_l in order to prevent artificial viscosity from vanishing at the stagnation points and sonic lines [3]. The lower limit on these values are based on the spectral radius:

$$|\tilde{\lambda}_1| = max(|\lambda_1|, V_n\rho(A)), \quad \rho(A) = |\xi_x u + \xi_y v| + c\sqrt{a_1^2 + a_2^2}, \tag{C.3}$$

$$|\tilde{\lambda}_2| = max(|\lambda_2|, V_n\rho(A)), \quad |\tilde{\lambda}_3| = max(|\lambda_3|, V_l\rho(A)), \tag{C.4}$$

where the choice of V_l and V_n are based on the convergence acceleration and the sharpness of resolution. The practical values for the variables is between 0.2 and 0.3. Moreover, one can use a different limitations for the linear eigenvalue λ_3 and the nonlinear eigenvalues $\lambda_{1,2}$.

After we calculated the scaling matrix we can form new artificial dissipation terms:

$$D_\xi^2 Q_{i,j} = \nabla_\xi \left[\left(|A|_{i+1/2,j} \epsilon^{(2)}_{i+1/2,j} \right) \Delta_\xi \right] Q_{i,j} \tag{C.5}$$

$$D_\xi^4 Q_{i,j} = \nabla_\xi \left[\left(|A|_{i+1/2,j} \epsilon^{(4)}_{i+1/2,j} \right) \Delta_\xi \nabla_\xi \Delta_\xi \right] Q_{i,j} \tag{C.6}$$

that we use instead of Eq. (4.57) in the central difference solver.

Appendix D

Axisymmetric flow

In the three dimensional calculation of the axisymmetric flow it is practical to simplify the governing equations and to solve two dimensional problem. The compressible Euler equations will be transformed to the following form:

$$\frac{\partial}{\partial t}(r\boldsymbol{U}) + \frac{\partial}{\partial z}(r\boldsymbol{F}) + \frac{\partial}{\partial r}(r\boldsymbol{G}) = \boldsymbol{W}, \tag{D.1}$$

where

$$\boldsymbol{U} = \begin{pmatrix} \rho \\ \rho u_z \\ \rho u_r \\ \rho e \end{pmatrix}, \boldsymbol{F} = \begin{pmatrix} \rho u_z \\ \rho u_z^2 + p \\ \rho u_r u_z \\ (\rho e + p) u_z \end{pmatrix}, \boldsymbol{G} = \begin{pmatrix} \rho u_r \\ \rho u_z u_r \\ \rho u_r^2 + p \\ \rho(\rho e + p) u_r \end{pmatrix}, \boldsymbol{W} = \begin{pmatrix} 0 \\ 0 \\ rp \\ 0 \end{pmatrix}. \tag{D.2}$$

Appendix E

Transformation to Generalized Coordinates

Practical calculations with complex geometries require more flexible tools than the governing differential equations developed for a Cartesian Coordinate system. The general practice is to transform the probem from the physical domain (x_1, x_2, x_3) to a uniformly spaced computational grid (ξ, η, ζ). The new coordinate system is given as

$$\begin{aligned} \xi &= \xi(x_1, x_2, x_3) \\ \eta &= \eta(x_1, x_2, x_3) \\ \zeta &= \zeta(x_1, x_2, x_3) \end{aligned} \tag{E.1}$$

and the Jacobian of the transformation

$$J = \frac{\partial(\xi, \eta, \zeta)}{\partial(x_1, x_2, x_3)} = \det \begin{pmatrix} \xi_{x_1} & \xi_{x_2} & \xi_{x_3} \\ \eta_{x_1} & \eta_{x_2} & \eta_{x_3} \\ \zeta_{x_1} & \zeta_{x_2} & \zeta_{x_3} \end{pmatrix}. \tag{E.2}$$

The new form of the governing equations may be rewritten as

$$\frac{1}{J}\frac{\partial \boldsymbol{Q}}{\partial t} + \frac{\partial \tilde{\boldsymbol{F}}}{\partial \xi} + \frac{\partial \tilde{\boldsymbol{G}}}{\partial \eta} + \frac{\partial \tilde{\boldsymbol{H}}}{\partial \zeta} = 0 \tag{E.3}$$

where

$$\tilde{\boldsymbol{F}} = \frac{\bar{\nabla}\boldsymbol{\xi}}{J} \cdot \boldsymbol{S}, \tag{E.4}$$
$$\tilde{\boldsymbol{G}} = \frac{\bar{\nabla}\boldsymbol{\eta}}{J} \cdot \boldsymbol{S},$$
$$\tilde{\boldsymbol{H}} = \frac{\bar{\nabla}\boldsymbol{\zeta}}{J} \cdot \boldsymbol{S}.$$

The vectors $\bar{\nabla}\boldsymbol{\xi}, \bar{\nabla}\boldsymbol{\eta}, \bar{\nabla}\boldsymbol{\zeta}$, are the unit vectors normal to the transformed coordinate surfaces and are defined by

$$\bar{\nabla}\boldsymbol{\xi} = \frac{\nabla\xi}{|\nabla\xi|} = \xi_{x_1}\boldsymbol{i}_1 + \xi_{x_1}\boldsymbol{i}_2 + \xi_{x_1}\boldsymbol{i}_3, \tag{E.5}$$

and the same for every component. In addition, we use flux-vector $\boldsymbol{S}$ that is defined in Eq. (2.32). The contravariant velocity in new directions are given as

$$\begin{aligned} \tilde{u}_1 &= \boldsymbol{u} \cdot \nabla\boldsymbol{\xi}, \\ \tilde{u}_2 &= \boldsymbol{u} \cdot \nabla\boldsymbol{\eta}, \\ \tilde{u}_3 &= \boldsymbol{u} \cdot \nabla\boldsymbol{\zeta}. \end{aligned} \tag{E.6}$$

Bibliography

[1] Jameson, A., Schmidt, W., and Turkel, E., "Numerical Solutions of the Euler Equations by Finite Volume Methods with Runge-Kutta Time Stepping Schemes," AIAA Paper, no. 81-1259, 1981.

[2] Turkel, E., "Improving the Accuracy of Central Difference Schemes," in *Lecture Notes in Physics*, vol. 323, pp. 586–591, New York: Springer-Verlag, 1988.

[3] Turkel, E. and Vatsa, V., "Effect of Artificial Viscosity on Three-Dimensional Flow Solutions," AIAA Journal, vol. 32, no. 1, pp. 39–45, 1994.

[4] Swanson, R. and Turkel, E., "On Central Difference and Upwind Schemes," CR 182061, NASA, Jun 1990.

[5] Gerlinger, P., Algermissen, J., and Bruggemann, D., "Matrix Dissipation for Central Difference Schemes with Combustion," AIAA Journal, vol. 33, no. 10, pp. 1865–70, 1995.

[6] Courant, R., Isaacson, E., and Reeves, M., "On the Solution of Nonlinear Hyperbolic Differential Equations by Finite Differences," Pure and Applied Mathematics, vol. 5, pp. 243–255, 1952.

[7] Van Leer, B., "Flux-Vector Splitting for the Euler Equations," in *Lecture Notes in Physics*, vol. 170, New York: Springer-Verlag, 1982.

[8] Steger, J. L. and Warming, R. F., "Flux Vector Splitting of the Inviscid Gasdynamics Equations with Application to Finite Difference Methods," Journal of Computational Physics, vol. 40, 1981.

[9] Godunov, S., "A Finite Difference Method for the Numerical Computation of Discontinuous Solutions of the Equations of Fluid Dynamics," Mat. Sbornik, vol. 47, 1959.

[10] Roe, P., "Approximate Riemann Solvers, Parameter Vectors, and Difference Schemes," Journal of Computational Physics, vol. 43, pp. 357–372, 1981.

[11] Harten, A., "High Resolution Schemes for Hyperbolic Conservation Laws," Journal of Computational Physics, vol. 49, pp. 357–393, 1983.

[12] Roe, P., "The Use of the Riemann Problem in Finite Difference Schemes," Lecture Notes in Physics, vol. 141, pp. 354–359, 1981.

[13] Chakravarthy, S. and Osher, S., "High Resolution Applications of the Osher Upwind Scheme for the Euler Equation," AIAA paper, no. 83-1943, 1983.

[14] Van Leer, B., "Towards the Ultimate Conservative Difference Scheme. V: A Second Order Sequel to Godunov's Method," Journal of Computational Physics, vol. 32, pp. 101–136, 1979.

[15] Van Leer, B., "Upwind-Difference Methods for Aerodynamic Problems Governed by the Euler Equations," Lectures in Applied Mathematics, vol. 22, pp. 327–336, 1985.

[16] Colella, P. and Woodward, P., "The Piecewise Parabolic Method(PPM) for Gasdynamic Simulation.," Journal of Computational Physics, vol. 54, pp. 174–201, 1984.

[17] Harten, A., Engquist, B., Osher, S., and Chakravarthy, S., "Uniformly High-order Accurate Essentially Non-oscillatory Schemes III," Journal of Computational Physics, vol. 71, pp. 231–303, 1987.

[18] Jameson, A., "Numerical Wind Tunnel - Vision or Reality," AIAA paper, no. 93-3021, 1993.

[19] Goodman, J. and R., L., "On the Accuracy of Stable Schemes for 2D Scalar Conservation Laws," Math. Comp., vol. 45, pp. 15–21, 1989.

[20] Spekreijse, S., "Multigrid Solution of Monotone Second-Order Discretisations of Hyperbolic Conservation Laws," Mathematics Computation, vol. 49, pp. 135–155, 1987.

[21] Struijs, R., Deconinck, H., and Roe, P., "Fluctuation Splitting Schemes for the 2D Euler Equations," Von Karman Institute Lecture Series, vol. 01, Jan. 1991.

[22] Jameson, A., "Artificial Diffusion, Upwind Biasing, Limiters and Their Effect on Accuracy and Multigrid Convergence in Transonic and Hypersonic Flows," AIAA paper, no. 93-3359, 1993.

[23] Ni, R., "A Multiple Grid Scheme for Solving the Euler equations," AIAA Journal, vol. 20, pp. 1565–1571, 1982.

[24] Morton, K.W.and Paisley, M., "On the Cell-center and Cell-vertex Approaches to the Steady Euler Equations and the Use of Shock Fitting," in *Proceedings of Tenth International Conference on Numerical Methods in Fluid Dynamics* (Zhuang, F. and Zhu, Y., eds.), (Beijing), Springer-Verlag, 1986.

[25] Morton, K., Childs, P., and Rudgyard, M., "The Cell Vertex Method for Steady Compressible Flow," in *Proceedings of the IMA Conference, Numerical Methods for Fluid Dynamics III* (Morton, K. and Baines, M., eds.), (Oxford), Oxford University Press, 1988.

[26] Morton, K. and Stringer, S., "Artificial Viscosity and the Cell Vertex Method," in *Proceedings of the 15th ICNMFD Conference*, (Monterey), 1996.

[27] Roe, P., "Fluctuations and Signals - a Framework fo Numerical Evolution Problems," in *Proceedings of the IMA Conference, Numerical Methods for Fluid Dynamics* (Morton, K. and Baines, M., eds.), Academic Press, 1982.

[28] Roe, P., "Discrete Models for the Numerical Analysis of Time-Dependent Multidimensional Gas Dynamics," Journal of Computational Physics, vol. 63, pp. 458–476, 1986.

[29] Roe, P., "Linear advection schemes on triangular meshes," Technical report CoA 8720, Cranfield Institute of Technology, Nov 1987.

[30] Deconinck, H., Struijs, R., and Roe, P., "Fluctuation Splitting for Multidimensional Convection Problems: an Alternative to Finite Volume and Finite Element Methods," Von Karman Institute Lecture Series, vol. 03, Mar. 1990.

[31] Deconinck, H., Powell, K., Roe, P., and Struijs, R., "Multi-Dimensional Schemes for Scalar Advection," AIAA paper, no. 91-1532, pp. 60–69, 1991.

[32] Struijs, R., Deconinck, H., De Palma, P., and Powell, K., "Progress on Multidimensional Upwind Euler Solvers for Unstructured Grids," AIAA Paper, June 1991.

[33] Paillere, H., Deconinck, H., Struijs, R., Roe, P., Mesaros, L., and Muller, J., "Computation of Inviscid Compressible Flows Using Fluctuation-Splitting on Triangular Meshes," AIAA paper, no. 93-3301, pp. 36–50, 1993.

[34] Paillere, H., Carette, J., and Deconinck, H., "Multidimensional Upwind and SUPG Methods for the Solution of the Compressible Flow Equations on Unstructured Grids," Von Karman Institute Lecture Series on Computational Fluid Dynamics, no. 1994-05, 1994.

[35] Paillere, H., *Multidimensional Upwind Residual Distribution Schemes for the Euler and Navier-Stokes Equations on Unstructured Grids.* PhD thesis, Von Karman Institute for Fluid Dynamics, Rhode St-Genèse, Belgium, June 1995.

[36] Mesaros, L., *Multi-dimensional Fluctuation Splitting Schemes for the Euler Equations on Unstructured Grids.* PhD thesis, University of Michigan, Ann-Arbor, Michigan, 1995.

[37] Sidilkover, D., "A Genuinely Multi-dimensional Upwind Scheme and Efficient Multigrid Solver for the Compressible Euler Equations," Tech. Rep. 94-84, ICASE, NASA Langley, 1994.

[38] Deconinck, H., L., R., and Struijs, R., "A Multi-Dimensional Generalization of Roe's Flux Difference Splitter for the Euler Equations," Journal of Computers and Fluids, vol. 22, no. 2, pp. 215–222, 1993.

[39] Sidilkover, D. and Brandt, A., "Multigrid Solution to Steady-state 2D Conservation Laws," SIAM J. Numer. Anal., vol. 30, pp. 249–274, 1993.

[40] Deconinck, H., Hirsch, C., and Peuteman, J., "Characteristic Decomposition Methods for the Multidimensional Euler Equations," Lecture Notes in Physics, vol. 264, pp. 216–221, 1986.

[41] Hirsch, C., Lacor, C., and Deconinck, H., "Convection Algorithms Based on a Diagonalization Procedure for the Multidimensional Euler Equations," AIAA Paper, no. 87-1163, pp. 667–676, 1987.

[42] Rumsey, C., Van Leer, B., and Roe, P., "A Grid-Independent Approximate Riemann Solver With Applications to the Euler and Navier-Stokes Equations," AIAA Paper, no. 91-0239, 1991.

[43] Rumsey, C., Van Leer, B., and Roe, P., "Effect of a Multi-Dimensional Flux Function on the Monotonicity of Euler and Navier-Stokes Computations," AIAA Paper, no. 91-1530-CP, pp. 32–39, 1991.

[44] Davis, S., "A Rotationally Biased Upwind Difference Scheme for the Euler Equations.," Journal of Computational Physics, vol. 56, pp. 65–92, 1984.

[45] Levy, D., Powell, K., and Van Leer, B., "Implementation of a Grid-independent Upwind Scheme for the Euler Equations," in *AIAA 9th Computational Fluid Dynamics Conference*, 1989.

[46] Dadone, A. and Grossman, B., "A Rotated Upwind Scheme for the Euler Equations," AIAA paper, Jan. 1991.

[47] Sidilkover, D., *Numerical Solution to Steady-state Problems with Discontinuities.* PhD thesis, Weizmann Institute of Science, Israel, 1989.

[48] Harten, A., Lax, P., and Van Leer, B., "On Upstream Differencing and Godunov-type Schemes for Hyperbolic Conservation Laws," SIAM Review, vol. 25, pp. 35–61, Jan. 1983.

[49] Deshpande, S. M., "Kinetic Theory Based New Upwind Methods For Inviscid Compressible Flows," AIAA Paper, no. 86-0275, 1986.

[50] Deshpande, S., "A Second Order Accurate, Kinetic-theory Based, Method for Inviscid Compressible Flows," NASA TP 2613, 1986.

[51] Perthame, B., "Boltzmann Type Schemes For Gas Dynamics and the Entropy Property," SIAM J. Numer Anal., vol. 27, pp. 1405–1421, 1990.

[52] Perthame, B. and Qiu, Y., "A Variant of Van Leer's Method for Multidimensional Systems of Conservation Laws," Journal of Computational Physics, vol. 112, pp. 370–381, 1994.

[53] Steinhoff, J., Senge, H., and Yanghu, W., "An Eulerian/Lagrangian Method for Computing Blade/Vortex Interactions." Private contacts.

[54] Steinhoff, J., Wang, C., Underhill, D., Mersch, T., and Wenren, Y., "Computational Vorticity Confinement: A Non-diffusive Eulerian Method for Vortex-Dominated Flows," preprint, UTSI, Tullahoma, TN, 1992.

[55] Steinhoff, J. and Mersch, T., "Computation of Incompressible Flow over Delta Wings Using Vorticity Confinement," AIAA Paper, no. 94–0646, 1994.

[56] Steinhoff, J., "Vorticity Confinement: A New Technique for Computing Vortex Dominated Flows," in *Frontiers of Computational Fluid Dynamics* (Caughey, D. and Hafez, M., eds.), pp. 253–264, New York: John Wiley and Sons, 1994.

[57] Steinhoff, J., Raviprakash, G., and Burley, C., "Navier-Stokes Computation of Blade-Vortex Interactions Using Vorticity Confinement," in *Proc. 33rd Aerospace Sciences Meeting*, Jan. 1995.

[58] Steinhoff, J. and Underhill, D., "Modification of the Euler Equations for "Vorticity Confinement": Application to the Computation of Interacting Vortex Rings," The Physics of fluids, vol. 6, no. 8, p. 2738, 1994.

[59] Puskas, E., Steinhoff, J., Underhill, D., and Wenren, Y., "Computation of Short Acoustic Pulses," in *Proceedings, 6th International Symposium on Computational Fluid Dynamics*, (Lake Tahoe, NV), 1995.

[60] Eppard, W. and Grossman, B., "A Multi-Dimensional Kinetic Based Upwind Solver for the Euler Equations," AIAA Paper, July 1993.

[61] Eppard, W., Pevchin, S., and Grossman, B., "Multi-dimensional Kinetic-based Upwind Algorithms for the Euler Equations," ICAM Report 93-12-02, Virginia Polytechnic Institute and State University, Blacksburg, Virginia 24061-0531, Dec 1993.

[62] Kogan, M., *Rarefied Gas Dynamics.* Plenum Press, New York, 1969.

[63] Bird, G., *Molecular Gas Dynamics and the Direct Simulation of Gas Flows.* Oxford University Press, 1994. ISBN 0-19-856195-4.

[64] Grad, H. in *Encyclopedia of Physics* (Flugge, S., ed.), vol. XII, p. 205, Berlin: Springer-Verlag, 1958.

[65] Harris, S., *An Introduction to the Theory of the Boltzmann Equation.* Holt, Rinehart, and Winston, New York, 1971.

[66] Liu, Y. and Vinokur, M., "Nonequilibrium Flow Computations:I. An Analysis of Numerical Formulation of Conservation Laws," CR 177489, NASA, 1988.

[67] Steger, J. and Warming, R., "Flux Vector Splitting of the Inviscid Gas-Dynamics Equations with Applications to Finite Difference Methods," Journal of Computational Physics, vol. 40, pp. 263–293, 1981.

[68] Roe, P., "Beyond the Riemann Problem I.," in *Algorithms trends for the 90s*, ICASE-LARC Workshop, Springer, 1993.

[69] Roe, P. and Sidilkover, D., "Optimum Positive Linear Schemes for Advection in Two and Three Dimensions," SIAM J. Numerical Analysis, vol. 29, pp. 1542–1568, 1992.

[70] Hirsch, C., "Compact Schemes for Two-Dimensional Convection Problems," Von Karman Institute Lecture Series, vol. 01, Jan. 1991.

[71] Struijs, R., *A Multi-dimensional Upwind Discretization Method for the Euler Equations on Unstructured Grids.* PhD thesis, The University of Delft, The Netherlands, 1994.

[72] Deconinck, H., Struijs, R., Bourgois, G., and Roe, P., "Compact Advection Schemes on Unstructured Grids," Preprint 1993-11, Von Karman Institute for Fluid Dynamics, Rhode St, Genese, Belgium, Mar 1993.

[73] Eppard, W., *Kinetic Algorithms for Non-equilibrium Gas Dynamics.* PhD thesis, Virginia Tech., Blacksburg, Virginia, Apr. 1996.

[74] Kim, J. and P., M., "Application of a Fractional-Step Method to Incompressible Navier-Stokes Equations," Journal of Computational Physics, vol. 59, 1985.

[75] Hirsch, C., *Numerical Computation of Internal and External Flows, Vol. 2.* John Wiley & Sons, 1991. ISBN 0-471-92452-0.

[76] Powell, K., Roe, P., and Quirk, J., "Adaptive Mesh Algorithms for Computational Fluid Dynamics," pp. 303–337, 1992.

[77] Prudhomme, S. and Haj-Hariri, H., "Investigation of Supersonic Underexpanded Jets Using Adaptive Unstructured Elements," Finite Elements in Analysis and Design, vol. 17, pp. 21–40, 1994.

[78] Chang, I. and Chow, W., "Mach Number from Underexpanded Axisymmetric Nozzle Flow," AIAA Journal, vol. 12, pp. 1079–1082, Aug. 1974.

Vita

The author was born on August 20th, 1970 in Tashkent, USSR. He began his engineering studies at Moscow Institute of Physics and Technology and graduated Summa Cum Laude in July 1993. Upon completion of his Master of Science degree, he entered the graduate program at Virginia Polytechnic Institute and State University. The next three years were spent in pursuit of a Doctorate in Aerospace Engineering.